Title
On Mechanical Transitions in Biologically Motivated Soft Matter Systems

Author
Fogle, Craig Alton

Publication Date
2015

University of California
Los Angeles

On Mechanical Transitions in Biologically Motivated Soft Matter Systems

A dissertation submitted in partial satisfaction
of the requirements for the degree
Doctor of Philosophy in Physics

by

Craig Fogle

2015

Abstract of the Dissertation

On Mechanical Transitions in Biologically Motivated Soft Matter Systems

by

Craig Fogle

Doctor of Philosophy in Physics

University of California, Los Angeles, 2015

Professor Joseph A. Rudnick, Chair

The notion of phase transitions as a characterization of a change in physical properties pervades modern physics. Such abrupt and fundamental changes in the behavior of physical systems are evident in condensed matter system and also occur in nuclear and subatomic settings. While this concept is less prevalent in the field of biology, recent advances have pointed to its relevance in a number of settings. Recent studies have modeled both the cell cycle [1] and cancer [2] as phase transition in physical systems. In this dissertation we construct simplified models for two biological systems. As described by those models, both systems exhibit phase transitions.

The first model is inspired by the shape transition in the nuclei of neutrophils during differentiation. During differentiation the nucleus transitions from spherical to a shape often described as "beads on a string." As a simplified model of this system, we investigate the spherical-to-wrinkled transition in an elastic core bounded to a fluid shell system. We find that this model exhibits a first-order phase transition, and the shape that minimizes the energy of the system scales as $(\mu r^3/\kappa)$.

The second system studied is motivated by the dynamics of globular proteins. These proteins may undergoes conformational changes with large displacements relative to their size. Transitions between conformational states are not possible if the dynamics are governed strictly by linear elasticity. We construct a model consisting of an predominantly elastic region near the energetic minimum of the system and a non-linear softening of the system at a critical displacement. We find that this simple model displays very rich dynamics include a sharp dynamical phase transition and driving-force-dependent symmetry breaking.

The dissertation of Craig Fogle is approved.

Amy Catherine Rowat
Alexander Jacob Levine
Joseph A. Rudnick, Committee Chair

University of California, Los Angeles
2015

To my family . . .

Table of Contents

Appendices

Appendices

List of Figures

ACKNOWLEDGMENTS

I wish to thank all of the members of the Department of Physics and Astronomy at UCLA. In particular members of the biophysics/Soft Matter groups. They have broaden my knowledge of the field of soft matter physics and I enjoy the discussions we had.

I would also like to acknowledges the many enjoyable conversations and helpful insights into the nuclear morphology project with Art Evans and William Klug.

I am grateful to Giovani Zocchi and Jonathan Rubin for interesting and helpful discussions in regards to the mechanical response and rheology of enzymes.

I all of the members Rowat lab for listening to talk through my projects. Amy Rowat provided me with a great deal of guidance several projects including the nuclear morphology project.

I thank Alex Levine for guidance on the nuclear morphology project. Additional, Alex as taught me a great deal about being a physicist. His insights have been invaluable.

I am immensely indebted to my supervisor Joesph Rudnick for his thorough counsel and advise, and for keeping my spirits high through all phases of my Ph.D.

Finally, I wish to think my friends and family. I am so glad that I had roommates who were patients enough to spend hours as a sounding board for my ideas as I thought through my projects.

I acknowledges support from the National Science Foundation through DMR Grants 1006128 and 1309423.

Chapters 2 [3] and 3 [4] are based on published journal articles and with the exception of reformatting and minor additions are presented as they appear in the corresponding publication.

VITA

2007	BS Engineering Physics, University of Colorado at Boulder
2007	BS Applied Mathematics, University of Colorado at Boulder

PUBLICATIONS

C. A. Fogle, J. L. Nagle and M. M. Desai, "Clonal Interference, Multiple Mutations and Adaptation in Large Asexual Populations," *Genetics*, vol. 180, no. 4, pp. 2163-73, Dec. 2008

C. A. Fogle, A. C. Rowat, A. J. Levine, and J. A. Rudnick, "Shape transitions in soft spheres regulated by elasticity," *Physical Review E - Statistical, Nonlinear, and Soft Matter Physics*, vol. 88, no. 5, Jul. 2013

C. A. Fogle, J. A. Rudnick and D. Jasnow, "Protein viscoelastic dynamics: a model system," version 1, pp. 1-19, Feb 2015. arXiv: `cond-mat.soft/1502.00343v1`

CHAPTER 1

Introduction

1.1 Interplay between physics and biology

Elasticity theory describes the way in which materials deform under an external stresses and the resulting arrangement of the resulting internal stresses. Because behavior in the vicinity of energy minima in atomic bonds is often well approximated by a simple harmonic oscillator for small displacements from equilibrium, many materials exhibit elastic behavior when exposed to weak external stresses. Because of this, elasticity theory enjoys broad applicability and can be utilized to address a broad range of topics. The equilibrium response of membranes and interfaces to external stresses has been characterized in terms of parameters such as bending rigidity, and mean and Gaussian curvature [5, 6]. An approach based on elasticity theory yields insights into the effects of thermal fluctuation on these physical properties in planar [7, 8] and more complex geometries [9–13]. Additionally, investigations have been performed on the mechanical response and topology of a network of randomly cross-linked polymers [14]. These structures appear in areas ranging from the design of new high-charge batteries and capacitors [15] to breads [16, 17] and other culinary creations [18, 19]. The role of structural entropy [20, 21], topology [22, 23], and thermal fluctuations [24] on the bulk elastic properties, as well as the connection between these macroscopic properties and the microscopic geometry [25, 26] have also been studied. In engineering and material science elasticity theory is utilized to study the mechanical properties of materials from the common, i.e. steel [27–29] and concrete [30–32], carbon fiber [32–34] and carbon nano-tubes [35–37]. Clearly, the elastic response of materials is important across many field of study.

The tools of elasticity theory have also seen extensive use in the study cellular and tissue biology. For example, the mechanical properties of cells and their ability to detect and respond to their physical environment have several biological consequences [38, 39]. Cells probe their environment and, through restructuring of their cytoskeletons, adjust their stiffness to more closely resemble it [40, 41]. In ovarian cancer a strong correlation has been documented between the cell's elastic moduli and its invasive/migrative potential [42]. This is significant because it implies that cell stiffness can be used has a biomarker for the health of the cell. Similar relationships have been found in cancer lines in both immortal cell lines [43, 44] and patient cells [45, 46]. An altered mechano-phenotype is also found to be an indicator of cell health in other disorders, such as sickle cell disease [47–50] and Hutchinson–Gilford progeria syndrome [51, 52]. The elastic properties of the environment surrounding pluripotent cells can effect their differentiated state. By adjusting the stiffness of the substrate, human mesenchymal stem cells can be directed along neuronal (soft substrate), muscle, or bone (hard substrate) lineages [53, 54].

Comprehensive studies have also been carried out on the elastic properties of biological macromolecules and polymers. The mechanical response of chromatin plays an important role in the accessibility of genomic information and in the dynamics of replication [55]. In addition, researchers have carried out studies of the elastic properties of both single chromatin fiber [56, 57] and of chromatin as a bulk [58, 59]. The elastic properties of actin networks [60, 61] play a critical role in numerous physiological processes, from mechanotransduction [62–64] and growth [65] to cell migration and motility [66–69].

1.2 The role of mechanical and morphological transitions in biology systems

The notion of a "phase transition" is ubiquitous in physics, chemistry and other scientific disciplines. In biological systems, a phase transitions can be characterized as a transformation of the system in which the phenotype or other physical properties can be mapped into distinct states. Such transitions are important, in that they allow the system to rapidly adapt to new conditions. In biological systems, phase transitions have been used to study processes ranging from the cell cycle [1] to cancer [2]. Here we will examine two examples of transitions of in biological systems in closer detail.

1.2.1 Morphological transitions: Membrane/core systems

Morphological transitions in the shape of cells and their nuclei are physiologically significant. One important example, examined here, is a shape transition in the nucleus of neutrophil. Neutrophils are the most common type of white blood cell and are among the major players in acute inflammation and initial immune response [70]. As stem cells in the bone morrow differentiate into neutrophils, their nuclei undergo a transition from roughly spherical to a lobulated shape. Figure 1.1 shows a pictorial mock-up of a neutrophil. Here we see that the nucleus is segmented in lobes connected by much thinner portions. The lobulated nucleus is much more deformable than it is when spherical. This is thought to be important in facilitating the rapid egress of neutrophils from the blood stream to sites of bacterial or fungal infection [71].

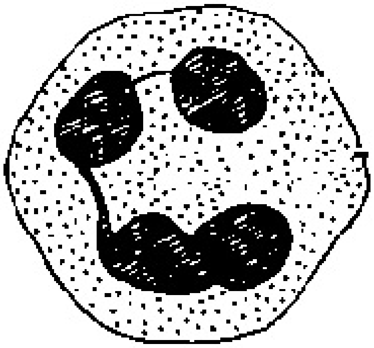

Figure 1.1: Pictorial image of a neutrophil

In this schematic image of a neutrophil, the nucleus take on a lobulated shape. This shape is often characterized as “beads on a string.”

This shape transition is induced by an increase in the expression of lamin-B receptor (LBR) when the cell differentiates into a neutrophil [71, 72]. As illustrated in Fig. 1.2,

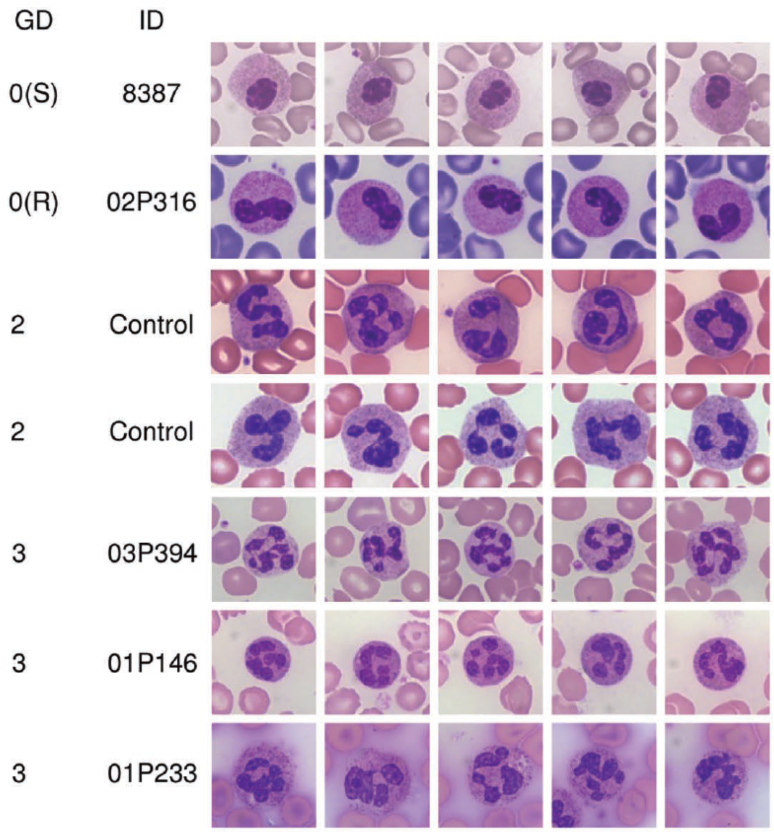

Figure 1.2: Effects of LBR on nuclear shape in neutrophils

A representative panel from the work of Gravemann *et al.* [72] showing the effects of the number of functional genetic copies on nuclear segmentation in neutrophils. The column **GD** is the number (0 to 3) of functional LBR copies present and the column **ID** is a code used to identify the individual from which the sample was taken. The number of functional LBR copies correlates with the segmentation of the neutrophil's nuclei (stained dark red) in blood smears. Nuclei in the top row (no functional copies of LBR) are a single blob which is roughly spherical. The is lower rows (**GD** ≥ 2) have nuclei which are greatly segmented.

there is a strong correlation between the number of copies of the LBR gene and the amount of lobulation in the nucleus. When no functional copies are present the nucleus remains roughly spherical. However, when 2 (normal) or 3 (extra) copies are present, the nucleus is segmented into more lobes. When normal cells are modified so as not to express LBR, no shape transition takes place during differentiation [71]. Other studies have shown that the area of the nucleus envelope scales approximately linearly with the expressions levels of LBR [73]. This implies that the upregulation of LBR corresponds to an increase in the surface of the nuclear membrane. In other words, the shape transition is induce by mass transport to the nuclear membrane.

Differentiation into neutrophils is also accompanied by a decrease in the expression of a fibrous protein called lamin-A. Lamin-A plays a role in many function in the cell. Significantly, it provides structural support to the nucleus [74–76]. Low levels of lamin-A correspond to softer nuclear membranes and high levels correspond to stiffer membranes [75, 77, 78]. Therefore, the downregulation of lamin-A during the differentiation of neutrophils results in a soft membrane. Rowat and collaborators [79] have shown that if the cells are modified to upregulated lamin-A during differentiation, the shape transition still takes place, but the resulting nucleus is closer to a bumpy sphere then to the normal lobulated morphology. This seems to imply that lamin-A plays the role of increasing nuclear membrane stiffness or bending rigidity.

The picture we are building of this transition can be seen in Fig. 1.3. This is shape transition driven by mass transport to the nuclear membrane in which membrane bending rigidity plays a large role in the resulting morphology. Constructing a model for this transition is understandably desirable, but also very difficult. The nuclear membrane is complex and contains an assortment of structures necessary for it to properly function. In addition, chromatin condensation causes changes in the architecture of the interior of the nucleus [80], resulting in additional stresses on the interior of the membrane. Moreover, the structure and interactions of the nuclear membrane proteins are not well understood. For these reasons, constructing an analytical model of the elastic response of the nucleus may be challenging at this point. As a first step in creating an analytic model of this and other related systems, we will look to analyze a model system in which mass transport drives a shape transition in which the resulting shape is governed by the elastic properties of the system.

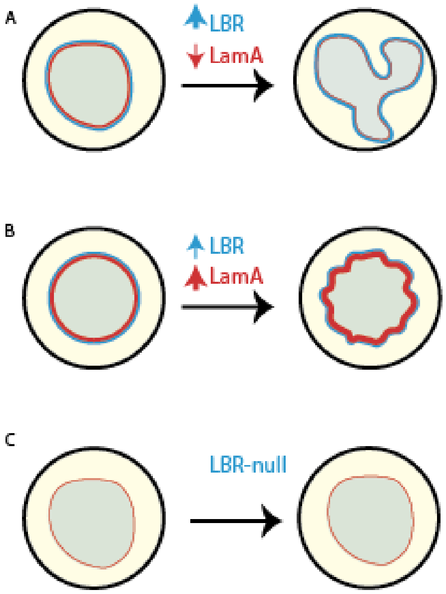

Figure 1.3: Nuclear shape transition during differentiation

Schematic of shape transition during differentiation. (A) Normal differentiation: Upregulation in LBR and a downregulation in lamin-A results in a lobulated nuclear morphology. (B) Upregulated lamin-A: A upregulation in both LBR and lamin-A results in transition into "bumpy sphere" morphology. (C) No LBR expressed: No shape transition takes place.

1.2.2 Phase transitions in dynamic systems

Another type of transition exhibited in biological systems is dynamical in nature. Dynamic transitions are characterized by a change in the system's mechanical response to an time-varying external drive. This is in contrast to the transition discussed in the Sec. 1.2.1, in which the change is in the physical properties of a static system. A particular type of dynamic transition involves systems in which the mechanical response changes from primarily elastic in nature to predominantly viscous. The standard characteristic of such a transition is smooth crossover from elastic to viscous response as the frequency of the driving force changes. Here we will examine another version of the viscoelastic transition, as seen experimentally in a dynamic transition in globular protein.

The mechanical response of a fibrous protein can is fairly well modeled by treating it as an elastic rod. However, there is not a similarly useful description of globular proteins. Changes in the conformational state of globular proteins are vital for function. The regulation of proteins through the binding of effector molecules at secondary active sites — allosteric regulation — requires that the protein has at least two of conformational states at approximately the same energy level [81]. The dynamics of protein folding also play an important role in protein-ligand binding [82] and enzymatic catalysis [83].

This conformational changes of an enzyme can often be large, with a displacement of $\sim 1\,nm$ for globular proteins with an overall size of $\sim 5\,nm$. These huge strains in the protein raise questions about the mechanics of the conformational dynamics and how the physical properties of the protein evolve during this process. A transition between states with nearly the same energy requires an enormous activation energy in the linear elastic regime. Thus, for these conformations to take place in biological system the dynamics must be non-linear in nature. One proposed mechanism for these transition is known as "protein quakes" or "cracking, " in which a crack or fissure forms and allows the protein to pivots into an new conformation [84–86].

Linear viscoelasticity is often used as a starting point to describe the mechanical response of proteins. The rheological properties of linear viscoelastic materials can be described in terms of a dynamic elastic modulus $G(\omega)$ [87]. In linear viscoelasticity the material there is a linear relationship between the current stress ($\sigma(t)$), the history of the strain ($\epsilon(t)$):

$$\sigma(t) = \int_{-\infty}^{t} K(t-t')\dot{\epsilon}(t')dt', \tag{1.2.1}$$

where the integration kernel ($K(t-t')$) is a called the relaxation function. Taking the Fourier transform of Eq. (1.2.1) yields Eq. (1.2.2), where $\dot{K}(t) = G(t)$. The first line of Eq. (1.2.2) is obtained by recalling that the Fourier transform of a convolution is a product of the Fourier transforms. The second line pulls the derivative out of the transform.

$$\begin{aligned} \sigma(\omega) &= K(\omega)\dot{\epsilon}(\omega) \\ &= K(\omega)(i\omega)\epsilon(\omega) \\ &= G(\omega)\epsilon(\omega). \end{aligned} \tag{1.2.2}$$

The real part of dynamic modulus, $G'(\omega)$, (sometime called the storage modulus), describes the elastic response of the system, and the imaginary part, $G''(\omega)$ (called the loss modulus), gives the viscous response [87]. By comparing the magnitude of $G'(\omega)$ and $G''(\omega)$, we can examine the nature of this dynamic transition.

Viscoelastic transitions can be found a variety of materials. Strain softening is common in soil and other granulate materials [88]. Pseudoplastic flow (also called shear thinning) occurs in materials such as whipped cream and latex paint [89, 90]; and dilatant flow (shear thickening) arises in corn starch and water suspensions [91]. A key feature these transitions is the they are each fairly smooth. An example of this smooth change in physical properties of the system can be seen in Fig. 1.4. Here, both the storage and loss moduli are smooth increasing functions of ω. This smooth transition is in contrast to the dynamic transition observed in proteins. Zocchi and collaborators [92] find that the physical properties of the protein sharply change from elastic to viscous. Figure 1.5 shows that for frequencies less than 100 Hz, increasing the driving force can cause a dramatic softening of the system. They also

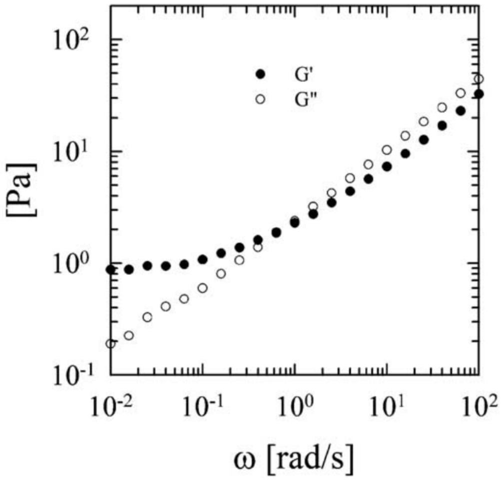

Figure 1.4: Stroage and loss moduli of corn starch

Plot from Byars *et al.* [91] of linear viscoelastic moduli, $G'(\omega)$ and $G''(\omega)$. The starch was jet-cooked under excess steam conditions, then combined with water to form a 10.2wt% corn starch suspensions. The suspensions is allowed to cool for 4 hrs while been stirred. Here we see that both $G'(\omega)$ and $G''(\omega)$ are increasing function of ω.

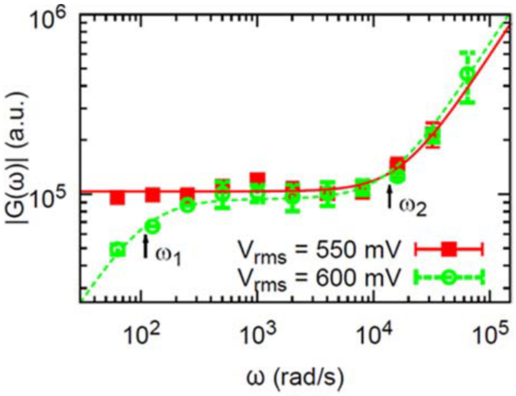

Figure 1.5: Magnitude of dynamic modulus in guanylate kinase protein
Plot from Wang *et al.* [92] of the magnitude of the dynamic modulus $|G(\omega)|$ (in arbitrary units). For a driving force of $V_{rms} = 550\,\mathrm{mV}$[red squares] the behavior is elastic. For $V_{rms} = 600\,\mathrm{mV}$ [green circles] the behavior is viscoelastic at low frequencies.

find that because the system is fundamentally non-linear, in that the dynamic modulus G depends on both the amplitude and frequency of the driving force.

1.3 Overview of thesis

Sections 1.2.1 and 1.2.2 reviewed morphological transitions in the shape of neutrophil nuclei and viscoelastic transitions in the dynamic response of globular proteins. In the remaining chapters we will investigate physical models inspired by these biological system. The principal feature of each model is that the system undergoes a phase transition. We can categorize these transition into two groups: continuous transitions and discontinuous transition. In a continuous phase transition, the properties of the system vary continuously. These transitions have a analog in second-order thermodynamic phase transitions [93]. Conversely, discontinuous phase transitions resemble first- order thermodynamic phase transitions. We use the term discontinuous here because these systems may not possess all of the characteristic in standard thermodynamic first-order phase transition (e.g.: coexistence of phases or latent heat) for all transitions expressed in the model, nonetheless, the properties of the system change abruptly. In this work, we will examine biological motivated systems exhibiting phase transitions in shape (Chapter 2) and in dynamic response (Chapter 3).

As discussed in Sec. 1.2.1, morphological transition in the nuclei of neutrophils is a very complex phenomenon. In our approach to this problem we have taken inspiration from other studies in which morphological transitions are driven by mass transport, such as studies of wrinkle formation in systems with growth constrained by displacement [94, 95] and surface stress [96]. A common tread in the studies is that non-linearities in the system lead to instabilities similar to standard Euler buckling[97]. In Chapter 2, we study a model system consisting of an isotropic elastic sphere (core) bound to a fluid membrane (shell). As in the case of most simple lipid bilayers, we assume that the membrane is tension-free and that it only supports bending energy. The increase in nuclear membrane surface area during differentiation is modeled by a uniform increase in area of the shell. We shall see that this system undergoes a sharp phase transition an a manner similar to other systems discussed above.

In Sec. 1.2.2 we consider the dynamics of viscoelastic transitions in globular proteins. In Chapter 3 we construct a simple model of a globular protein which consist of a predominantly elastic region and a non-linear softening of the system at a critical displacement. The elastic region can be thought of as the normal mode response of the system near an equilibrium conformation. The non-linear softening is analogous to the "cracking" process discussed in Sec. 1.2.2. However, we view it as the reversible breaking of a single — or more likely a set of — non-covalent bonds within the protein. Investigating this model both analytically and computationally, we find that it exhibits that a rich range of dynamical behaviors, including a sharp dynamical phase transition, driving-force-dependent symmetry breaking, and limit cycles (in the case in which inertial effect are included).

CHAPTER 2

Shape transitions in soft spheres regulated by elasticity

2.1 Introduction

Euler buckling is a well-known mechanical instability. For a beam of length L under axial compressive loads, there is a critical compressive strain $\sim L^{-2}$ at which its deformation switches discontinuously from axial compression to the lateral deflection [97, 98]. This mechanical instability and the breaking of the axial symmetry of the compressed beam by its lateral deflection provides a mechanical analogy to symmetry-breaking first-order phase transitions [99]. The role of Euler buckling in beams has, of course, been explored extensively in engineering and materials science [100], but it also plays an important role in biological physics in the context of buckling cytoskeletal filaments where such buckling affects force propagation along individual filaments [101], and the nonlinear mechanics [60, 102] and structural evolution under load [103] of their networks.

Similar buckling and wrinkling instabilities appear in elastic sheets [7, 104] under in-plane compressive stress. In cases where that compressive stress is generated by the growth or addition of material to a constrained system, morphological transitions induced by buckling result [105–108], and these are believed to have biological relevance in a variety of contexts including the formation of fingerprints [109] and intestinal structures — villi and crypts — that can be reproduced *in vitro* [110] and understood theoretically [111] by considering the buckling of a thin elastic and growing layer coupled to a thick elastic substrate. More generally, the appearance of wrinkling of a stiff thin elastic layer mechanically coupled to a soft, three-dimensional elastic substrate has been studied quite generally [94, 112–114] as has that of thin elastic layers coupled to a fluid substrate [115, 116]. The modifications of the buckling phenomenon arising from coupling the elastic sheet to the substrate are generically two-fold. First the coupling increases the critical load at which buckling first occurs, and second it modifies the wavelength of the buckled state near to the transition. The latter effect can be understood by noting that longer wavelength buckling lowers the elastic energy of the thin sheet, but generates deformations over longer length scales within the substrate at the cost of greater elastic energy there. The competition between these two elastic energies associated with the sheet and the substrate generate minimum energy buckled state at some intermediate wavelength. Without that competition, the buckling wavelength is controlled entirely by the system size, as it is in the archetypal case of Euler buckling in beam.

Morphological transitions can also be induced in compact elastic bodies, including a variety of core-shell structured spheres. In this article, we explore the surface wrinkling of a spherical elastic object bounded by a membrane, which supports bending stresses. Motivated primarily by the observation surface buckling of a giant unilamellar vesicle filled with an elastic gel as their interior gel was osmotically shrunk [117], we examine theoretically morphological transition driving by an increase in the surface area of the membrane-bounded sphere for fixed interior content. For sufficiently small amounts of excess area, the system simply expands isotropically. At a critical value of the excess area, however, the sphere buckles into a lower symmetry shape. We have determine the critical excess area and optimally buckled shape within a linear elastic analysis. More broadly, these results should be relevant to morphological transitions in a number of elastic core-shell structures [118] and even the cell nucleus [119].

The remainder of the chapter is organized as follows. In Sec. 2.2.1 we first present the results of a heuristic model replacing the interior elastic deformation field with a scalar Laplacian model. This theory provides insight into the single control parameter for the morphological transition and the basic competition between the elastic energy cost of surface deformation favoring buckling at longer wavelengths and interior strain favoring buckling at shorter wavelengths. In Sec. 2.2.2 we present the full elastic calculation. In Sec. 2.3 we examine the solution and analyze the sharp buckling transition and determine the dominant deformation mode in the buckled state. We find a first order transition to a buckled state identified as a spherical harmonic mode $Y_{\ell m}$ with $\ell \sim \mathcal{O}(10)$ for a broad range of the relevant elastic parameters and $m = \ell$, although there are typically generated m states for larger ℓ. Finally, we conclude in Sec. 2.4 with a discussion of the implications of these results to current experiments and proposals for future tests. A few details of a more technical nature are relegated to the appendix.

2.2 The model

2.2.1 Scalar model

It is helpful to first examine a heuristic model that dramatically simplifies the elastic calculation of the interior of the sphere, but still manages to capture the basic competition between surface and bulk elastic energies. To that end we replace the vectorial elastic displacement field $\mathbf{u}(\mathbf{x})$ by a scalar field $\phi(\mathbf{x})$ that obeys the Laplace equation rather than the usual equation of stress continuity in a bulk elastic medium. In this way we neglect the distinction between transverse and longitudinal modes of the solid, but retain the basic power counting of derivatives in the equation of stress continuity, which is necessary for our argument. We impose "excess area" on the surface of the elastic sphere of radius R by requiring the scalarized deformation to be given there by

$$\phi(r = R, \theta) = \Phi P_\ell(\cos\theta), \tag{2.2.1}$$

where P_ℓ is a Legendre polynomial and θ is the polar angle. In this way we impose a deformation on the surface in the form of a spherical harmonic. In the scalarized approach we specialize to azimuthally symmetric modes ($m = 0$), but this is not essential and is relaxed in the full calculation presented below. The surface deformation can be thought of as being imposed by a set of normal stresses on the sphere's surface that serve as a method for injecting excess area on the surface. The morphological transition can be understood as resulting from either imposing excess surface area or reducing the interior volume of the unstrained material. For example, shape transitions are observed when gel-filled vesicles are osmotically shrunk [117]. In either case, the application of surface stresses is equivalent to changing the reference state within linear elasticity theory – see Appendix 2.E for a more detailed discussion.

Given that $\phi(\mathbf{x})$ satisfies the Laplace equation, a solution satisfying the above condition is given in terms of the polar angle θ and radial distance r from the origin of the coordinate system at the center of the sphere by

$$\phi(r,\theta) = \Phi\left(\frac{r}{R}\right)^{\ell} P_{\ell}(\cos\theta). \tag{2.2.2}$$

The deformation energy of the elastic interior is

$$E_{\text{bulk}} = \frac{\gamma}{2}\int_{r<R} d^3\mathbf{x}\,(\boldsymbol{\nabla}\phi)^2\,, \tag{2.2.3}$$

where γ is the single elastic constant in the scalarized elastic model, which has dimensions of energy per length. Inserting the solution Eq. (2.2.2) into Eq. (2.2.3), we find that

$$E_{\text{bulk}} = 2\pi\gamma R\Phi^2\left[\frac{1+\ell(\ell+1)}{(2\ell+1)^2}\right]. \tag{2.2.4}$$

The prefactors associated with the elastic constant, sphere's radius, and magnitude of deformation follow naturally from dimensional analysis; the ℓ-dependent term in square brackets, however, shows that higher order spherical harmonics (of the same amplitude) generate less elastic energy storage in the interior. In terms of the energy of the $\ell = 0$ mode $E_0 = 2\pi\gamma R\Phi^2$, the elastic energy associated with the ℓ^{th} mode decays monotonically with ℓ to the limiting value of $E_{\text{bulk}} \to \frac{E_0}{4}$ as $\ell \to \infty$.

We now introduce a bending energy associated with the surface deformation imposed by $\phi(\mathbf{x})$, specified in Eq. (2.2.1). Letting $\boldsymbol{\nabla}_{\perp}$ be the parts of the gradient operator normal to the radial direction, we approximate this bending energy as

$$E_{\text{surf}} = \frac{\tilde{\kappa}}{2}R^2\oint_{r=R} d\Omega\left[\nabla_{\perp}^2\phi\right]^2, \tag{2.2.5}$$

where $\tilde{\kappa}$ is the bending energy, which, in the scalarized model, has dimensions of length squared times energy. This form of the bending energy is correct only for small deformations

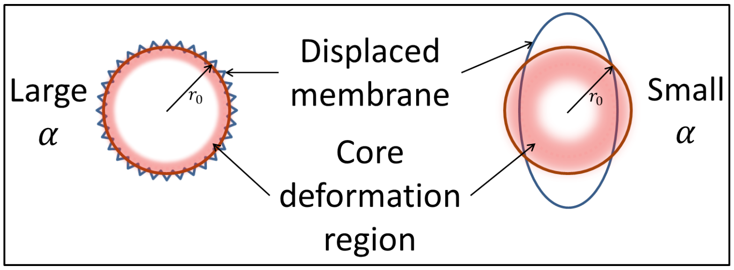

FIGURE 2.1: SCHEMATIC REPRESENTATION OF THE ENERGY BALANCE

A schematic representation of the basic energy balance between the surface and the bulk. By inserting excess surface area in a short wavelength deformation as shown on the left, the deformation field in the interior decays rapidly, minimizing bulk elastic energy at the cost of the incurring high bending energy on the surface. Inserting the same excess area into a lower spherical harmonic, as shown on the right, exchanges the relative importance of surface and bulk energetic contributions. This trade off between bulk and surface energy selects a optimally buckled state with $\ell \sim \alpha^{1/3}$. See text for details.

from an originally flat surface, so it is approximate in this case and can only be justified *a posteriori* by showing that energy minimizing buckling wavelength is small compared to the sphere's circumference – see below. In the full calculation, shown in the next section, such approximations are not used. Using the solution Eq. (2.2.2) we find the bending energy to be given by

$$E_{\text{surf}} = \frac{2\tilde{\kappa}\pi\Phi^2}{R^2}\left[\frac{\ell^2(1+\ell)^2}{2\ell+1}\right]. \tag{2.2.6}$$

The total energy cost for a given deformation in mode ℓ, E_ℓ, is given by the sum of the energetic contributions from the bulk Eq. (2.2.4) and the surface Eq. (2.2.6). To determine the minimum such energy for a given *excess surface area* ΔA we first compute the "excess area" associated with the deformation ϕ,

$$\Delta A = \frac{R^2}{2}\oint d\Omega \left[\boldsymbol{\nabla}_\perp \phi\right]^2, \tag{2.2.7}$$

and use this result to eliminate the amplitude of the deformation field Φ in favor ΔA. Defining a dimensionless energy $\mathcal{E}_\ell = R^2 E_\ell / 2\pi\tilde{\kappa}$ we find that the energy of a deformation in the Y_ℓ^0

mode generating excess surface area ΔA is given by

$$\mathcal{E}_\ell = \frac{\Delta A}{\ell(\ell+1)}\left[\tilde{\alpha}\frac{1+\ell(\ell+1)}{2\ell+1} + \ell^2(\ell+1)^2\right], \tag{2.2.8}$$

where we have introduced a single dimensionless control parameter

$$\tilde{\alpha} = \frac{\gamma R^3}{\tilde{\kappa}}. \tag{2.2.9}$$

This dimensionless constant describes the relative stiffness of the interior as compared to the surface. For large ℓ one notes that the dimensionless energy in Eq. (2.2.8) is given roughly by

$$\frac{\mathcal{E}_\ell}{\Delta A} \sim \frac{\tilde{\alpha}}{\ell} + \ell^2, \tag{2.2.10}$$

showing that a minimum exists for a mode at

$$\tilde{\ell}^\star \sim \tilde{\alpha}^{1/3}. \tag{2.2.11}$$

The key features determining the form of Eq. (2.2.10) can be readily understood. The $\frac{\tilde{\alpha}}{\ell}$ and ℓ^2 represent the energetic contribution from the interior and the surface respectively. The growth of $\mathcal{E}_\ell$ at large ℓ reflects the high bending energy cost of the high ℓ modes, but the first term, weighted by the ratio of the bulk to surface modulus, decreases with increasing ℓ. The deformation field in the sphere's interior becomes confined to a type of boundary layer: $\phi \sim (r/R)^\ell$. Figure 2.1 shows a schematic representation of this trade off between the confinement of the interior strain to a boundary layer at high ℓ, leading to the reduction of the bulk energy and the monotonically growing bending energy cost of injecting a fixed amount of excess surface area into a mode with increasing ℓ.

The qualitative features of this result will survive the introduction of a proper vectorial displacement field to describe the deformation state of the sphere. In that case we will replace the dimensionless control parameter $\tilde{\alpha}$ by

$$\alpha = \frac{\mu R^3}{\kappa}, \tag{2.2.12}$$

where μ is the shear modulus of the bulk and κ is the bending modulus of the surface. Ignoring a weak dependence on the Poisson ratio of the bulk elastic material, we will find a similar structure of the total energy yielding, a transition from a spherical state to deformation in the mode $\ell^{\star}$. The generic nature of the result is not surprising in light of previous work on buckling of beams embedded in an elastic medium [120]. In that case, the beam is generically stiffened against buckling by the surrounding medium and the unstable mode associated with the buckled state shifts from the lowest wavelength allowed by the length of the beam to a finite wavelength set by the ratio of the beam's bending modulus and the elastic constants describing the surrounding medium [120]. The finite wavelength results from the fact that the continuum elastic theory is Laplacian. Undulations of the beam at wavevector k generate strain in the elastic continuum that decays over a distance $1/k$ into the medium. This sets up the same trade off between beam bending energy and bulk elastic energy as discussed here. The key differences in the present calculation involve the spherical geometry of the undeformed structure, which renders the calculation more difficult.

2.2.2 Full elastic calculation

To calculate the energy associated with the membrane bounding the elastic sphere we introduce the energy of that surface that depends on the mean curvature H, the spontaneous curvature $H_s = 1/R_s$, and a single elastic constant, the bending modulus κ:

$$E_{\text{surface}} = \frac{\kappa}{2} \oint_{\mathcal{S}} dS \left(H - H_s\right)^2 , \tag{2.2.13}$$

where $\mathcal{S}$ and dS are the deformed surface and its metric respectively. Because the membrane is fluid, it does not support a shear stress, therefore, the Helfrich energy [5] is the only energy involving the membrane. The details of this calculation are in Appendix 2.A.

To determine the elastic energy stored in the sphere's interior, we parameterize the strain in the usual way by introducing the symmetrized deformation tensor $u_{ij} = (1/2)[\partial_i u_j + \partial_j u_i]$ calculated from the displacement field $\mathbf{u}(\mathbf{x})$ defined everywhere within the undeformed body, a sphere of radius R. The elastic properties of the interior are described in terms its shear modulus $\mu > 0$ and the Poisson ratio $-1 < \nu < 1/2$, with $\nu = 1/2$ corresponding to an incompressible solid. In terms of these parameters the elastic energy associated with a given deformation state of the sphere is given by [97]

$$E_{\text{bulk}} = \mu \int_{|\mathbf{x}|<R} d^3x \left(\frac{\nu}{1-2\nu} u_{ii}^2 + u_{ij}^2 \right). \tag{2.2.14}$$

The integral is over the reference space of the undeformed sphere. The above strain tensor satisfies the standard stress continuity equation $\partial_i \sigma_{ij} = 0$ within the sphere requiring that $\mathbf{u}$ satisfy

$$\frac{1}{1-2\nu} \boldsymbol{\nabla}\boldsymbol{\nabla} \cdot u + \nabla^2 \mathbf{u} = 0. \tag{2.2.15}$$

The total energy of deformation, which is the sum of the contributions from Eqs. (2.2.13) and (2.2.14) is fully determined once one requires that the state of deformation of the elastic interior matches the imposed normal displacements at its boundary surface, $r = R$. To do that we require the normal displacements obey

$$\mathbf{u}(R, \theta, \phi) \cdot \hat{\mathbf{r}} = R\, g(\Omega), \tag{2.2.16}$$

with $\Omega = (\theta, \phi)$ representing the polar and azimuthal angles. Since we consider a fluid membrane boundary and look at static states of deformation, the tangential displacements of the elastic core $\mathbf{u}_\perp(r = R, \Omega)$, $\mathbf{u}_\perp \cdot \hat{r} = 0$ do not affect the deformation energy of the surface. We take these displacements to be zero for now and return to this point later in the discussion.

Following the analysis of the heuristic model above, we impose a deformation on the surface of the sphere so that the radial distance $r(\Omega)$ from its center to the deformed boundary is expanded in spherical harmonics [12]. In other words

$$r(\Omega) = R\left[1 + g(\Omega)\right] = R\left[1 + \sum_{\ell,m} g_{\ell m} Y_{\ell m}(\Omega)\right]. \tag{2.2.17}$$

In order to make the radial deformation of the sphere explicitly real, we have introduced linear combinations of the complex spherical harmonics Y_ℓ^m for $m > 0$

$$Y_{\ell m} = \tfrac{1}{\sqrt{2}} \left[Y_\ell^m + (-1)^m Y_\ell^{-m} \right], \tag{2.2.18}$$

and set $Y_{\ell 0} = Y_\ell^0$ for the azimuthally symmetric mode. Other linear combinations of the spherical harmonics of the form $Y_\ell^m e^{im\phi_0} + (-1)^m Y_\ell^{-m} e^{-im\phi_0}$ correspond to the same deformation state, but simply rotated azimuthally by ϕ_0. As such, they are not interesting, at least until one considers the energy cost of linear combinations of such deformation modes. Finally, it will prove convenient to rescale the amplitude the $\ell = 0$ mode by introducing the notation $\bar{g}_0 = g_0/\sqrt{4\pi}$.

Since the surface energy Eq. (2.2.13) is quadratic in the deformations, the spherical harmonic decomposition of the surface deformation energy yields a result quadratic in amplitudes $g_{\ell m}$ for $\ell \neq 0$.

$$\begin{aligned} E_{\text{surface}} = {} & \bar{E} + 2\pi\kappa\bar{g}_0\omega_s\left[\omega_s(2+\bar{g}_0) - 2\right] + \\ & + \frac{\kappa}{8}\sum_{\ell\neq 0, m\geq 0} g_{\ell m}^2 \Big[\ell(\ell+2)(\ell^2-1) - 4\omega_s\ell(\ell+1) \\ & + 2\omega_s^2(\ell^2+\ell+2)\Big], \end{aligned} \tag{2.2.19}$$

where $\omega_s = R/R_s$ is the ratio of the undeformed sphere's radius to the spontaneous curvature of its bounding membrane, and $\bar{E} = 2\pi\kappa\left(1-\omega_s\right)^2$ is the energy associated with the mismatch ($\omega_s \neq 1$) between these quantities (see Appendix 2.C of details).

Such a mismatch $\omega_s \neq 1$ leads to a "prestress" in the membrane-sphere system due to the incompatibility of their undeformed states. We do not explore these effects here, but it is clear that the prestress above can lead to buckling at zero excess area.

We may also calculate change in surface area associated with the deformation of the sphere. Keeping terms to $\mathcal{O}(g^2)$ we find

$$\frac{A}{4\pi R^2} = \left(1+\bar{g}_0\right)^2 + \frac{1}{8\pi R^2}\sum_{\ell\neq 0, m} g_{\ell m}^2\left[\ell^2+\ell+2\right]. \tag{2.2.20}$$

The first term is the extra area associated with the uniform change in the sphere's radius, i.e., the $\ell = 0$ mode. The second term gives the contributions from all the higher modes of deformation $\ell > 0$. Both the results for the bending energy and contribution to the surface area are consistent with previous work on the undulations of micelles [12]. In the following we will consider the fractional excess area Δ of the deformed sphere as the control parameter for the transition from spherical to deformed shapes. Consequently, we define

$$\Delta = \frac{A}{4\pi R^2} - 1. \tag{2.2.21}$$

The surface energy Eq. (2.2.19), and the excess area Eq. (2.2.20) both take the form of sums of terms each proportional to the square of the spherical harmonic mode amplitudes. This will also be true of the elastic energy stored in the sphere's interior Eq. (2.2.14). Thus, in a deformation state given by a linear combination of such modes, the contributions of each mode to both the energy cost and excess surface area are simply additive. For this reason it is sufficient to consider a single spherical harmonic mode at a time.

The remaining calculation of the energy stored in the elastic interior is somewhat tedious; we present the key features of the calculation here and the remaining details in Appendix 2.D. Our method of solution has been used to consider the deformations of spherical inclusions embedded in another elastic medium [121], but we consider the problem with displacement, rather than stress, boundary conditions at the surface. To briefly describe the approach: if one were to obtain a harmonic vector $\mathbf{S}_{\ell m}(\mathbf{x})$ i.e., $\nabla^2\mathbf{S} = 0$ that matches the boundary conditions imposed on the displacement field at the boundary $r = R$ so that $\mathbf{S}(r = R, \Omega) = \hat{\mathbf{r}} g_{\ell m} Y_{\ell m}(\Omega)$, then a displacement field of the form

$$\mathbf{u}(\mathbf{x}) = M_\ell (R^2 - r^2) \boldsymbol{\nabla}\boldsymbol{\nabla} \cdot \mathbf{S}_{\ell m} + \mathbf{S}_{\ell m}, \tag{2.2.22}$$

with

$$M_\ell = \frac{1}{4(1-\nu)(2\ell - 1) - 2\ell}. \tag{2.2.23}$$

is a solution to Eq. (2.2.15) with the correct boundary conditions, as may be checked by direct computation.

Recognizing that $Y_{\ell m}$ is a linear combination of complex spherical harmonics $Y_\ell^{\pm m}$, it is sufficient to produce a complex harmonic vector field $\mathcal{S}$ that generates the appropriate part of the radial displacement at the surface:

$$\mathcal{S}(r = R, \Omega) = \hat{\mathbf{r}} Y_\ell^m(\Omega). \tag{2.2.24}$$

The Cartesian components of such a complex vector are products of $\hat{r} \cdot \hat{e}_i$, $i = x, y, z$ and Y_ℓ^m. Using the usual rules for adding angular momentum, such products can be expanded in spherical harmonics having $\ell' = \ell - 1, \ell, \ell + 1$ and $m' = m - 1, m, m + 1$ with coefficients given by the Clebsh-Gordon coefficients. The net result is a displacement field that gives the appropriate radial displacement on the surface in a single $Y_{\ell m}$ mode, but contains a sum of terms including that mode as well as modes with $\ell \pm 1$ (and $m \pm 1$) in the interior. Taking the necessary derivatives, one obtains the strain tensor and, from that, the elastic energy density. Integrating the energy density over the volume of the sphere, we obtain the total bulk elastic energy. That result, combined with Eqs. (2.2.19) and (2.2.20), completes our analysis of the geometry and energetics of the sphere held in a deformed state. As in the heuristic example, it is necessary only to eliminate the amplitude of the surface deformation in favor of the true control variable, the excess area (using Eq. (2.2.20)). For a deformation consisting of a single harmonic with ℓ this leads to

$$g_{\ell m}(\Delta) = \begin{cases} \sqrt{4\pi}\left(\sqrt{1+\Delta} - 1\right) & \text{for } \ell = 0 \\ \sqrt{\Delta}\left(\frac{8\pi}{\ell(\ell+1)+2}\right)^{1/2} & \text{for } \ell \neq 0 \end{cases}, \tag{2.2.25}$$

where the fraction excess area Δ is defined by Eq. (2.2.21).

For small Δ, the amplitude of the $\ell = 0$ mode grows as $g_{00} \sim \Delta$. For all other modes with $\ell > 0$ the amplitude grows as $g_{\ell m} \sim \Delta^{1/2}$. Since the deformation energies of both the surface and the bulk are proportional to g^2 (when $\omega_s = 1$, i.e., no prestress), the energy cost for inserting the the excess area into the $\ell = 0$ mode grows as Δ^2. For the $\ell > 0$ modes, however, it grows linearly.

Thus, for sufficiently small Δ, the isotropic deformation is necessarily lower in energy. At some ℓ- and m-dependent values of the excess area, the energetic cost storing that excess area in these finite ℓ modes must become lower than storing it in the isotropic one. At that point a morphological transition results. This is illustrated in Fig. 2.2 which shows the non-dimensionalized energy of the system $\mathcal{E} = E/\kappa$ as a function of the fractional excess area Δ – see Eq. (2.2.21) – in three cases: Accommodating that excess area by isotropically expanding the sphere and membrane system (sold line, gold) or by fractional excess area creating a

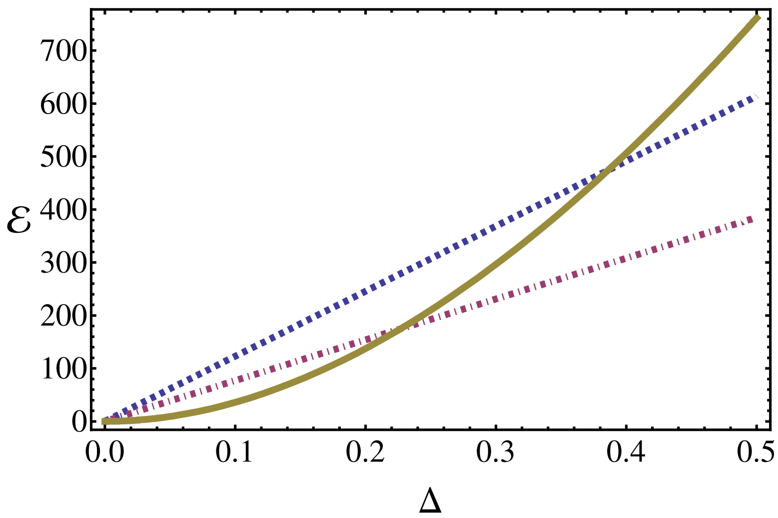

Figure 2.2: Energy vs. Fractional excess area

The dimensionless energy $\mathcal{E} = E/\kappa$ of the deformed sphere and membrane as a function of the fractional excess area Δ for isotropic growth $\ell = 0$ solid (gold) and for buckling into the $\ell = 8, m = 0$ dashed (blue) mode or the $\ell = 8, m = 8$ dot-dashed (purple). The dimensionless control parameter is $\alpha = 575$ and the Poisson ratio of the interior is $\nu = 0.2$. As discussed in the text, the $\ell = 8, m = 8$ mode is the minimum energy buckled state of the sphere. The transition from isotropic expansion to buckling occurs at $\Delta \approx 0.22$.

lower symmetry buckled state in the $\ell = 8, m = 0$ (dashed line, blue) or $\ell = 8, m = 8$ (dashed dotted line, purple) mode. It is clear that there is a transition near $\Delta^\star \simeq 0.22$ where the isotropic solution is no longer the energy minimizing solution.

As with the heuristic toy model, α – see Eq. (2.2.12) – is the key dimensionless parameter controlling both the fractional critical excess area of the transition $\Delta^\star$ and the symmetry of the optimally buckled state above the transition $\ell^\star$. The Poisson ratio of the elastic material inside the sphere has a weak effect on the quantitative results as long as $\nu < 1/2$, i.e., as long as the material is not strictly incompressible. We return to this point in the next section. Of the three cases shown, the optimal solution is the $\ell = 8, m = 8$ one; it will be shown later that, for these parameters giving $\alpha = 575$ and $\nu = 0.2$, there are in fact six degenerate optimal solutions with $\ell = 8$ and $m = 3, \ldots, 8$. In the next section we survey the dependence of the buckling transition on α, examine the buckled state more closely, and present an overall phase diagram of core/shell buckling.

2.3 Results

Having seen that a buckling transition is required from a basic scaling analysis, we examine in more detail which buckled configuration is an energy minimum and which material parameters control the symmetry of the optimally buckled shape. To determine which is the optimally buckled shape above the transition, i.e., for $\Delta > \Delta^\star$, we plot the dimensionless energy $\mathcal{E}$ as a function of the angular harmonic ℓ, using the same values of the material parameters as above ($\alpha = 575$ and $\nu = 0.2$). A representative example is shown in Fig. 2.3 in which the energy of the buckled sphere is plotted for buckling mode $\ell, m = 0$ (dashed dot, blue), and $\ell, m = \ell$ (dashed, purple). For comparison, we show the energy of the isotropically expanded state as a solid (gold) line. In all cases the fractional excess area is fixed at $\Delta = 0.5 > \Delta^\star \simeq 0.22$, so some lower symmetry state of the system is the energy minimum. Here, we see that the $\ell^\star = 8$ state with large m is the lowest energy buckled state of the system. We will find that the larger m solutions for a given ℓ are, in fact, generically of lower energy.

Repeating this exercise for various values of α, one determines both the dependence of the critical fractional excess area $\Delta^\star$ and the symmetry of the minimum energy buckled state $\ell^\star$ on the control parameter α. The results for the dependence of $\ell^\star$ upon α are shown in Fig. 2.4 for two different values of the fractional excess area: $\Delta = 0.4$ dashed (blue) and $\Delta = 0.25$ solid (red). As expected based on the heuristic model, we find that $\ell^\star \sim \alpha^{1/3}$, as shown by a comparison to the cube root function dashed by the dashed line in the figure. For sufficiently small values of α the interior of the sphere is too compliant to drive the buckling transition; the isotropic deformation of the sphere is the energetically favored manner of storing the excess surface area. Collecting more results of this form, we observe that the critical fractional excess area decreases with increasing α for fixed Poisson ratio as $\Delta^\star \sim \alpha^{-1/3}$, as is discussed later in terms of the overall buckling phase diagram.

The dependence of these results on the Poisson ratio is generically weak – see Fig. 2.5

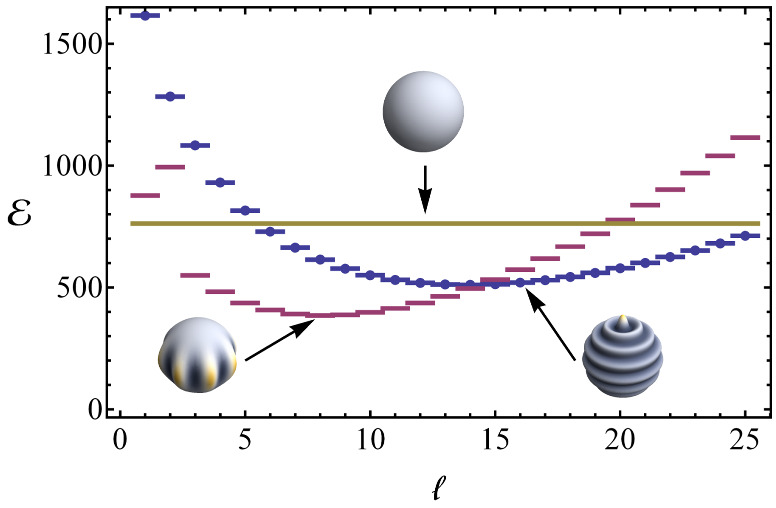

Figure 2.3: Energy vs. Angular harmonic of buckled state

Plot of the dimensionless energy $\mathcal{E} = E/\kappa$ vs. the angular harmonic of the buckled state ℓ for $\alpha = 575$, $\nu = 0.2$, and fixed fractional excess area $\Delta = 0.5$. These plots can be used to determine the optimal buckled state symmetry $\ell^{\star}$. The solid (gold) line shows the energy of the isotropically expanded state. The dashed (red) curve gives the energies of the $\ell = m$ state and the dot dashed (blue) curve the energies of the $m = 0$ state at each ℓ. For this α, ν combination the lowest energy configuration at $\Delta = 0.5$ is given by $\ell = m = 8$. Representative figures of the isotropic state (top), the $\ell = m = 8$ state (bottom left) and the $\ell = 16, m = 0$ (bottom right) are shown.

– except in the singular limit of $\nu \to 1/2$ where the material becomes incompressible. As ν approaches 1/2, the symmetry of the optimally buckled state is gradually reduced. A more incompressible interior results in more wrinkles for the buckled state. As expected, the energy cost of the isotropically expanded sphere increases without bound as the sphere's interior is made more incompressible. Consequently, the critical value of the excess fractional area Δ decreases continuously with increasing ν. Finally at $\nu = 1/2$ the isotropic solution is disallowed by the compressibility condition and buckling occurs for all $\Delta > 0$ and all α.

2.3.1 Energy dependence on azimuthal mode

When examining the energy of various buckled states for the same ℓ, one notes that it is a non-increasing function of m. The buckled states having rings of equal radial deformation

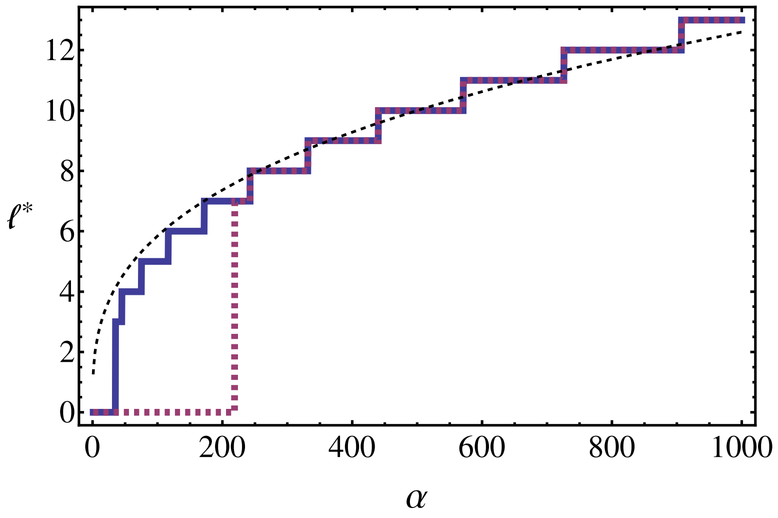

FIGURE 2.4: ANGULAR HARMONIC IN MINIMUM ENERGY STATE VS α

Plot of $\ell^\star$, the angular harmonic of the minimum energy state of the sphere as a function of α for fixed fractional excess areas $\Delta = 0.25$ dashed (purple) and $\Delta = 0.4$ solid (blue). For sufficiently soft interiors (small α) the isotropic shape is the energy minimum. As α is increased, the sphere transitions to a buckled state with $\ell^\star$, and $m = \ell^\star$. As expected from the heuristic treatment of scalarized elasticity, symmetry of the optimally buckled state $\ell^\star \sim \alpha^{1/3}$, as shown by the dashed (black) line.

extending azimuthally around the sphere, e.g., the $m = 0$ state is always the highest energy state with the subspace of equal ℓ buckled configurations. As m is increased, the energy initially decreases within increasing m, but reaches a plateau for $m \geq 3$ independent of ℓ for $\ell > 3$. An example of this degeneracy is shown in Fig. 2.7 for the $\ell = 8$ with the same combination of α, ν as used in the previous figures. The fractional excess surface area is fixed at $\Delta = 0.5$.

This can be understood as examining the forms of elastic energy in both the bulk and the membrane. Referring to Appendix 2.D for the form of the bulk elastic energy, we see that the displacement field in the sphere's interior associated with a surface deformation proportional to $Y_{\ell m}$ contains terms with angular dependence given by a sum of spherical harmonics with $m-1, m, m+1$. The elastic energy density requires one more spatial gradient of $\mathbf{u}(\mathbf{x})$. The gradient of spherical harmonics has the effect of shifting the azimuthal mode by 0 or ±1.

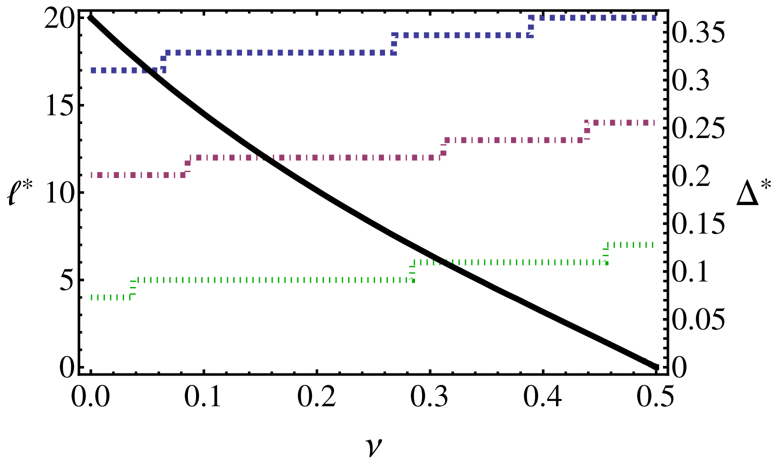

Figure 2.5: Angular harmonic in minimum energy state vs ν

Plot of $\ell^\star$, the angular harmonic of the minimum energy state of the sphere as a function of ν for $\alpha = 100, 800, 2500$: dotted (green), dash-dotted (purple), and dashed (blue) respectively. As the interior is made less compressible, the optimally buckled shape has lower symmetry, i.e., higher $\ell^\star$ (left axis). Additionally, the critical fractional excess area $\Delta^\star$ (black line, right axis) decreases continuously to zero as $\nu \to 1/2$, the incompressible limit, for fixed $\alpha = 575$.

As a result, the bulk elastic energy density will contain a sum of terms having azimuthal mode numbers of $m-2, \ldots, m+2$. Notice that this is the case only in within linear elastic theory. We believe that nonlinear elastic terms well either product additional derivatives and/or greater powers of g_θ and g_ϕ, which would break this degeneracy.

This degeneracy is also present in the bending elastic energy term. To compute the bending elastic energy we need to find both the curvature and the metric of the deformed surface as shown in Appendix 2.A. The normal vector (Eq. (2.A.4)) and the metric (Eq. (2.B.4)) both of the deformed surface contains square root. This is significant because the full Taylor series expansion of square root would g_θ and g_ϕ to all orders. Using relations found in [122–124] it can be shown that products of spherical harmonics can be rewritten as a sum of spherical harmonics with Clebsch-Gordan coefficients. This would produce spherical harmonics with ℓ and m values over a large range. However, because we only keep terms up to $\mathcal{O}(g^2)$ only values in the range of $m-2$ to $m+2$ are produced.

Recall also our spherical harmonics $Y_{\ell m}$ are superpositions of complex spherical harmonics

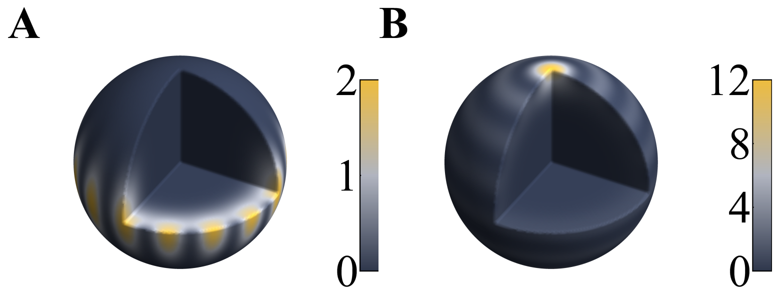

Figure 2.6: Comparison of energy distribution for different azimuthal modes

A comparison of the distribution of the elastic energy density in spheres having the same fractional excess area $\Delta = 0.5$, and same elastic parameters $\alpha = 575, \nu = .2$. On the left (A) the excess area is put into the $\ell = 8, m = 8$ mode. Here the energy density is primarily spread out over the equator. On the right (B) the excess area is put into the $\ell = 8, m = 0$ mode so that the sphere's surface has undulatory rings that run along lines of constant latitude. The overall elastic energy of A is less than B – note the difference in the energy scale associated with the two color maps.

with $\pm m$ so that the volume integral of the bulk energy density contains an array of products of terms having magnetic quantum numbers between $-m-2, \cdots - m+2$ and $m-2, \ldots m+2$. Cross products between these two sets of terms vanish upon integration unless the sum of their magnetic quantum numbers vanishes. There are more such products, however, if these two sets of terms have an overlap; in other words if $m \leq 2$, then there is an accessible solution to $-m+2 = m-2$ and more products are nonvanishing in the computation of the internal energy of the sphere. These terms necessarily make a positive contribution to the elastic energy of the sphere since every deformation adds to the elastic energy. Thus as m is increased, the number of these cross terms is reduced as and the total elastic energy of deformation decreases. Once $m \geq 3$, however, there are no more cross terms. It is important to emphasize that this degeneracy is not a fundamental feature of this system. Rather it is due to fact that the calculate is within the limits of linear elastic theory and the elastic energy is only computed up to second-order in the displacement field. For the reasons stated above we believe that relaxing these conditions would lift degeneracy, but such effects are beyond the scope of the current analysis.

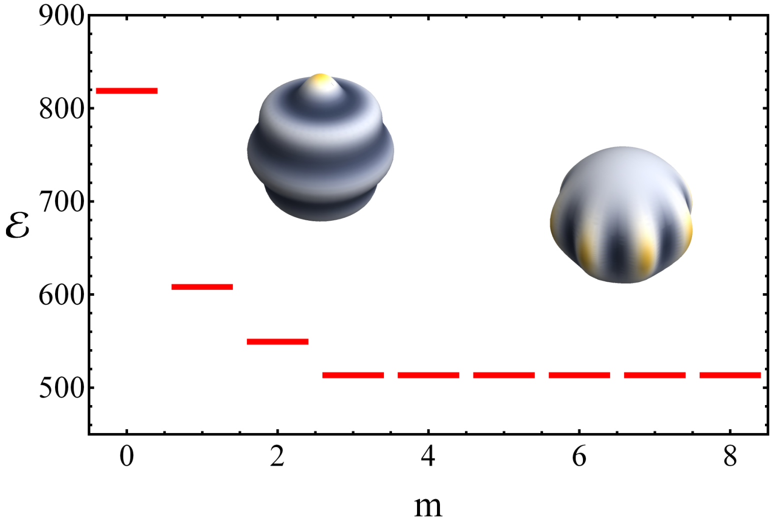

FIGURE 2.7: ENERGY AT FIXED ANGULAR HARMONIC VS. AZIMUTHAL MODE
Example of the degeneracy of the buckled state energy with respect to m for a representative value of $\ell = 8$ and $\alpha = 575, \nu = 0.2$ and excess fractional area of $\Delta = 0.5$. For fixed ℓ the energy initially decreases with m until $m = 3$. All states with $m \geq 3$ are generate. Superposed on the plot are pictorial representations of the higher energy state with $m = 0$ (left) and one of the lowest energy states with $m = \ell = 8$ (right).

The physical effect of these extra terms in the energy density is well illustrated by plotting the distribution of elastic energy storage in two spheres with $\ell = 8$ surface deformations. Their energy densities are shown as a heat map in Fig. 2.6 for the $m = 0$ (left) and the $m = 8$ (right) solutions. The $m = 0$ mode is clearly higher in energy as can be seen by noting the difference between the two color scales. From a comparison of the two figures, it is clear that in both cases the elastic deformation energy is confined to a boundary layer near the sphere's surface, as expected based on the heuristic calculation. In the $m = 0$ solution, however, there is a distinct concentration of the elastic energy near the sphere's poles. This is due to the fact that $m = 0$ distortion lay along lines of longitude. Near the poles these undulatory rings of deformation become tightly wrapped. In the $m = 8$ solution the elastic energy is spread out primarily over the equator of the sphere, resulting in a lower total energy.

2.3.2 Phase diagram and mixed mode configurations

Putting these results together into a more unified picture, we present a phase diagram for spherical elastic core/membrane shell structures in Fig. 2.8. The diagram is spanned by the fractional excess area Δ and the control parameter α for a fixed value of the Poisson ratio $\nu = 0.2$. This phase diagram is representative of other ν values with the exception of the $\nu = 1/2$ incompressible case, as mentioned above. The solid black in Fig. 2.8 line divides the the phase space of such elastic objects into isotropic and expanded spheres below line and lower symmetry buckled ones above it. One also observes the dependence of the critical fractional excess area on α. As α is increased $\Delta^\star$ indeed decreases and the symmetry of the

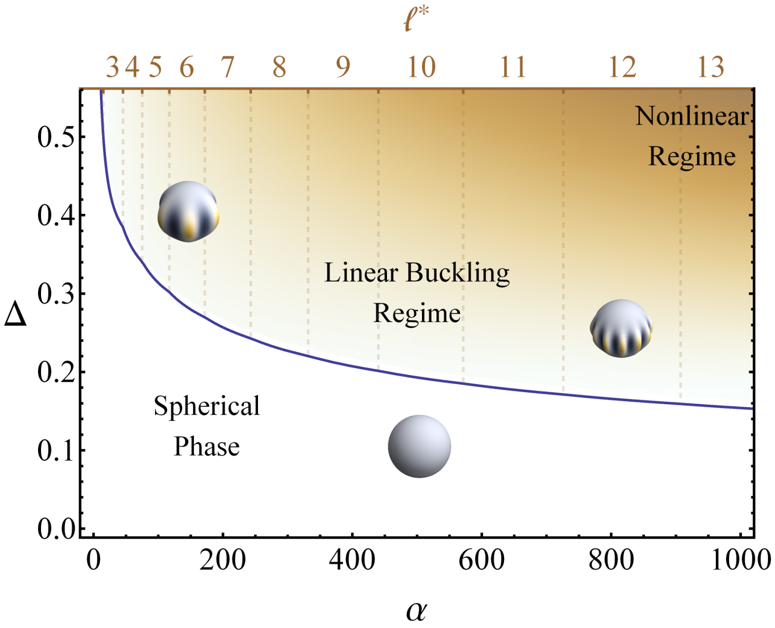

Figure 2.8: Fractional excess area vs α

Buckling phase diagram of core-shell structures spanned by the fractional excess area Δ and the dimensionless control parameter α. The (solid, black) curve separates isotropically expanded spheres from lower symmetry buckled states. As $\alpha = \mu R^3/\kappa$ is increased the interior material stiffens relative to the bending modulus of the boundary, leading to buckling at smaller Δ. Also, as α is increased the $\ell^\star$ of the buckled state near the transition also increases – see the top axis. Representative shapes for these minimum energy buckling spheres are shown for $\ell^\star = 6, 12$.

buckled state decreases as well. The angular harmonic of the optimal buckled state $\ell^\star$ is shown by the horizontal axis along the top of the figure. The representative figures show the $\ell = m$ state, which, as described earlier, is always part of the degenerate subspace of optimally buckled shapes for $\ell^\star \geq 3$. Such buckled shapes are qualitatively similar to the buckled gel-filled vesicles of [117, 125].

There are a variety of other buckled core shell structures. In particular, Cao and coworkers investigated the buckling of Ag core/ SiO_2 shell particles experimentally [126] and numerically [118], where, relying the materials' differential thermal expansion, buckling was induced by temperature change. In these systems, a triangular pattern of ridges where observed near the transition from the smooth spherical state, while, deeper the buckled phase, labyrinthine patterns were observed. The triangular patterns observed near the transition have lower symmetry than an single spherical harmonic mode predicted by the linear theory. Such triangular patterns, however, can be simply reproduced from out results by forming a linear superposition of the degenerate buckling modes predicted herein. This is shown in Fig. 2.9 where we reproduce examples of lower symmetry buckling states by combining degenerate buckling modes all with $\ell = 8$. One generically finds a triangular pattern of dimples in such cases, as shown by the dashed (red) line in Fig. 2.9 C. Understanding whether these mixed modes truly represent lower energy solutions or are the result of some underlying quenched disorder in the core/shell system is beyond the scope of our linear elasticity approach. Nevertheless, from our analysis it is easy to see that either small elastic nonlinearities or disorder may select such mixed modes from the space of degenerate states that we identify, and that these mixed mode solutions are qualitatively similar to those observed.

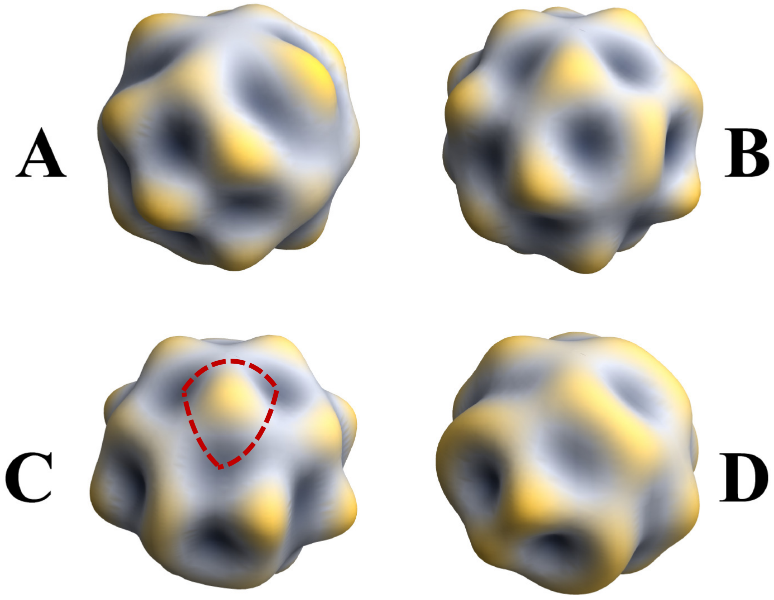

Figure 2.9: Examples systems with mixed degenerate states

Examples of mixing the degenerate buckling modes for a system with $\mu = 0.2$ and $\alpha = 300$. For this value of the control parameter, the degenerate modes are the $\ell = 8$ and $m \in [3, 8]$. Each example is an equally weighted mixture of buckling modes with amplitude such that $\Delta = 0.4$. **A**: $m = 4$ and 6; **B**: $m = 3$ and 7; **C**: $m = 3$ and 8; **D**: $m = 3,\ 5,\ 7,$ and 8.

2.4 Summary

We have demonstrated the analog of Euler buckling in spherical core-shell structures where the shell is treated as a tensionless lipid membrane, i.e., one whose elasticity is controlled solely by a bending modulus, κ. Such systems are found in gel-filled vesicles, but with some modifications to the treatment of the surface elasticity of the bounding membrane (e.g., adding an area compression modulus) these calculations have more general relevance to a variety of soft elastic solids coupled to thin shells, such any number of colloidal core/shell particles [118, 119, 127–129], or even the blastocyst that transitions from spherical to ovoid shape during embryonic development [130]. Following our exploration of a heuristic scalarized elasticity theory, we identified one control parameter for the transition upon increasing the bounding surface area between an isotropically expanded sphere and a buckled one. This control parameter $\alpha = \mu R^3/\kappa$ measures the relative compliance of the sphere's interior to its boundary. In the full elastic theory presented above, there is also a continuous and weak dependence of the results on the Poisson ratio of the elastic interior, but as long as the material remains somewhat compressible, these effects are subdominant.

It is of interest then to determine the expected magnitude of α for various systems of current interest. To do this it convenient to rewrite this dimensionless quantity as the ratio of two lengths: $\alpha = R^3/\xi^3$, where the numerator is of purely geometric origin – the size of the sphere – and the denominator $\xi = (\kappa/\mu)^{1/3}$ is a length set by the ratio of the surface to bulk moduli of the system. For many soft polymeric gels and even for the interior of eukaryotic cells the typical values of the shear modulus are in the range of 10^2–10^4Pa. Bending moduli of lipid bilayers are commonly found to be in the range of $10 - 100\ k_{\mathrm{B}}T$ at room temperature. This range of values generates a natural length scale of $\xi \sim 10^{-2}$–$10^{-1}\mu$m. Thus, for spheres of typical colloidal dimensions, $R \sim 1 - 10\mu m$, we find a range of $\alpha \sim 10^3 - 10^9$, justifying our focus on the large α regime. Since the optimally buckled state spherical harmonic $\ell^\star$ scales as $\alpha^{1/3}$, we predict that all buckled soft spheres of micron size will have $\ell^\star \sim \mathcal{O}(10)$. Such wrinkled states are indeed observed in the gel-filled vesicles [117]. We imagined that one encounters the mechanical instability leading to buckling via increasing the surface area of the bounding membrane at fixed interior volume. The gel-filled vesicle experiments generate the instability by reducing the interior at fixed membrane surface area. Within linear elasticity theory as used here, these two approaches to the instability are equivalent. There may be biophysical examples of the same mechanical instability driven by membrane growth occurring in cells, nuclei, and, more broadly, during development.

It should be possible to extend this analysis to consider the dynamics morphological change in growing systems. We identify in our present work the requisite excess area for the morphological transition. As long as stress relaxation is fast compared to growth, our analysis remains valid for any growth model: morphology is simply slaved to excess area. However, if one were to consider the interior to be viscoelastic with a sufficiently long stress relaxation time, then one should encounter interesting new dynamics of the instability by explicitly including material growth as explored in Refs. [107, 131].

A similar buckling transition has been analyzed for the geometry of a thin shell or membrane on a flat elastic substrate [132]. In that work, the authors describe a critical buckling stress as opposed to a critical excess surface area, as we do. The two are simply related in linear elasticity theory. We find that our results may be equivalently described in terms of a critical stress in the membrane for buckling. The key distinction between buckling on a sphere and on a flat substrate is that the sphere's radius now enters the critical stress. We may, in fact, express that critical stress in terms of the control parameter α and a dimensionless function of the Poisson ratio of the internal material. The result is given in Appendix 2.F.

Extending the above analysis to core-shell structures where the shell also contains a shear and area compression modulus remains an open and quite complex problem. We do expect the general phenomenology observed here to remain valid. Specifically, surface buckling will occur at a critical excess area and high moduli elastic interiors will push this morphological transition to lower critical fraction excess areas and require progressively lower symmetry buckled states for areas just above the critical value. We expect that the additional moduli associated with the surface will effectively stiffen the shell towards buckling and serve to further stabilize the isotropically extended sphere to larger values of Δ than those found here.

The theory presented here applies only for small distortions where linear elasticity remains valid. For the expected levels of fractional excess area $\Delta^\star \sim 0.5$ the typical size of the radial displacements at the surface are on the order of $u_r/R \sim 0.05$, so that it seems reasonable to suppose that the application of the theory is valid up to the predicted morphological transition. Clearly as more area is added beyond that point, nonlinear effects will become relevant. Numerical simulations [118] of elastic core-shell structures under "drying," where volume is removed from the interior rather than area added to the surface, have been performed. The results suggest that patterns reminiscent of those predicted here near the transition evolve under the further reduction of interior volume towards deeply folded surfaces where the folds meet in three-fold junctions that roughly tessellate the surface. This suggests that elastic nonlinearities neglected here lead to fold formation, as might be expected based on the extensive work on folding of two-dimensional globally elastic [104] and flat elastica coupled to elastic or viscous subspaces [116]. Exploring the folding phenomenon and the interactions of folds on a curved surface remains an open problem.

Appendix 2.A Mean curvature of the surface

The general curvature of the surface consist of the Gaussian curvature and the mean curvature. Since we consider only genus-preserving morphological transitions, we may neglect terms proportional to the Gaussian curvature modulus [133]. Therefore, only the mean curvature (H) is needed to compute the bending energy if the membrane. The mean curvature is defined as

$$H = \frac{\boldsymbol{\nabla} \cdot \hat{\mathbf{n}}}{2}, \tag{2.A.1}$$

where the form of $\hat{\mathbf{n}}$ is given by

$$\hat{\mathbf{n}} = \frac{\boldsymbol{\nabla}\mathcal{R}}{|\boldsymbol{\nabla}\mathcal{R}|} \tag{2.A.2}$$

$\mathcal{R}$ is the level of the surface, which has the form for:

$$\mathcal{R}(r,\theta,\phi) = 0 = r - R\left[1 + g(\Omega)\right]. \tag{2.A.3}$$

In the following calculations we will only keep terms up to $\mathcal{O}(g^2)$. Coordinate subscripts are used to indicate derivate with respect to the given coordinate, i.e. $g_\phi = \partial_\phi(g(\Omega))$. Using Eq. (2.2.17) as for the form of $r(\Omega)$ at the deformed surface and Eq. (2.A.2) we can write the unit normal vector as

$$\hat{\mathbf{n}} = \frac{\left[\hat{\mathbf{r}} - \frac{R}{r} g_\theta \hat{\theta} - \frac{R}{r\sin\theta} g_\phi \hat{\phi}\right]}{\left[1 + \left(\frac{R}{r} g_\theta\right)^2 + \left(\frac{R}{r\sin\theta} g_\phi\right)^2\right]^{\frac{1}{2}}}, \tag{2.A.4}$$

where r, θ, and ϕ are variables and R is the radius of the undeformed sphere.

Now we need to take the divergence of $\hat{\mathbf{n}}$. In spherical coordinates this has the form

$$\boldsymbol{\nabla} \cdot \hat{\mathbf{n}} = \frac{1}{r^2}\frac{\partial(r^2 \hat{\mathbf{n}} \cdot \hat{\mathbf{r}})}{\partial r} + \frac{1}{r\sin\theta}\frac{\partial(\sin\theta \; \hat{\mathbf{n}} \cdot \hat{\theta})}{\partial\theta} + \frac{1}{r\sin\theta}\frac{\partial(\hat{\mathbf{n}} \cdot \hat{\phi})}{\partial\phi}. \tag{2.A.5}$$

We evaluate Eq. (2.A.5) term-by-term and keep terms up to $\mathcal{O}(g^2)$. This first term is

$$\begin{aligned}
\frac{\partial(r^2\hat{\mathbf{n}}\cdot\hat{\mathbf{r}})}{\partial r} &= \frac{\partial}{\partial r}\left\{r^2\left[1+\left(\frac{R}{r}g_\theta\right)^2+\left(\frac{R}{r\sin\theta}g_\phi\right)^2\right]^{-\frac{1}{2}}\right\} \\
&= 2r\left[1+\left(\frac{R}{r}g_\theta\right)^2+\left(\frac{R}{r\sin\theta}g_\phi\right)^2\right]^{-\frac{1}{2}} \\
&+ r^2\left[1+\left(\frac{R}{r}g_\theta\right)^2+\left(\frac{R}{r\sin\theta}g_\phi\right)^2\right]^{-\frac{3}{2}}\left[\left(\frac{R^2}{r^3}g_\theta^2\right)+\left(\frac{R^2}{r^3\sin^2\theta}g_\phi^2\right)\right] \\
&\approx 2r-\left(\frac{R^2}{r}g_\theta^2\right)-\left(\frac{R^2}{r\sin^2\theta}g_\phi^2\right)+\left(\frac{R^2}{r}g_\theta^2\right)-\left(\frac{R^2}{r\sin^2\theta}g_\phi^2\right) \\
&\approx 2r \qquad (2.A.6)
\end{aligned}$$

The second term of Eq. (2.A.5) is

$$\begin{aligned}
\frac{\partial(\sin\theta\ \hat{\mathbf{n}}\cdot\hat{\theta})}{\partial\theta} &= \frac{\partial}{\partial\theta}\left\{-\sin\theta\left(\frac{R}{r}g_\theta\right)\left[1+\left(\frac{R}{r}g_\theta\right)^2+\left(\frac{R}{r\sin\theta}g_\phi\right)^2\right]^{-\frac{1}{2}}\right\} \\
&\approx \frac{\partial}{\partial\theta}\left\{-\sin\theta\left(\frac{R}{r}g_\theta\right)\left[1+\frac{1}{2}\left(\frac{R}{r}g_\theta\right)+\frac{1}{2}\left(\frac{R}{r\sin\theta}g_\phi\right)\right]\right\} \\
&\approx -\frac{R}{r}\frac{\partial\left(g_\theta\sin\theta\right)}{\partial\theta} \qquad (2.A.7)
\end{aligned}$$

The last term of Eq. (2.A.5) is

$$\begin{aligned}
\frac{\partial(\hat{\mathbf{n}}\cdot\hat{\phi})}{\partial\phi} &= \frac{\partial}{\partial\phi}\left\{\left(-\frac{R}{r\sin\theta}g_\phi\right)\left[1+\left(\frac{R}{r}g_\theta\right)^2+\left(\frac{R}{r\sin\theta}g_\phi\right)^2\right]^{-\frac{1}{2}}\right\} \\
&\approx \frac{\partial}{\partial\phi}\left\{\left(\frac{R}{r\sin\theta}g_\phi\right)\left[1+\frac{1}{2}\left(-\frac{R}{r}g_\theta\right)+\frac{1}{2}\left(\frac{R}{r\sin\theta}g_\phi\right)\right]\right\} \\
&\approx -\frac{R}{r\sin\theta}g_{\phi\phi} \qquad (2.A.8)
\end{aligned}$$

Combining Eqs. (2.A.6)–(2.A.8) we find that the divergent of the unit norm is

$$\boldsymbol{\nabla}\cdot\hat{\mathbf{n}} \approx \frac{2}{r}-\frac{R}{r^2\sin\theta}\frac{\partial\left(g_\theta\sin\theta\right)}{\partial\theta}-\frac{R}{r^2\sin^2\theta}g_{\phi\phi} \qquad (2.A.9)$$

It is worth noting that the square root in the denominator of Eq. (2.A.4) is significant. The expansion of this square would contain g_θ and g_ϕ to all orders, and therefore derivatives of all orders. Additional derivative break the degeneracy in the azimuthal mode as seen in Sec. 2.3.1.

Now we define the the following operator. This is the angular momentum operator for $\hat{L}^2$ that we are use to from quantum mechanics, but $\hbar$ replaced by $\frac{1}{2}$.

$$\hat{L}^2 = -\frac{1}{2}\left[\frac{1}{\sin\theta}\frac{\partial}{\partial\theta}\left(\sin\theta\frac{\partial}{\partial\theta}\right) + \frac{1}{\sin^2\theta}\frac{\partial^2}{\partial\phi^2}\right] \tag{2.A.10}$$

It will also be useful to define the ratio of the initial radius to both the varible r and the spontaneous radius R_s as follows:

$$\omega = \frac{R}{r} \tag{2.A.11}$$

$$\omega_s = \frac{R_s}{r} \tag{2.A.12}$$

Plugging in Eqs. (2.A.9)–(2.A.11) into Eq. (2.A.1) and noting that spontaneous curvature is $H_s = 1/R_s$, we obtain a convenient form for $H - H_s$.

$$H - H_s \approx \frac{1}{r}\left(1 + \omega\hat{L}^2 g\right) - \frac{1}{r_s}. \tag{2.A.13}$$

This form is useful because $\hat{L}^2$ acts of $g(\theta, \phi)$ in a very simple manner.

Appendix 2.B Metric of the surface

Now that we have $H - H_s$, we just need to calculate dS before we can compute bending energy of the membrane. To do this we need to find the metric of the surface and take it determine. The first step in computing the metric is to find the arc length.

$$\begin{aligned} d\ell^2 &= dr^2 + r^2 d\theta^2 + r^2\sin^2\theta d\phi^2 \\ &= (Rg_\theta d\theta + Rg_\phi d\phi)^2 + r^2 d\theta^2 + r^2\sin^2\theta d\phi^2 \\ &= R^2 g_\theta^2 d\theta^2 + 2R^2 g_\theta g_\phi d\theta d\phi + R^2 g_\phi^2 d\phi^2 + r^2 d\theta^2 + r^2\sin^2\theta d\phi^2 \\ &= (R^2 g_\theta^2 + r^2)d\theta^2 + 2(R^2 g_\theta g_\phi)d\theta d\phi + (R^2 g_\phi^2 + r^2\sin^2\theta)d\phi^2. \end{aligned} \tag{2.B.1}$$

Here we use Eq. (2.2.17) to compute dr and group terms with by powers of $d\theta$ and $d\phi$.

Equation (2.B.1) can also be rewritten into a matrix form:

$$d\ell^2 = \begin{bmatrix} d\theta \\ d\phi \end{bmatrix} \begin{bmatrix} E & F \\ F & G \end{bmatrix} \begin{bmatrix} d\theta & d\phi \end{bmatrix}, \tag{2.B.2}$$

where E, F, and G are of the form:

$$E = R^2 g_\theta^2 + r^2 \qquad F = R^2 g_\theta g_\phi \qquad G = R^2 g_\phi^2 + r^2 \sin^2\theta. \tag{2.B.3}$$

The center matrix in Eq. (2.B.2) is called the metric tensor and the metric is given by the square root of its determent:

$$\begin{aligned} dS &= \sqrt{EG - F^2}\, d\theta d\phi \\ &= \left[r^4 \sin^2\theta + R^2 r^2 g_\phi^2 + R^2 r^2 g_\theta^2 \sin^2\theta + R^4 g_\theta^2 g_\phi^2 - R^4 g_\theta^2 g_\phi^2\right]^{\frac{1}{2}} d\theta d\phi \\ &= \left[1 + \frac{R^2 g_\phi^2}{r^2 \sin^2\theta} + \frac{R^2 g_\theta^2}{r^2}\right]^{\frac{1}{2}} r^2 \sin\theta d\theta d\phi \\ &\approx \left[1 + \frac{1}{2}\left(\frac{R^2 g_\phi^2}{r^2 \sin^2\theta} + \frac{R^2 g_\theta^2}{r^2}\right)\right] r^2 \sin\theta d\theta d\phi \\ &\approx \left[1 + \frac{\omega^2}{2}\left(g_\theta^2 + \frac{g_\phi^2}{\sin^2\theta}\right)\right] r^2 d\Omega. \end{aligned} \tag{2.B.4}$$

The approximation in the fourth line of Eq. (2.B.4) is because we expanse the square root only out to second-order in g. It should be noted that if we recall the r is of the form given in Eq. (2.2.17), then Eq. (2.B.4) contains terms which are higher then second-order. We have retained these terms because when Eqs. (2.A.13) and (2.B.4) are combined to compute the Helfrich energy (Eq. (2.2.13)), there is some cancellation of the power of r.

Appendix 2.C Total Bending Energy

Plugging in Eq. (2.B.4) into Eq. (2.2.13), integral for the bending energy is of the form

$$\mathcal{E}^{bend} = \oint_{\mathcal{S}} (H - H_s)^2 \left[1 + \frac{\omega^2}{2}\left(g_\theta^2 + \frac{g_\phi^2}{\sin^2\theta}\right)\right] r^2 d\Omega, \tag{2.C.1}$$

where $\mathcal{S}$ denotes the surface of the deformed sphere.

To make this a more convenient to work with, we would rewrite the second term in this integral using integrating by parts. We replace $(H - H_s)^2$ by f for simplicity.

$$\begin{aligned}
&\oint \left(g_\theta^2 + \frac{g_\phi^2}{\sin^2\theta} \right) f(\theta, \phi) d\Omega \\
&= - \oint g \left[\frac{\partial}{\partial\theta} \left(f \sin\theta \frac{\partial g}{\partial\theta} \right) + \frac{1}{\sin\theta} \frac{\partial}{\partial\phi} \left(f \frac{\partial g}{\partial\phi} \right) \right] d\theta d\phi.
\end{aligned}$$

Note that we conduct the integration-by-parts by separation the first term in the two parts: g_θ and $g_\theta f \sin\theta d\theta$, we integrate the first part is differentiate the second. The same procedure is used on the second term. Because the integral is over a closed surface, the boundary term vanishes. The last last in the above equation also most has the form of $\hat{L}^2$. With this in mind we, rewrite it as following:

$$\begin{aligned}
&= \oint 2fg\hat{L}^2 g d\Omega - \oint g \left[f_\theta g_\theta + \frac{1}{\sin^2\theta} f_\phi g_\phi \right] d\Omega \\
&\approx \oint 2fg\hat{L}^2 g d\Omega. \qquad (2.C.2)
\end{aligned}$$

We drop the last term in the first line of Eq. (2.C.2) because the function f given by $(H - H_s)^2$. Thus both f_θ and f_ϕ are both proportional to g. This makes the second integral here at least 3^{rd} order in g. Our bending energy is now in a forms which is fairly easy to work with.

Substituting Eq. (2.C.2) into Eq. (2.C.1) yeilds

$$\begin{aligned}
\mathcal{E}^{bend} &\approx \frac{\kappa}{2} \oint \left[\frac{1}{r} \left(1 + \omega \hat{L}^2 g \right) - \frac{1}{r_s} \right]^2 \left[1 + \omega^2 \left(g \hat{L}^2 g \right) \right] r^2 d\Omega \\
&\approx \frac{\kappa}{2} \oint \left[\left(1 + \omega \hat{L}^2 g \right) - \frac{r}{r_s} \right]^2 \left[1 + \omega^2 \left(g \hat{L}^2 g \right) \right] d\Omega \\
&\approx \frac{\kappa}{2} \oint \left[\left(1 - \frac{r}{r_s} \right)^2 + 2\omega \left(1 - \frac{r}{r_s} \right) \hat{L}^2 g + \left(\omega \hat{L}^2 g \right)^2 \right] \left[1 + \omega^2 \left(g \hat{L}^2 g \right) \right] d\Omega. \qquad (2.C.3)
\end{aligned}$$

Here again we are only keeping terms up to second-order in g. We must keep in mind that r (Eq. (2.2.17)) and ω (Eq. (2.A.11)) are also functions of g. Now we expand both r and ω two second-order in g:

$$r = R(1 + g) \qquad (2.C.4a)$$

$$\omega = \frac{R}{r} = \frac{1}{1 + g} \approx 1 - g + g^2. \qquad (2.C.4b)$$

Plugging Eq. (2.C.4) back into this into Eq. (2.C.3) and dropping terms higher and second-order:

$$\begin{aligned}\mathcal{E}^{bend} &\approx \frac{\kappa}{2}\oint\left[\left(1-\frac{R(1+g)}{r_s}\right)^2+2(1-g+g^2)\left(1-\frac{R(1+g)}{r_s}\right)\hat{L}^2 g\right.\\ &\qquad\left.+(1-g+g^2)^2\left(\hat{L}^2 g\right)^2\right]\left[1+\left(g\hat{L}^2 g\right)\right]d\Omega\\ &\approx \frac{\kappa}{2}\oint\left[\left(1-\frac{R}{r_s}\right)^2-2\frac{R}{r_s}\left(1-\frac{R}{r_s}\right)g+\left(\frac{R}{r_s}\right)^2 g^2\right.\\ &\qquad\left.+2\left(2-\frac{R}{r_s}\right)\hat{L}^2 g-2g\hat{L}^2 g+\left(\hat{L}^2 g\right)^2\right]\left[1+\left(g\hat{L}^2 g\right)\right]d\Omega\end{aligned}$$

$$\begin{aligned}\mathcal{E}^{bend} &\approx \frac{\kappa}{2}\oint\left[\left(1-\frac{R}{r_s}\right)^2+2\left(2\hat{L}^2-\frac{R}{r_s}\hat{L}^2-\frac{R}{r_s}+\frac{R^2}{r_s^2}\right)g+\left(\frac{R}{r_s}\right)^2 g^2\right.\\ &\qquad\left.-\left(1+\frac{2R}{r_s}-\frac{R^2}{r_s^2}\right)g\hat{L}^2 g+\left(\hat{L}^2 g\right)^2\right]d\Omega\end{aligned}$$

$$\begin{aligned}&\approx \frac{\kappa}{2}\oint\left(1-\omega_s\right)^2 d\Omega\\ &+\frac{\kappa}{2}\oint\left\{\omega_s^2\left[2g+g^2+g\hat{L}^2 g\right]-\omega_s\left[2g+\hat{L}^2 g+2g\hat{L}^2 g\right]\right.\\ &\qquad\left.+\left[4\hat{L}^2 g-g\hat{L}^2 g+\left(\hat{L}^2 g\right)^2\right]\right\}d\Omega\end{aligned} \tag{2.C.5}$$

The first term in Eq. (2.C.5) is the energy associated with the radius of the initial sphere being different the spontaneous radius of curvature and is independent of displacement of the surface. The second integral, $\Delta\mathcal{E}$ contains all of the terms which contain the surface displacement. To proceed farther we need to plug in for g.

$$
\begin{aligned}
\Delta\mathcal{E} = \frac{\kappa}{2}\sum_{\ell,m\geq 0}\oint\Bigg\{&\omega_s^2\left[2\left(g_{\ell m}Y_{\ell m}\right)+\left(g_{\ell m}Y_{\ell m}\right)\left(g_{\ell m}Y_{\ell m}\right)+\left(g_{\ell m}Y_{\ell m}\right)\hat{L}^2\left(g_{\ell m}Y_{\ell m}\right)\right]\\
&-\omega_s\left[2\left(g_{\ell m}Y_{\ell m}\right)+\hat{L}^2\left(g_{\ell m}Y_{\ell m}\right)+2\left(g_{\ell m}Y_{\ell m}\right)\hat{L}^2\left(g_{\ell m}Y_{\ell m}\right)\right]\\
&+\left[4\hat{L}^2\left(g_{\ell m}Y_{\ell m}\right)-\left(g_{\ell m}Y_{\ell m}\right)\hat{L}^2\left(g_{\ell m}Y_{\ell m}\right)+\hat{L}^2\left(g_{\ell m}Y_{\ell m}\right)\hat{L}^2\left(g_{\ell m}Y_{\ell m}\right)\right]\Bigg\}d\Omega
\end{aligned}
\tag{2.C.6}
$$

In Eq. (2.C.6) factors of g^2 generates cross terms, $Y_{\ell m}Y_{\ell'}^{m'}$, but because spherical harmonics are orthogonal functions and how we constructed $Y_{\ell m}$ (Eq. (2.2.18)) they vanish unless $m' = m$. Additionally we know that when $\hat{L}^2$ acts on $Y_{\ell m}$ it it just produces $\frac{\ell(\ell+1)}{2}$, we can see that there are only two different integrals we need to compute:

$$
\oint d\Omega\ g_{\ell m}Y_{\ell m}
$$

$$
\oint d\Omega\left(g_{\ell m}Y_{\ell m}\right)\left(g_{\ell m}Y_{\ell m}\right)
$$

The first integral gives fair simple result of

$$
\begin{aligned}
\oint d\Omega\ g_{\ell m}Y_{\ell m} &= \oint d\Omega\ g_{\ell m}Y_{\ell m}\left(\sqrt{4\pi}Y_0^0\right)\\
&= g_0\sqrt{4\pi}.
\end{aligned}
\tag{2.C.7}
$$

Looking at the second integral we find

$$
\oint d\Omega\left(g_{\ell m}Y_{\ell m}\right)\left(g_{\ell m}Y_{\ell m}\right) = |g_{\ell m}|^2 \tag{2.C.8}
$$

We arrive at Eq. (2.C.8) because we constructed $Y_{\ell m}$ to be real-valued (see Eq. (2.2.18)). Plugging this back into Eq. (2.C.6) we arrive at form of the $\Delta\mathcal{E}$.

$$
\begin{aligned}
\Delta\mathcal{E} &= g_0\kappa\sqrt{4\pi}\left(\omega_s^2-\omega_s\right)\\
&\quad+\frac{\kappa}{2}\sum_{\ell,m\geq 0}\omega_s^2\left[|g_{\ell m}|^2+\frac{\ell(\ell+1)}{2}|g_{\ell m}|^2\right]-\omega_s\left[\ell(\ell+1)|g_{\ell m}|^2\right]\\
&\qquad+\left[\left(\frac{\ell(\ell+1)}{2}\right)^2|g_{\ell m}|^2-\frac{\ell(\ell+1)}{2}|g_{\ell m}|^2\right]\\
&= 2\pi\kappa\bar{g}_0\omega_s\left[\omega_s(2+\bar{g}_0)-2\right]\\
&\quad+\frac{\kappa}{8}\sum_{\ell\neq 0,m\geq 0}|g_{\ell m}|^2\left[(\ell+2)(\ell+1)(\ell)(\ell-1)-4\omega_s\ell(\ell+1)+\omega_s^2(4+2\ell(\ell+1))\right]
\end{aligned}
\tag{2.C.9}
$$

Here we define $\bar{g}_0 \equiv g_0/\sqrt{4\pi}$.

Recall that $\Delta\mathcal{E}$ was the second term in Eq. (2.C.5). The total bending energy is obtain by including adding the back in the first term of Eq. (2.C.5).

$$\begin{aligned}\mathcal{E}^{bend} &= 2\pi\kappa\left(1-\omega_s\right)^2 + 2\pi\kappa\bar{g}_0\omega_s\left[\omega_s(2+\bar{g}_0)-2\right] \\ &+ \frac{\kappa}{8}\sum_{\ell\neq 0, m\geq 0}|g_{\ell m}|^2\Big[(\ell+2)(\ell+1)(\ell)(\ell-1) - 4\omega_s\ell(\ell+1) + \omega_s^2(4+2\ell(\ell+1))\Big]\end{aligned} \tag{2.C.10}$$

Appendix 2.D Solving for the elastic deformation of the sphere's interior

In this appendix we examine in more detail the solution to elasticity problem proposed in the text. Namely, if one were to specify a radial displacement of the surface of an elastic sphere in terms of a single spherical harmonic, what is the form of the displacement field in the sphere's interior? We solved this problem by asserting that one may find a harmonic vector field $\mathbf{S}_{\ell m}$ that satisfies the required radial displacements on the sphere's surface. In this appendix we present some of the details of that computation and give the solution of the displacement field $\mathbf{u}(\mathbf{x})$.

2.D.1 Force Balance

At every point in the sphere must be in force balance. Because there are no body forces involved $\boldsymbol{\nabla}\cdot\overleftrightarrow{\sigma} = 0$. Writing this equation in components and using the stress-strain relation yields an equation for the displacement field inside the sphere.

Stress-Strain Relation $$\sigma_{ik} = B\delta_{ik}u_{\ell\ell} + 2\mu\left(u_{ik} - \frac{1}{3}\delta_{ik}u_{\ell\ell}\right) \tag{2.D.1}$$

Linearized Strain Tensor $$u_{ik} = \frac{1}{2}\left(\partial_i u_k + \partial_k u_i\right) \tag{2.D.2}$$

Enforcing equilibrium gives

$$\begin{aligned} 0 &= \partial_k \sigma_{ik} \\ &= B\ \partial_k \partial_\ell u_\ell \delta_{ik} + 2\mu \left[\partial_k \left(\frac{\partial_i u_k + \partial_k u_i}{2} \right) - \frac{1}{3} \partial_k \partial_\ell \delta_{ik} u_{\ell\ell} \right] \\ &= (\lambda + \mu)\, \boldsymbol{\nabla} \left(\boldsymbol{\nabla} \cdot \mathbf{u} \right) + \mu \nabla^2 \mathbf{u}. \end{aligned} \tag{2.D.3}$$

Now we can take the divergence of the Eq. (2.D.3) and notice $0 = \nabla^2 \left(\boldsymbol{\nabla} \cdot \mathbf{u} \right)$, therefore $(\boldsymbol{\nabla} \cdot \mathbf{u})$ is a harmonic function. As a harmonic function we can expand it as a sum of solid spherical harmonics:

$$\boldsymbol{\nabla} \cdot \mathbf{u} = f(r, \theta, \phi) = \sum_{\ell=0}^{\infty} \sum_{m=-\ell}^{\ell} f_\ell^m r^\ell Y_\ell^m. \tag{2.D.4}$$

We next take the curl of the Eq. (2.D.3) and notice that $0 = \nabla^2 \left(\boldsymbol{\nabla} \times \mathbf{u} \right)$. Therefore, $(\boldsymbol{\nabla} \times \mathbf{u})$ is also are harmonic function. The problem that arises here is that we do not have the solution to the harmonic vector equation in spherical coordinates, so at this point we take guidance from Love [134] and change to Cartesian coordinates. Looking at the ith component of the equilibrium equation we have:

$$(\lambda + \mu)\, \partial_i f(r, \theta, \phi) + \mu \nabla^2 u_i = 0, \quad i \in \{x, y, z\}. \tag{2.D.5}$$

Where we have replaced the divergence of $\mathbf{u}$ using Eq. (2.D.4).

To solve Eq. (2.D.5) we write the Cartesian derivatives of the f. Below we state these derivatives in terms of r, θ and ϕ

$$\partial_x = \sin\theta\ \cos\phi\ \partial_r + \frac{\cos\theta\ \cos\phi\ \partial_\theta}{r} - \frac{\sin\phi}{r \sin\theta} \partial_\phi \tag{2.D.6a}$$

$$\partial_y = \sin\theta\ \sin\phi\ \partial_r + \frac{\cos\theta\ \sin\phi\ \partial_\theta}{r} + \frac{\cos\phi}{r \sin\theta} \partial_\phi \tag{2.D.6b}$$

$$\partial_z = \cos\theta\ \partial_r - \frac{\sin\theta}{r}. \tag{2.D.6c}$$

2.D.2 Properties of Derivatives of Harmonic Functions

Derivatives of spherical harmonics are messy to compute, so we will avoided explicitly computing them. For now we will just cover general properties of these derivatives.

Let $\mathcal{F}$ be a harmonic function (e.g.: Y_ℓ^m). Because derivatives commute with the Laplacian, derivatives of $\mathcal{F}$ are also harmonic functions

$$\begin{gathered} 0 = \partial_i \left[\nabla^2 \mathcal{F}(r,\theta,\phi)\right] = \nabla^2 \left[\partial_i \mathcal{F}(r,\theta,\phi)\right] \\ \partial_i \mathcal{F}(r,\theta,\phi) \text{ is a harmonic function.} \end{gathered} \tag{2.D.7}$$

Given that derivatives of $\mathcal{F}$ are also harmonic functions, we know that they can be expressed at a sum of solid spherical harmonics.

The next thing to notice is that a derivative of a solid spherical harmonic of order ℓ (i.e. $r^\ell Y_\ell^m$) produces a sum of solid spherical harmonics of order $\ell - 1$. To show this we first focus on the r-dependence. When ∂_i acts on $\mathcal{F}$ it produces a sum of terms, each of which are proportional to $r^{\ell-1}$. The power of r is reduced by 1 (from r^ℓ to $r^{\ell-1}$) by taking a derivative:

$$\partial_i \left(r^\ell Y_\ell^m\right) \propto r^{\ell-1} \tag{2.D.8}$$

$$\partial_i \left(r^\ell Y_\ell^m\right) = r^{\ell-1} \mathcal{G}(\theta,\phi;i). \tag{2.D.9}$$

Equation (2.D.7) shows that $\partial_i \left(r^\ell Y_{\ell m}\right)$ is a harmonic function. Therefore $r^{\ell-1}\mathcal{G}(\theta,\phi;i)$ is also a harmonic function. This is only true if $\mathcal{G}(\theta,\phi;i)$ consist only of spherical harmonics of order $\ell - 1$. All together we have Eq. (2.D.10) where $g_{\ell-1}^{m'}(i)$ are unknown coefficients.

At this point we could calculate these coefficients, but instead we will simply leave them as unknowns for now. The important part is that we know the order of these spherical harmonics. Knowing the order of the spherical harmonics allows us to takes its Laplacian without know the coefficients:

$$\partial_i \left(r^\ell Y_\ell^m\right) = \sum_{m'=-(\ell-1)}^{\ell-1} r^{\ell-1} Y_{\ell-1}^{m'} \; g_{\ell-1}^{m'}(i). \tag{2.D.10}$$

2.D.3 Laplacian of Displacement Field

Plugging Eq. (2.D.4) into Eq. (2.D.3) gives

$$\nabla^2 u_i = -\left(\frac{\lambda + \mu}{\mu}\right) \partial_i f(r,\theta,\phi). \tag{2.D.11}$$

We will now try to construct a solution to this equation. We know that the Laplacian operator the has units of inverse length square and that spherical harmonics are eigenfunctions of the Laplacian. Thus we take the following as our initial guess for the solution to Eq. (2.D.11):

$$\text{Initial Ansatz:}\quad u_i(r,\theta,\phi) = \alpha[r^2\ \partial_i f(r,\theta,\phi)], \tag{2.D.12}$$

where α is an unknown constant.

Now we take the Laplacian of our ansatz to see if we reproduce the right-hand side of Eq. (2.D.11):

$$\nabla^2\alpha\left[r^2\ \partial_i f(r,\theta,\phi)\ \right] = \sum_{\ell=0}^{\infty}\sum_{m=-\ell}^{\ell} f_\ell^m \nabla^2\left[r^2\ \partial_i\left(r^\ell Y_\ell^m\right)\right]$$

$$\begin{aligned}
\sum_{\ell=0}^{\infty}\sum_{m=-\ell}^{\ell} f_\ell^m \nabla^2\left[r^2\ \partial_i\left(r^\ell Y_\ell^m\right)\right] &= \sum_{\ell=0}^{\infty}\sum_{m=-\ell}^{\ell} f_\ell^m \alpha\left[\sum_{m'=-(\ell-1)}^{\ell-1} g_{\ell-1}^{m'}(i)\ \nabla^2\left(r^{\ell+1}Y_{\ell-1}^{m'}\right)\right]\\
&= \sum_{\ell=0}^{\infty}\sum_{m=-\ell}^{\ell} f_\ell^m \alpha\left[\sum_{m'=-(\ell-1)}^{\ell-1} g_{\ell-1}^{m'}(i)\ \left(2(2\ell+1)r^{\ell-1}Y_{\ell-1}^{m'}\right)\right]\\
&= \sum_{\ell=0}^{\infty}\sum_{m=-\ell}^{\ell} 2(2\ell+1) f_\ell^m \alpha\left[\sum_{m'=-(\ell-1)}^{\ell-1} g_{\ell-1}^{m'}(i)\ \left(r^{\ell-1}Y_{\ell-1}^{m'}\right)\right]\\
&= \sum_{\ell=0}^{\infty}\sum_{m=-\ell}^{\ell} 2(2\ell+1) f_\ell^m \alpha\left[r^2\ \partial_i\left(r^\ell Y_\ell^m\right)\right].
\end{aligned} \tag{2.D.13}$$

Our initial ansatz didn't quite yield a function which proportional to the right-hand side of Eq. (2.D.11). In Eq. (2.D.13) each term on the right-hand side differs by a factor of $2(2\ell+2)$. We dividing the factor out in our next ansatz for u_i:

$$\text{Old Ansatz:}\qquad u_i(r,\theta,\phi) = \alpha[r^2\ \partial_i f(r,\theta,\phi)]\ = \sum_{\ell=0}^{\infty}\sum_{m=-\ell}^{\ell} f_\ell^m\left[r^2\ \partial_i\left(r^\ell Y_\ell^m\right)\right]$$

$$\text{New Ansatz:}\qquad u_i(r,\theta,\phi) = \alpha\sum_{\ell=0}^{\infty}\sum_{m=-\ell}^{\ell}\frac{f_\ell^m}{2(2\ell+1)}\left[r^2\ \partial_i\left(r^\ell Y_\ell^m\right)\right]. \tag{2.D.14}$$

Taking the Laplacian of the new ansatz we see

$$\begin{aligned}
\nabla^2 u_i &= \alpha\sum_{\ell=0}^{\infty}\sum_{m=-\ell}^{\ell}\frac{f_\ell^m}{2(2\ell+1)}\nabla^2\left[r^2\ \partial_i\left(r^\ell Y_\ell^m\right)\right]\\
&= \alpha\sum_{\ell=0}^{\infty}\sum_{m=-\ell}^{\ell} f_\ell^m\left[r^2\ \partial_i\left(r^\ell Y_\ell^m\right)\right]\\
&= \alpha\partial_i f(r,\theta,\phi).
\end{aligned}$$

Comparing this with Eq. (2.D.11) gives $\alpha = \frac{-(\lambda+\mu)}{\mu}$. Now we have the particular solution to Eq. (2.D.11), however to obtain a general solution, the homogeneous solution must also be considered. To obtain the full solution for u_i a homogeneous term must be added to this:

$$u_i^p(r,\theta,\phi) = -\frac{\lambda+\mu}{\mu}\sum_{\ell=0}^{\infty}\sum_{m=-\ell}^{\ell}\frac{f_\ell^m}{2(2\ell+1)}\left[r^2\,\partial_i\left(r^\ell Y_\ell^m\right)\right] \tag{2.D.15}$$

$$u_i^h(r,\theta,\phi) = \sum_{\ell=0}^{\infty}\sum_{m=-\ell}^{\ell} h_{i,\ell}^m r^\ell Y_\ell^m \tag{2.D.16}$$

$$u_i(r,\theta,\phi) = u_i^p + u_i^h = -\frac{\lambda+\mu}{\mu}\sum_{\ell=0}^{\infty}\sum_{m=-\ell}^{\ell}\left[\frac{r^2 f_\ell^m}{2(2\ell+1)}\partial_i\left(r^\ell Y_\ell^m\right) - \frac{\mu}{\lambda+\mu}h_{i,\ell}^m r^\ell Y_\ell^m\right] \tag{2.D.17}$$

$$\mathbf{u} = -\frac{\lambda+\mu}{\mu}\sum_{\ell=0}^{\infty}\sum_{m=-\ell}^{\ell}\left[\frac{r^2 f_\ell^m}{2(2\ell+1)}\boldsymbol{\nabla}\left(r^\ell Y_\ell^m\right) - \frac{\mu}{\lambda+\mu}\mathbf{h}_\ell^m r^\ell Y_\ell^m\right]. \tag{2.D.18}$$

In Eq. (2.D.16) $h_{i,\ell}^m$ is the ith component of vector of constant coefficients. This vector is unknown at this point. It will be used to satisfy boundary conditions

2.D.4 Constraining $\boldsymbol{\nabla}\cdot\mathbf{u}$

Noted that **u** is written as a Cartesian vector. This vector satisfies Eq. (2.D.3) by construction, but there is a we have an additional consistency condition. In Eq. (2.D.4) we set $(\boldsymbol{\nabla}\cdot\mathbf{u})$ equal to the harmonic function $f(r,\theta,\phi)$. This equality must hold for our solution of **u** in Eq. (2.D.18)

$$\begin{aligned} f(r,\theta,\phi) &= \boldsymbol{\nabla}\cdot\mathbf{u} \\ &= -\frac{\lambda+\mu}{\mu}\sum_{\ell=0}^{\infty}\sum_{m=-\ell}^{\ell}\boldsymbol{\nabla}\cdot\left[\frac{r^2 f_\ell^m}{2(2\ell+1)}\boldsymbol{\nabla}\left(r^\ell Y_\ell^m\right) - \frac{\mu}{\lambda+\mu}\mathbf{h}_\ell^m r^\ell Y_\ell^m\right] \\ &= -\frac{\lambda+\mu}{\mu}\sum_{\ell=0}^{\infty}\sum_{m=-\ell}^{\ell}\left[\frac{f_\ell^m}{2(2\ell+1)}\boldsymbol{\nabla}\cdot\left\{r^2\boldsymbol{\nabla}\left(r^\ell Y_\ell^m\right)\right\} - \frac{\mu}{\lambda+\mu}\mathbf{h}_\ell^m\cdot\boldsymbol{\nabla}\left(r^\ell Y_\ell^m\right)\right]. \end{aligned} \tag{2.D.19}$$

The first term in the square brackets reduces to a simple expression because of the spherical harmonic.

$$\begin{aligned}\boldsymbol{\nabla}\cdot\left\{r^2\boldsymbol{\nabla}\left(r^\ell Y_\ell^m\right)\right\} &= \boldsymbol{\nabla}r^2\cdot\boldsymbol{\nabla}\left(r^\ell Y_\ell^m\right)+\overbrace{r^2\nabla^2\left(r^\ell Y_\ell^m\right)}^{\text{equals zero}}\\ &= 2r\hat{\mathbf{r}}\cdot\partial_r\left(r^\ell Y_\ell^m\right)\hat{\mathbf{r}}\\ &= 2\ell\left(r^\ell Y_\ell^m\right) \qquad (2.D.20)\end{aligned}$$

Now we can go back to Eq. (2.D.19) and replace the first term in the square brackets with Eq. (2.D.20) to yield:

$$\begin{aligned}f(r,\theta,\phi) &= \sum_{\ell=0}^{\infty}\sum_{m=-\ell}^{\ell} f_\ell^m r^\ell Y_\ell^m = \boldsymbol{\nabla}\cdot\mathbf{u}\\ &= -\frac{\lambda+\mu}{\mu}\sum_{\ell=0}^{\infty}\sum_{m=-\ell}^{\ell}\left[\frac{f_\ell^m}{2(2\ell+1)}\left\{2\ell\left(r^\ell Y_\ell^m\right)\right\}-\frac{\mu}{\lambda+\mu}\mathbf{h}_\ell^m\cdot\boldsymbol{\nabla}\left(r^\ell Y_\ell^m\right)\right]\\ &= -\frac{\lambda+\mu}{\mu}\sum_{\ell=0}^{\infty}\sum_{m=-\ell}^{\ell}\frac{\ell\ f_\ell^m}{(2\ell+1)}\left(r^\ell Y_\ell^m\right)+\sum_{\ell=0}^{\infty}\left[\sum_{m=-\ell}^{\ell}\mathbf{h}_\ell^m\cdot\boldsymbol{\nabla}\left(r^\ell Y_\ell^m\right)\right]. \qquad (2.D.21)\end{aligned}$$

The second term in the square brackets takes a bit more work. As discussed in the Appendix 2.D.2, the derivative of a solid spherical harmonic of order ℓ is a sum of solid spherical harmonics of order $\ell-1$. Knowing this we define a new function Ψ_ℓ in Eq. (2.D.22). Ψ_ℓ is define in such a manner that it consist only of solid spherical harmonics of order ℓ.

$$\Psi_\ell \equiv \sum_{m=-(\ell+1)}^{\ell+1}\mathbf{h}_{\ell+1}^m\cdot\boldsymbol{\nabla}\left(r^{\ell+1}Y_{\ell+1}^m\right). \qquad (2.D.22)$$

Note that Ψ_ℓ contains spherical harmonics of order $\ell+1$. Additional we define a few more functions which will prove useful

$$\Psi_\ell = \sum_{m=-\ell}^{\ell}\psi_\ell^m \qquad (2.D.23a)$$

$$\psi_\ell^m = p_\ell^m r^\ell Y_\ell^m \qquad (2.D.23b)$$

$$p_\ell^m = \oint\partial\Omega\ \frac{\Psi_\ell}{r^\ell}Y_\ell^m. \qquad (2.D.23c)$$

Combining Eqs. (2.D.22) and (2.D.23) gives the following relations:

$$\sum_{m'=-\ell}^{\ell} \mathbf{h}_\ell^{m'} \cdot \boldsymbol{\nabla}\left(r^\ell Y_\ell^{m'}\right) = \sum_{m=-(\ell-1)}^{\ell-1} \psi_{\ell-1}^m \tag{2.D.24a}$$

$$0 = \psi_{-1}^m = \Psi_{-1}. \tag{2.D.24b}$$

Substituting Eq. (2.D.23b) and Eq. (2.D.24a) into Eq. (2.D.21) results in Eq. (2.D.26). Remember that Y_0^0 is a constant and its gradient is zero. This means that $p_{-1}^m = 0\ \forall m$. This allows us to re-index the sum going from Eq. (2.D.25) to Eq. (2.D.26) while starting from the same value.

$$\begin{aligned}
&\sum_{\ell=0}^{\infty}\sum_{m=-\ell}^{\ell} f_\ell^m r^\ell Y_\ell^m \\
&\quad= -\frac{\lambda+\mu}{\mu}\sum_{\ell=0}^{\infty}\sum_{m=-\ell}^{\ell}\frac{\ell\ f_\ell^m}{(2\ell+1)}\left(r^\ell Y_\ell^m\right) + \sum_{\ell=0}^{\infty}\left[\sum_{m=-(\ell-1)}^{\ell-1} p_{\ell-1}^m r^{\ell-1} Y_{\ell-1}^m\right] \\
&\quad= -\frac{\lambda+\mu}{\mu}\sum_{\ell=0}^{\infty}\sum_{m=-\ell}^{\ell}\frac{\ell\ f_\ell^m}{(2\ell+1)}\left(r^\ell Y_\ell^m\right) + \sum_{\ell=-1}^{\infty}\left[\sum_{m=-\ell}^{\ell} p_\ell^m r^\ell Y_\ell^m\right] && \text{(2.D.25)} \\
&\quad= -\frac{\lambda+\mu}{\mu}\sum_{\ell=0}^{\infty}\sum_{m=-\ell}^{\ell}\left[\frac{\ell\ f_\ell^m}{(2\ell+1)} r^\ell Y_\ell^m - \frac{\mu\ p_\ell^m}{\lambda+\mu} r^\ell Y_\ell^m\right] && \text{(2.D.26)}
\end{aligned}$$

Because solid spherical harmonics from a basis for $\mathbb{R}^3$, Eq. (2.D.26) must hold term by term. This gives a relation between p_ℓ^m and f_ℓ^m.

$$\begin{aligned}
f_\ell^m r^\ell Y_\ell^m &= -\frac{\lambda+\mu}{\mu}\frac{\ell\ f_\ell^m}{(2\ell+1)} r^\ell Y_\ell^m + p_\ell^m r^\ell Y_\ell^m \\
f_\ell^m\left(1 + \frac{\lambda+\mu}{\mu}\frac{\ell}{(2\ell+1)}\right) &= p_\ell^m \\
f_\ell^m\left(\frac{(\lambda+\mu)\ell + \mu(2\ell+1)}{\mu(2\ell+1)}\right) &= p_\ell^m \\
f_\ell^m\left(\frac{\lambda\ell + \mu(3\ell+1)}{\mu(2\ell+1)}\right) &= p_\ell^m \\
f_\ell^m &= \left(\frac{\mu(2\ell+1)}{\lambda\ell + \mu(3\ell+1)}\right) p_\ell^m && \text{(2.D.27)}
\end{aligned}$$

The coefficients in the expansion of divergence of $\mathbf{u}$ are related to the coefficients in the expansion of ψ_ℓ^m by Eq. (2.D.27). One thing that can be seen right away is that if $\boldsymbol{\nabla}\cdot\mathbf{u} = 0$ then either all $p_\ell^m = 0$ or $\lambda = \infty$.

2.D.5 General Solution before Boundaries Conditions in Cartesian Coordinates

Now we can write down a general solution for the displacement

$$\begin{aligned}
\mathbf{u} &= -\frac{\lambda+\mu}{\mu}\sum_{\ell=0}^{\infty}\sum_{m=-\ell}^{\ell}\left[\frac{r^2}{2(2\ell+1)}\left(\frac{\mu(2\ell+1)}{\lambda\ell+\mu(3\ell+1)}\right)p_\ell^m\boldsymbol{\nabla}\left(r^\ell Y_\ell^m\right)-\frac{\mu}{\lambda+\mu}\mathbf{h}_\ell^m r^\ell Y_\ell^m\right] \\
&= -\frac{\lambda+\mu}{\mu}\sum_{\ell=0}^{\infty}\sum_{m=-\ell}^{\ell}\left[\frac{1}{2}\left(\frac{\mu r^2}{\lambda\ell+\mu(3\ell+1)}\right)\boldsymbol{\nabla}\left(p_\ell^m r^\ell Y_\ell^m\right)-\frac{\mu}{\lambda+\mu}\mathbf{h}_\ell^m r^\ell Y_\ell^m\right] \\
&= \sum_{\ell=0}^{\infty}\sum_{m=-\ell}^{\ell}\left[\frac{-1}{2}\left(\frac{(\lambda+\mu)r^2}{\lambda\ell+\mu(3\ell+1)}\right)\boldsymbol{\nabla}\left(p_\ell^m r^\ell Y_\ell^m\right)+\mathbf{h}_\ell^m r^\ell Y_\ell^m\right] \\
&= \sum_{\ell=0}^{\infty}\sum_{m=-\ell}^{\ell}\left[-M_\ell r^2\boldsymbol{\nabla}\psi_\ell^m+\mathbf{h}_\ell^m r^\ell Y_\ell^m\right], \quad M_\ell=\frac{1}{2}\left(\frac{\lambda+\mu}{\lambda\ell+\mu(3\ell+1)}\right). \qquad (2.D.28)
\end{aligned}$$

Rewriting this in vector notation we have

$$\mathbf{u}(r,\theta,\phi)=\sum_{\ell=0}^{\infty}\sum_{m=-\ell}^{\ell}\left[-M_\ell r^2\boldsymbol{\nabla}\psi_\ell^m+\mathbf{h}_\ell^m r^\ell Y_\ell^m\right] \qquad (2.D.29a)$$

$$M_\ell=\frac{1}{2}\left(\frac{\lambda+\mu}{\lambda\ell+\mu(3\ell+1)}\right) \qquad (2.D.29b)$$

$$\sum_{m=-(\ell+1)}^{(\ell+1)}\mathbf{h}_{(\ell+1)}^m\cdot\boldsymbol{\nabla}\left(r^{(\ell+1)}Y_{(\ell+1)}^m\right)=\sum_{m'=-\ell}^{\ell}\psi_\ell^{m'}. \qquad (2.D.29c)$$

We now have the general solution for an elastic spherical which is only under the influence surfaces forces. All that remains is to enforce boundary conditions. To do this we will need to solve for the unknown vector $\mathbf{h}_\ell^m$.

2.D.6 Spherical Boundary Conditions

Our boundary conditions are given by the displacement field at the surface of the sphere ($r=R$). They are expressed as a sum over spherical harmonics:

$$\begin{aligned}
\mathbf{u}(r,\theta,\phi)|_{r=R}=\mathbf{S}(\theta,\phi) &= \sum_{\ell=0}^{\infty}\sum_{m=-\ell}^{\ell}\mathbf{s}_\ell^m Y_\ell^m \\
&= \sum_{\ell=0}^{\infty}\sum_{m=-\ell}^{\ell}\left(s_{x,\ell}^m\hat{\mathbf{x}}+s_{y,\ell}^m\hat{\mathbf{y}}+s_{z,\ell}^m\hat{\mathbf{z}}\right)Y_\ell^m.
\end{aligned} \qquad (2.D.30)$$

This boundary condition must match Eq. (2.D.29a) at the surface of the sphere. Again because solid spherical harmonics are orthogonal functions we can equate Eq. (2.D.30) to the

Eq. (2.D.29a) at the boundary term by term:

$$\begin{aligned}\left(\frac{r^\ell}{R^\ell}\right) s^m_{x,\ell} Y^m_\ell &= -M_\ell R^2 \frac{d\psi^m_\ell}{dx} + h^m_{x,\ell} r^\ell Y^m_\ell \\ \left(\frac{r^\ell}{R^\ell}\right) s^m_{y,\ell} Y^m_\ell &= -M_\ell R^2 \frac{d\psi^m_\ell}{dy} + h^m_{y,\ell} r^\ell Y^m_\ell \\ \left(\frac{r^\ell}{R^\ell}\right) s^m_{z,\ell} Y^m_\ell &= -M_\ell R^2 \frac{d\psi^m_\ell}{dz} + h^m_{z,\ell} r^\ell Y^m_\ell .\end{aligned} \tag{2.D.31}$$

At the surface the factor on the left-hand side in parentheses is equal to 1. This is just the statement that the displacement field is equal to the boundary conditions at the surface. For this to hold both sides must have the same θ & ϕ-dependences. The factor in the parentheses is added to give both sides the same r- dependences. This ensures that both sides are equal everywhere.

Our next goal is to remove the **h**-dependences from Eq. (2.D.29a). To proceed it is best to rewrite the boundaries conditions by solving for the terms which contain **h**, multiplying each equation by its corresponding unit vector:

$$h^m_{x,\ell} r^\ell Y^m_\ell \hat{\mathbf{x}} = \left(\frac{r^\ell}{R^\ell}\right) s^m_{x,\ell} Y^m_\ell \hat{\mathbf{x}} + M_\ell R^2 \frac{d\psi^m_\ell}{dx} \hat{\mathbf{x}} \tag{2.D.32a}$$

$$h^m_{y,\ell} r^\ell Y^m_\ell \hat{\mathbf{y}} = \left(\frac{r^\ell}{R^\ell}\right) s^m_{y,\ell} Y^m_\ell \hat{\mathbf{y}} + M_\ell R^2 \frac{d\psi^m_\ell}{dy} \hat{\mathbf{y}} \tag{2.D.32b}$$

$$h^m_{z,\ell} r^\ell Y^m_\ell \hat{\mathbf{z}} = \left(\frac{r^\ell}{R^\ell}\right) s_{z,\ell} Y^m_\ell \hat{\mathbf{z}} + M_\ell R^2 \frac{d\psi^m_\ell}{dz} \hat{\mathbf{z}} \tag{2.D.32c}$$

$$\mathbf{h}^m_\ell r^\ell Y^m_\ell = \left(\frac{r^\ell}{R^\ell}\right) \mathbf{s}^m_\ell Y^m_\ell + M_\ell R^2 \boldsymbol{\nabla} \psi^m_\ell . \tag{2.D.32d}$$

At this point we add the vectors in Eq. (2.D.32) substitute the result into Eq. (2.D.29a) to replace **h** with ψ's.Adding Eq. (2.D.32a), Eq. (2.D.32b), and Eq. (2.D.32c), gives us Eq. (2.D.32d). We see that the left-hand side reproduces the last term on the right-hand side of our Eq. (2.D.29a). Now the displacement field has the form of

$$\begin{aligned}
&\mathbf{u}(r,\theta,\phi)\\
&\quad=\sum_{\ell=0}^{\infty}\sum_{m=-\ell}^{\ell}\left[-M_\ell r^2\boldsymbol{\nabla}\psi_\ell^m+\mathbf{h}_\ell^m r^\ell Y_\ell^m\right]\\
&\quad=\sum_{\ell=0}^{\infty}\sum_{m=-\ell}^{\ell}\left[-M_\ell r^2\boldsymbol{\nabla}\psi_\ell^m+\left(\frac{r^\ell}{R^\ell}\right)\mathbf{s}_\ell^m Y_\ell^m+M_\ell R^2\boldsymbol{\nabla}\psi_\ell^m\right]\\
&\quad=\sum_{\ell=0}^{\infty}\sum_{m=-\ell}^{\ell}\left[\left(\frac{r^\ell}{R^\ell}\right)\mathbf{s}_\ell^m Y_\ell^m+M_\ell\left(R^2-r^2\right)\boldsymbol{\nabla}\psi_\ell^m\right], \qquad (2.D.33)
\end{aligned}$$

removing the explicit dependence of **h** from **u**.

There is, however, still an **h**-dependences in Eq. (2.D.33) through the function ψ_ℓ^m. To remove the remaining **h**-dependences from Eq. (2.D.33) we notice that if we take the gradient of Eq. (2.D.32d), we reproduce the left-hand side of Eq. (2.D.24a).

$$\boldsymbol{\nabla}\cdot\left[\mathbf{h}_\ell^m r^\ell Y_\ell^m\right]=\boldsymbol{\nabla}\cdot\left[\left(\frac{r^\ell}{R^\ell}\right)\mathbf{s}_\ell^m Y_\ell^m+M_\ell R^2\boldsymbol{\nabla}\psi_\ell^m\right] \qquad (2.D.34)$$

$$=\boldsymbol{\nabla}\cdot\left[\left(\frac{r^\ell}{R^\ell}\right)\mathbf{s}_\ell^m Y_\ell^m\right]+\underbrace{M_\ell R^2\nabla^2\psi_\ell^m}_{\text{equals zero}} \qquad (2.D.35)$$

$$\Psi_\ell=\sum_{m=-(\ell+1)}^{\ell+1}\boldsymbol{\nabla}\cdot\left\{\left(\frac{r^{\ell+1}}{R^{\ell+1}}\right)\mathbf{s}_{\ell+1}^m Y_{\ell+1}^m\right\} \qquad (2.D.36)$$

2.D.7 General Solution for Spherical Boundary Conditions

So far we have

$$\mathbf{u}(r,\theta,\phi)=\sum_{\ell=0}^{\infty}\left[M_\ell\left(R^2-r^2\right)\boldsymbol{\nabla}\Psi_\ell+\sum_{m=-\ell}^{\ell}\left(\frac{r^\ell}{R^\ell}\right)\mathbf{s}_\ell^m Y_\ell^m\right] \qquad (2.D.37a)$$

$$M_\ell=\frac{1}{2}\left(\frac{\lambda+\mu}{\lambda\ell+\mu(3\ell+1)}\right) \qquad (2.D.37b)$$

$$\Psi_\ell=\sum_{m=-(\ell+1)}^{\ell+1}\boldsymbol{\nabla}\cdot\left\{\left(\frac{r^{\ell+1}}{R^{\ell+1}}\right)\mathbf{s}_{\ell+1}^m Y_{\ell+1}^m\right\} \qquad (2.D.37c)$$

$$Im\left[\sum_{m=-\ell}^{\ell}\left(\frac{r^\ell}{R^\ell}\right)\mathbf{s}_\ell^m Y_\ell^m\right]=0. \qquad (2.D.37d)$$

Until now we have assumed that $\mathbf{S}$ and $\mathbf{u}$ were Cartesian vectors, but in this final form we see that these vectors can be written in any coordinates system in which we can compute the gradient and divergence of a vector field. We also need to construct the $\mathbf{S}$ so that it is real, harmonic, and matches the boundary conditions at $r = R$. We plug Eq. (2.D.37c) into Eq. (2.D.37a) and vectorize the result to obtain a solution which only depends on the boundary conditions.

$$\mathbf{u}(r,\theta,\phi) = \sum_{\ell=0}^{\infty} \left[M_\ell^* \left(R^2 - r^2\right) \boldsymbol{\nabla}\boldsymbol{\nabla} \cdot \mathbf{S}_\ell + \mathbf{S}_\ell\right] \tag{2.D.38a}$$

$$M_\ell^* = \frac{1}{2}\left(\frac{1}{2(1-\nu)(2\ell-1)-\ell}\right) \tag{2.D.38b}$$

To make our final answer as dimensionless as possible, we drop the first Lamé constant in favor of the Poisson's ratio.

Recall from Appendix 2.D.6 that on the surface of the sphere we require the vector field $\mathbf{S}_{\ell m}$ to be given by

$$\mathbf{S}_{\ell m} = g_{\ell m} \hat{r} Y_{\ell m}. \tag{2.D.39}$$

To construct a harmonic vector is of this form we write the Cartesian components of this vector field at the surface, expand these components in sums of spherical harmonics, and then multiple each of them the appropriate factor of $(r/R)^\ell$ to make these function harmonic in the interior. These x, y, z Cartesian components are then of the form $Y_{\ell m}\sin(\theta) cos(\phi)$, $Y_{\ell m}\sin(\theta) cos(\phi)$, $Y_{\ell m}\cos\theta$ respectively. Using the usual rules for the addition of angular momentum, these products can be expanded in sums of other spherical harmonics. Specifically, we may use the fact that the product of two spherical harmonics may be expanded in terms of a sum of spherical harmonics using the Wigner $3-j$ symbols

$$\begin{aligned} Y_{\ell_1}^{m_1} Y_{\ell_2}^{m_2} &= \sum_{\ell m} \sqrt{\frac{(2\ell_1+1)(2\ell_2+1)(2\ell+1)}{4\pi}} \times \\ &\times \begin{pmatrix} \ell_1 & \ell_2 & \ell \\ m_1 & m_2 & m \end{pmatrix} Y_\ell^{-m} \begin{pmatrix} \ell_1 & \ell_2 & \ell \\ 0 & 0 & 0 \end{pmatrix}. \end{aligned} \tag{2.D.40}$$

The Wigner $3-j$ symbols are simply related to the better known Clebsch-Gordan coefficients. The reader may refer to any standard reference on quantum mechanics [135, 136]. In the products above ℓ_1, m_1 refer to the angular harmonic of the imposed surface deformation and ℓ_2, m_2, the decomposition of the radial unit vector into its Cartesian components.Thus, $\ell_2 = 1$, and $m_2 = \pm 1, 0$. Given this simplification, it is useful to define $A^{\pm,0}_{\pm}$ where the lower indices refer an increase or decrease of the total angular momentum: $\ell \to \ell \pm 1$, while the upper index refers to the change in its z-axis projection: $m \to m \pm 1, m$

$$A^{\pm}_{-}(\ell, m) = \frac{-1}{2}\sqrt{\frac{3}{2\pi}}\sqrt{\frac{(\ell \mp m - 1)(\ell \mp m)}{(2\ell - 1)(2\ell + 1)}} \tag{2.D.41}$$

$$A^{\pm}_{+}(\ell, m) = \frac{1}{2}\sqrt{\frac{3}{2\pi}}\sqrt{\frac{(\ell \pm m + 2)(\ell \pm m + 1)}{(2\ell + 1)(2\ell + 3)}} \tag{2.D.42}$$

for the terms generating m values of $m \pm 1$ and

$$A^{0}_{-}(\ell, m) = \sqrt{\frac{3}{4\pi}}\sqrt{\frac{(\ell^2 - m^2)}{(2\ell - 1)(2\ell + 1)}} \tag{2.D.43}$$

$$A^{0}_{+}(\ell, m) = \sqrt{\frac{3}{4\pi}}\sqrt{\frac{(\ell + m + 1)(\ell - m + 1)}{(2\ell + 1)(2\ell + 3)}} \tag{2.D.44}$$

for the terms with the same m value as the radial surface deformation.

At this point it is useful to define $Y_{\ell m}$ for $m < 0$

$$Y_{\ell m} = \tfrac{1}{i\sqrt{2}}\left[Y_{\ell}^{|m|} - (-1)^m Y_{\ell}^{-|m|}\right] \quad m < 0 \tag{2.D.45}$$

This is simply a rotation of $Y_{\ell|m|}$ mode through an angle $\phi_0 = \frac{\pi}{2m}$. Defining $Y_{\ell m}$ for all $m \in \mathbb{I}$ allow us to describe a mode rotated by any angle. This notation is useful in the Cartesian representation of the deformation field.

Using this decomposition of the $\mathbf{S}_{\ell m}$ vector into its spherical harmonic components, multiplying each by the appropriate power $(r/R)^{\ell}$ to make this vector field harmonic in the sphere's interior, and using the above notation, we find:

$$
\begin{aligned}
&S_x = \mathrm{Sgn}(m) g_{\ell m}\sqrt{\frac{2\pi}{3}}\Bigg\{ \\
&\left(\frac{r}{R}\right)^{\ell-1}\Big[A_-^-(\ell,m)\times\left(1-2\delta_{m,0}\right)Y_{\ell-1,m-1} - A_-^+(\ell,m)\left(1-\delta_{m,-1}\right)Y_{\ell-1,m+1}\Big] + \\
&\left(\frac{r}{R}\right)^{\ell+1}\Big[A_+^-(\ell,m)\left(1-2\delta_{m,0}\right)Y_{\ell+1,m-1} - A_+^+(\ell,m)\left(1-\delta_{m,-1}\right)Y_{\ell+1,m+1}\Big]\Bigg\}
\end{aligned}
\tag{2.D.46}
$$

$$
\begin{aligned}
&S_y = -\mathrm{Sgn}(m) g_{\ell m}\sqrt{\frac{2\pi}{3}}\Bigg\{ \\
&\left(\frac{r}{R}\right)^{\ell-1}\Big[A_-^-(\ell,m)\times Y_{\ell-1,-m-1} + A_-^+(\ell,m)Y_{\ell-1,-m+1}\Big] + \\
&\left(\frac{r}{R}\right)^{\ell+1}\Big[A_+^-(\ell,m)Y_{\ell+1,-m-1} - A_+^+(\ell,m)Y_{\ell+1,-m+1}\Big]\Bigg\}
\end{aligned}
\tag{2.D.47}
$$

$$
S_z = g_{\ell m}\sqrt{\frac{4\pi}{3}}\left\{\left(\frac{r}{R}\right)^{\ell-1}A_-^0(\ell,m)Y_{\ell-1,m} + \left(\frac{r}{R}\right)^{\ell+1}A_+^0(\ell,m)Y_{\ell+1,m}\right\},
\tag{2.D.48}
$$

where we have written the result in terms of the real spherical harmonics defined in the text so that each term of the above harmonic vector is explicitly real. Finally, we have introduced *sign function* $\mathrm{Sgn}(x) = +1$ for nonnegative x and -1 otherwise.

Finally, for completeness we record the Cartesian components of the displacement vector field $\mathbf{u}(\mathbf{x})$ for a given radial deformation field on the sphere's surface taken to be a single (real) spherical harmonic:

$$
\begin{aligned}
u_x = g_{\ell m}\frac{r^{\ell-1}}{4R^{\ell+1}}&\Bigg[\left(2r^2\sqrt{\frac{1}{(4\ell^2-1)}} - \frac{\left(R^2-r^2\right)\left(\ell-4\nu+5\right)\sqrt{\frac{(2\ell+1)}{(2\ell-1)}}}{\ell(4\nu-3)+2\nu-1}\right) \\
&\left(\sqrt{(\ell-m-1)(\ell-m)}Y_{\ell-1,m+1} - \mathrm{Sgn}(m-1)^{m-1}\sqrt{(\ell+m-1)(\ell+m)}Y_{\ell-1,|m-1|}\right) \\
&-2r^2\sqrt{\frac{2\pi}{3}}\left(A_+^+(\ell,m)Y_{\ell+1,m+1} - \mathrm{Sgn}(m-1)^{m-1}\ A_+^-(\ell,m)Y_{\ell+1,|m-1|}\right)\Bigg]
\end{aligned}
\tag{2.D.49}
$$

$$\begin{aligned} u_y = g_{\ell m}\frac{r^{\ell-1}}{4R^{\ell+1}} \Bigg[& \left(2r^2\sqrt{\frac{1}{(4\ell^2-1)}} - \frac{\left(R^2-r^2\right)\left(\ell-4\nu+5\right)\sqrt{\frac{(2\ell+1)}{(2\ell-1)}}}{\ell(4\nu-3)+2\nu-1} \right) \\ & \left(\sqrt{(\ell-m-1)(\ell-m)}Y_{\ell-1,m-1} + \mathrm{Sgn}(m-1)^m \sqrt{(\ell+m-1)(\ell+m)}Y_{\ell-1,-|m+1|} \right) \\ & - 2r^2\sqrt{\frac{2\pi}{3}} \left(A_+^-(\ell,m)Y_{\ell+1,m-1} + \mathrm{Sgn}(m-1)^m\ A_+^+(\ell,m)Y_{\ell+1,-|m+1|} \right) \Bigg] \end{aligned} \tag{2.D.50}$$

$$u_z = g_{\ell m}\frac{r^{\ell-1}}{R^{\ell+1}}\sqrt{\frac{4\pi}{3}} \left[r^2 A_+^0 Y_{\ell+1,m} + A_-^0 \frac{\left(2\ell^2+5\ell+3\right)r^2 - (2\ell+1)R^2(\ell-4\nu+5)}{2(\ell(4\nu-3)+2\nu-1)} Y_{\ell-1,m} \right]. \tag{2.D.51}$$

This completes the analysis of the displacement field inside the elastic sphere when a radial deformation whose amplitude is proportional to a single spherical harmonic is imposed on the surface.

Appendix 2.E Modeling growth via applied stress

In our calculation we impose the excess area of the sphere's surface by applying constraint surface tractions as required to generate a specified radial displacement of the surface. The amplitude of that radial displacement is then determined by desired excess area. It is reasonable to ask whether such a procedure is equivalent to demanding the growth of the sphere's surface and then computing the elastic distortions required to accommodate that growth. In this appendix we demonstrate that, within a linear elastic theory, there is a simple correspondence between changes in the elastic reference state, reflecting material growth, and the application of constraint tractions at the boundary of the elastic object.

To begin we consider the simplest case of one elastic degree of freedom. Imagine a single particle bound to the origin by a spring having spring constant k. Its energy of deformation in one dimension is

$$E = \frac{1}{2}kx^2, \tag{2.E.1}$$

where x is the displacement of the particle. In this simple example, a change of reference state entails shifting the origin of the spring from $x = 0$ to $x = x_0$, yielding an energy function

$$E = \frac{1}{2}k(x - x_0)^2 = \frac{1}{2}kx^2 - F_0 x + E_0, \tag{2.E.2}$$

where $F_0 = kx_0$ and the constant in the energy $E_0 = \frac{1}{2}kx_0^2$ has no effect on the statics or dynamics of the system. From Eq. (2.E.2) we see that the effect of shifting the reference state is equivalent to adding a constraint force F_0 to the original energy function for the unshifted spring in Eq. (2.E.1).

We now consider a simplified one-dimension version of linear elasticity theory. We define the reference space labeling the undeformed mass points of the system by X on a segment of the x-axis in the range $[0, 1]$. We now grow this elastic material via the transformation $X \to \lambda X$, with $\lambda = 1 + \delta > 1$ for growth. In the original system displacement vectors $u = \mathbf{u} \cdot \hat{x}$ are defined in terms of the location of those same mass points in the deformed state by

$$u(X) = R(X) - X, \tag{2.E.3}$$

where the mapping $X \to R(X)$ defines the deformation state of the one-dimensional elastic continuum. As expected from the global translational invariance of the energy, the energy density $e(X)$ of the elastic body is proportional to derivatives of the displacement vector with respect to the *reference state label* X. In the system with growth, this becomes

$$e(X) = \frac{1}{2}\mu \left(\frac{\partial}{\partial X} \left[R(X) - X - \delta X \right] \right)^2, \tag{2.E.4}$$

where we have introduced a single elastic constant μ.

Expanding the square as we did for the simple spring system we find that the elastic energy density of deformation in the system with growth λ is given by

$$e(X) = \frac{1}{2}\mu \left(\frac{\partial u}{\partial X} \right)^2 - \sigma \frac{\partial u}{\partial X} + e_0, \tag{2.E.5}$$

where $\sigma = \mu\delta$ now acts as a surface traction and the constant in the energy density is, once again, physically irrelevant. Thus, we see in a one dimensional model of linear elasticity, growth of the reference state is identical mechanically to applying the appropriate set of surface tractions. In our calculation, we did not know these tractions *a priori* , but determined them later by required a fixed increase in the surface area of the growing and elastically deformed structure.

The principle demonstrated here applies for three dimensional vectorial displacements at the cost of some trivial complexity involving indices. Note that the equivalence exploited here is valid only if one assumes a linear elastic material for which all terms in the energy functional are quadratic in the strain tensor. It is only in this case that expanding the square generates a linear shift in the energy interpreted as the surface traction and an irrelevant additional constant. Future studies of nonlinear elastic systems will require a more sophisticated approach to the problem of changing the reference state of the material.

Appendix 2.F Critical stress for Buckling

One may calculate the critical surface stress required for the morphological transition using the elastic theory. We calculate the critical stress by computing the surface stress of the $\ell = 0$ mode as a function of g_{00}. This critical surface stress has the form:

$$\sigma^\star = \mu \frac{(1+\nu)\sqrt{2/\pi}}{1-2\nu} g_{00}. \tag{2.F.1}$$

We now need to find a from for g_{00}. We then use the critical fractional excess area $\Delta^\star$ to solve for the value of g_{00} at the buckling transition. $\Delta^\star$ may be approximated as a function of α and ν, the Poisson ratio of the interior:

$$\Delta^\star \approx \frac{f(\nu)}{\alpha^{1/3}}. \tag{2.F.2}$$

The function $f(\nu)$ is difficult to produce in closed form, but we find that the following polynomial serves as a good numerical approximation for $\nu \geq 0$:

$$f(\nu) = -7.92208\nu^3 + 10.2125\nu^2 - 9.19217\nu + 3.0332. \tag{2.F.3}$$

All that remains is to invert Eq. (2.2.25) for the case of $\ell = 0$ and solve for g_{00} in terms for $\Delta^\star$. Expanding the square root to second order in Δ yields

$$g_{00} \approx 4\pi \left(\tfrac{1}{2}\Delta - \tfrac{1}{8}\Delta^2\right) \tag{2.F.4}$$

Combining Eqs. (2.F.1), (2.F.2) and (2.F.4) and using Eq. (2.2.12) to replace μ by $\alpha\kappa/R^3$, we arrive at the critical stress:

$$\sigma^\star = \frac{\kappa}{R^3}\frac{(1+\nu)\sqrt{2}}{1-2\nu}\left(f(\nu)\alpha^{2/3} - \frac{f^2(\nu)\alpha^{1/3}}{4}\right). \tag{2.F.5}$$

CHAPTER 3

Transitions in the Mechanical Response of Proteins

3.1 Introduction

Investigations by Zocchi and collaborators [137–139] of the dynamics of folded proteins under the influence of a sinusoidally modulated force provide insight into the mechanical response of those molecules to external forces. These investigations probe both the interactions and the dynamics associated with conformational changes in proteins. The latter aspect of the work promises to enhance our understanding of the action of proteins, since conformational adjustments, particularly substantial alterations in the tertiary structure of these molecules, are central to their action in key biological settings [140, 141].

In the experimental system studied by Zocchi *et. al.* a collection of guanylate kinase enzymes tether 20 nm gold nano-particles to a planar gold substrate through Cysteins that are mutagenically introduced into those enzymes. An oscillating electrophoretic force, generated by applying an AC voltage between the gold substrate and a parallel electrode, drives the charged gold nano-particles; the motion of those nano-particles is then measured with the use of evanescent wave scattering. The large number of gold nano particles in the sample that participate in the motion allow for the detection of displacements that are considerably smaller than thermal motion would predict. Those displacements map directly onto the deformation of the enzymes.

A key finding that emerges from these investigations is the existence of a relatively abrupt crossover as the driving force increases, from elastic response to a response that is dominantly viscous. This crossover is described as a “viscoelastic transition.” Reference [139] discusses the nature of the transition and describes two response regimes. First, when the displacement is small, the most accurate underlying model of the enzyme appears to be a Hookean spring, for which the equation of motion is simply $x(t) = f(t)/k$, where $f(t)$ is the applied sinusoidal force. This representation of the protein characterizes its deformation in terms of a single collective coordinate, $x(t)$, and neglects both inertial and dissipative effects. On the other hand, for sufficiently large driving force, the motion is described in terms of a Maxwellian model of a dissipative system [142], schematically displayed in Fig. 3.1.

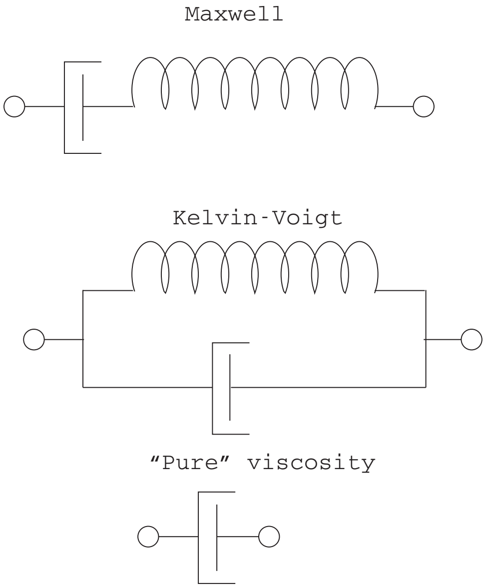

Figure 3.1: Schmematics of simple viscoelatic systems

Two simple models for a viscoelastic system, along with a model for a system governed entirely by viscosity. The springs have spring constants equal to k, and the viscous coefficient for the dash pots is γ.

The equations of motion that govern this system are

$$\gamma \frac{dy(t)}{dt} = f(t) \tag{3.1.1}$$

$$x(t) = y(t) + \frac{\gamma}{k}\frac{dy(t)}{dt} \tag{3.1.2}$$

where $x(t)$ once again tracks the deformation of the enzyme, which is directly related to the displacement of the gold nano particle, while $y(t)$ is an “internal" degree of freedom of the system. (A further time differentiation of Eq. (3.1.2) renders it in the familiar form relating strain rate to the stress and its rate of change.) According to [139], the mechanism that drives the transition is an underlying energy versus displacement curve that changes from quadratic—i.e., harmonic—at low displacement, to linear at higher displacements. The precise nature of this form of potential energy curve is not expanded on in that reference.

Inspired by the above results, we have explored the dynamical response of a somewhat different —but unified—depiction of the driven protein system. Our approach is based on a Kelvin-Voigt model for a viscoelastic substance, as shown in Fig. 3.1. The spring in this system is not, however, strictly Hookean. Rather the energy of the spring as a function of displacement, $V(x)$, which gives rise to a restoring force $F(x)$, is schematically displayed in Fig. 3.2. In our initial analysis, we ignore inertial effects, under the assumption that the system is heavily over-damped. We find that the system displays an unexpectedly rich range of behavior, including symmetry breaking— and restoration—dynamical phase transitions, as well as noise driven rounding and “switching" in bi-stability and many features reminiscent of equilibrium thermodynamic phase transitions, such as spinodals and multicriticality. Preliminary investigations of the effects of inertia on the dynamical equations reveal an even richer range.

There is at least one precedent for a dynamical transition in a driven system of the type that is explored here. The Suzuki-Kubo equation describes the behavior of a mean field version of the Ising model with dissipative dynamics in which the spin variables are driven by a magnetic field with sinusoidal time dependence [143]. At low temperatures, the response to the driving field undergoes a dynamical transition, from an oscillation about an equilibrium ferromagnetic state at small amplitude of the drive to an oscillation at larger drive amplitudes centered about spin magnitude equal to zero [144]. This dynamical transition can be either continuous or first-order, depending on the temperature. However, the physics underlying that model differs fundamentally from the phenomena explored here.

The remainder of this chapter is organized as follows. In Sec. 3.2 the basic model is introduced and the deterministic, noise free, dynamical phase diagram is displayed summarizing the basic behavior. In Sec. 3.3, to provide additional insight, we provide some analytical results for the model with a piecewise continuous restoring force. In the following section, Sec. 3.4, we make contact with typical dynamical responses, as measured in experiments on viscoelastic materials in general and in the experiments of Zocchi et al. in particular. For the basic over-damped deterministic case we discuss the nature of the transitions and compare the analysis to that of standard mean field theory for thermodynamic phase transitions in Sec. 3.5. Section 3.6 contains a preliminary investigation into the effects of inertia, while the effect of noise on the transitions and response functions is discussed in Sec. 3.7 via Langevin over-damped dynamics and a master equation. Concluding remarks follow, including a short discussion of the consequences of a restoring force without the symmetry shown in Fig. 3.2. Appendices contain some details on our "standard model," a comparison to mean field thermodynamics and a brief commentary on an alternate version of the restoring force.

3.2 Model, dynamical phase diagram, and characterization of response

Our model is a highly simplified depiction of a folded protein, in which we single out a collective degree of freedom that we assume dominates the response of the molecule to an external force. As a caricature of its much more complex structure, we assume a system described by the Kelvin-Voigt model of viscoelasticty [142, 145], as shown in Fig. 3.1, which, as we will see, appears natural for a driven, over-damped, nonlinear oscillator. The spring in this model can be thought of as a gross simplification of the Tirion model for protein interactions [146], with the caveat that our coordinate, x, is a collective one, while the Tirion model replaces the various interactions between the actual constituents of a protein by harmonic bonds between idealized point-like entities. In addition, we assume the possibility of the "cracking" of this protein under sufficient external stress [147–149] through the reversible detachment of the spring. This means that the harmonic potential energy expression holds only in a limited range of values of x. According to the model we adopt, at sufficiently large values of $|x|$ the potential energy and associated restoring force depart from strict Hookean form to approach either a constant energy (and, correspondingly, no restoring force) or a fixed, constant restoring force corresponding to a linear, rather than quadratic, energy. Figure 3.2 is a schematic depiction of a particular version of such a force and associated energy function. Inside a region centered at the origin, $x = 0$, the potential is nearly harmonic and the force is approximately Hookean. Outside this central region the force approaches constant values $\pm F_0$, and the associated confining potential is linear. The precise form of the restoring force utilized in our calculations is described in Appendix 3.A.

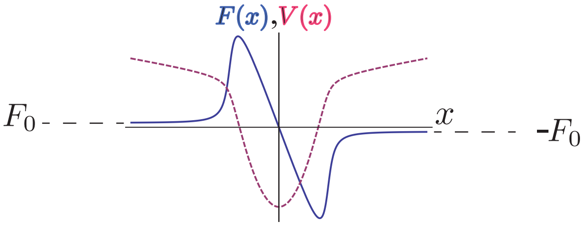

Figure 3.2: Model force and energy curves

The potential energy, $V(x)$, (red, dashed) and associated restoring force, $F(x)$, (blue, solid) that we assume in our model. The force approaches $\pm F_0$ for large x, as indicated in the figure.

We assume initially that the motion of our system is highly over-damped, so that the time rate of change of the displacement coordinate x is directly proportional to the force generating change in the system. Given the restoring force shown in Fig. 3.2 and a periodic external force, the equation of motion takes the form

$$\frac{dx(t)}{dt} = \frac{1}{\gamma}\left[F(x(t)) + A\sin(\omega t)\right] \tag{3.2.1}$$

where the parameter γ encodes viscous effects.

Figure 3.3 indicates the resulting behavior when the drive amplitude, A, and F_0, the asymptotic absolute strength of the confining force, are scanned.

In Regions 1 and 1a, color-coded blue, the steady state periodic solution, is symmetric about the origin. In Region 2, color-coded red, the dynamically stable solution is skewed, either to the right or the left of the origin. As it turns out, skewed solutions appear in pairs; see Appendix 3.B. There is also a symmetric steady state solution that is, however,

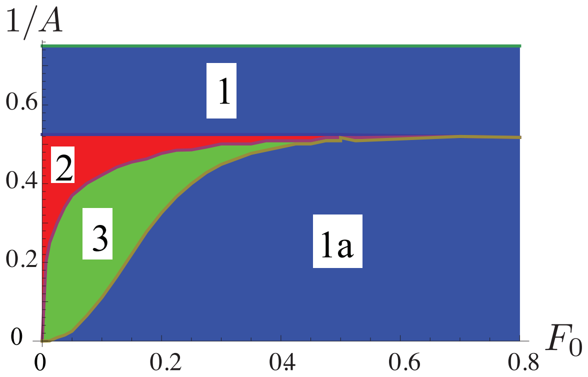

FIGURE 3.3: DYNAMICAL PHASE DIAGRAM

Dynamical phase diagram of the types of response to a sinusoidal drive exhibited by Kelvin-Voigt model governed by the equation of motion Eq. (3.2.1) with restoring force $F(x)$ as shown in Fig. 3.2. The horizontal axis is the absolute value of the asymptotes of the restoring force at large $|x|$. The vertical axis is the inverse of the drive amplitude, A. The parameter α controlling the transition from Hooke's law to constant restoring force (see Eqs. (3.A.1) and (3.A.6) and Fig. 3.29) has been set equal to 0.01. The frequency of the drive, ω, is equal to $1/2$, and the viscosity parameter, γ, is set equal to one.

dynamically unstable. In Region 3, color-coded green, three dynamically stable, steady state solutions exist, one symmetric and the other two skewed. In addition, there are two skewed, *dynamically unstable*, steady state solutions. Finally, a region complementing Region 3, separating Region 1 from Region 2, is not shown as it is exceedingly narrow and beyond the resolution in Fig. 3.3.

Figures 3.4–3.6 illustrate the (steady state) solutions characteristic of the four regions in Fig. 3.3. The time interval shown corresponds to two periods of the driving force. The parameters A and F_0 corresponding to the region of the phase diagram are provided in the captions, while $k = 2$, corresponding to the spring constant in the harmonic regime, and $\omega = 0.5$ for the driving force are kept constant in these figures. The friction constant $\gamma = 1$ sets the time scale.

Given the very different properties of the steady states in the four regions, the boundaries between the regions are necessarily sharp. We will return to the nature of the transitions that take place as those boundaries are traversed.

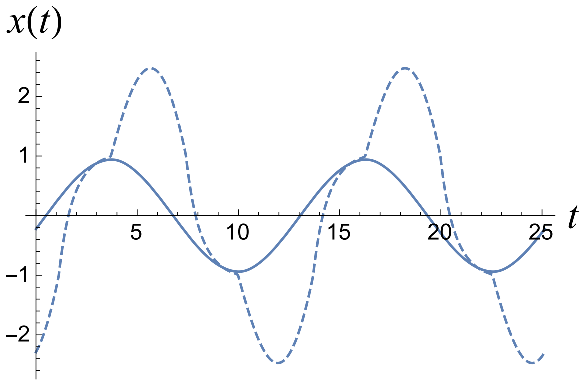

Figure 3.4: Steady state response in region 1

The steady state response in Region 1 (solid curve) and in Region 1a (dashed curve). Both are dynaically stable. The inverse of the drive amplitude, $1/A$, is 0.53 for the Region 1 response and 0.51 for the Region 1a response. The asymptotes of the restoring force outside the harmonic regime are $\pm F_0$ with $F_0 = 0.6$, and the value of the spring constant in the Hooke's law region is $k = 2$. The frequency of the driving force is $\omega = 0.5$. The transition between a harmonic restoring force and a force equal to $\pm F_0$ occurs at $|x| \simeq 1$. The restoring force is given in Appendix 3.A with parameter $\alpha = 0.01$.

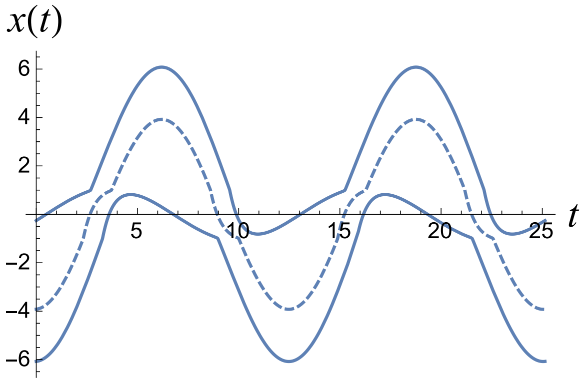

Figure 3.5: Steady state response in region 2

The three steady state responses in Region 2. The solid, skewed, curves are dynamically stable and the dashed, symmetric, curve is dynamically unstable. The quantity F_0 is 0.1 and $1/A = 0.45$. All other parameters are the same as in Fig. 3.4.

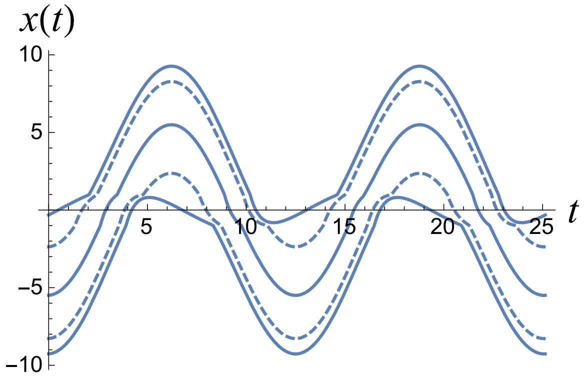

Figure 3.6: Steady state response in region 3

The five steady state responses in Region 3. The solid symmetric curve and the two solid skewed curves are dynamically stable, while the two skewed curves shown dashed are dynamically unstable. The quantity F_0 is 0.1, and the inverse of the drive amplitude, $1/A$, is 0.35. All other parameters are the same as in Figs. 3.4 and 3.5.

For the time being, it is worthwhile to consider the two solutions for $x(t)$ shown in Fig. 3.4. They differ in a few respects. First, although the driving force strengths differ by less than 5%, the displacement amplitudes are quite different. Second, the curve describing the solution in Region 1 is nearly sinusoidal (in fact, nearly in phase with the drive, which goes as $\sin(\omega t)$, while the steady state solution for Region 1a is somewhat distorted. Furthermore, the latter solution is well out of phase with respect to the drive. As we will see, the steady state solution in Region 1 is close to elastic—i.e., nondissipative—while the the behavior in Region 1a is strongly dissipative.

3.3 Analytical solution in a limiting case

To gain a perspective on the nature of solutions of Eq. (3.2.1), we consider of that equation under the limiting assumption of a sharp break between the regime in which the restoring force is strictly linear and the range of the displacement variable x in which it is considerably gentler. If the restoring force outside the harmonic regime *vanishes*, the function $F(x)$ has the form

$$F(x) = \begin{cases} -kx & |x| < x_0 \\ 0 & |x| \geq x_0 \end{cases} \tag{3.3.1}$$

The solutions to Eq. (3.2.1) in the two regimes are

$$x_i(t) = Be^{-kt/\gamma} - \frac{A}{\sqrt{\gamma^2\omega^2 + k^2}} \cos\left(\omega t + \arctan\frac{k}{\gamma\omega}\right) \tag{3.3.2}$$

$$x_e(t) = B' - \frac{A}{\gamma\omega}\cos(\omega t)\,, \tag{3.3.3}$$

where the subscripts i and e refer to behavior in the "interior" region $|x| < x_0$ and the "exterior" region $|x| \geq x_0$. A complete solution to the equation of motion requires adjusting the coefficients B and B' so as to match $x_i(t)$ and $x_e(t)$ at the boundary between the two regimes.

When the frequency of the driving force is small, the characters of the "exterior" and "interior" responses differ fundamentally. In the exterior region, the steady state velocity, $v_e(t) = dx_e(t)/dt$, is in phase with the driving force, which means that the drive's energy feeds optimally into viscous damping. On the other hand, when $\gamma\omega \ll k$, $dx_i(t)/dt$ is almost ninety degrees out of phase with the driving force, so the response is nearly the same as at static equilibrium, in that the two terms in square brackets in Eq. (3.2.1) nearly cancel, and the dissipation is quite small. In the regime of low frequency response, we can roughly characterize the dynamics in the exterior region as *viscous* and the behavior in the interior region as *elastic*. It is therefore reasonable to expect that as the driving amplitude, A, increases, the response will evolve from elastic to viscous.

However, as strongly indicated by the phase diagram shown above, the change from elastic to viscous response entails an abrupt transition in the dynamical behavior. This transition occurs near the drive amplitude for which the coordinate x visits the region outside the harmonic regime (in fact, it occurs at a slightly lower drive amplitude). At this point skewed solutions to the equation of motion appear and, in fact, coexist with solutions remaining entirely within the harmonic regime.

Figure 3.7 shows two full periods of two skewed solution to the equation of motion

Eq. (3.2.1) with confining potential Eq. (3.3.1). The displacement limits outside of which

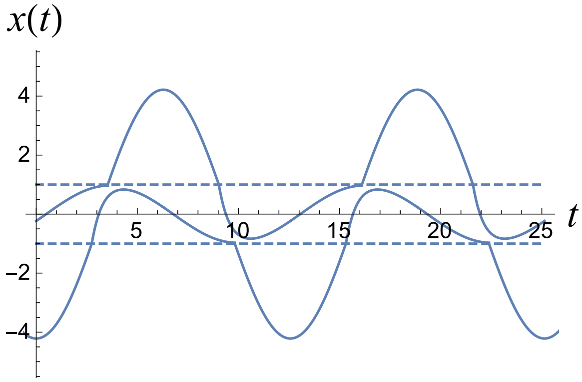

FIGURE 3.7: SKEWED SOLUTION IN REGION 3

Two skewed solutions to Eqs. (3.2.1) and (3.3.1). The value of x_0 has been set equal to one.

which the restoring force vanishes are indicated by dashed lines. Note the slope discontinuities when those limits are traversed. This is permissible in a system in which inertia is ignored. The trajectories consist of the two solutions Eqs. (3.3.2) and (3.3.3), grafted together at the boundaries between their regimes of applicability. From the nature of the solution for $|x(t)| > x_0$, we see that, in the case of the solution skewed above the x axis, the intervals in which the solution for $|x(t)| < x_0$ applies, as depicted in Fig. 3.7, will satisfy

$$(2n+1)\pi/\omega + t_0 < t < (2n+3)\pi/\omega - t_0\,, \tag{3.3.4}$$

corresponding to time windows lying symmetrically within the interval between successive odd multiples of the period of the forcing term, $2\pi/\omega$. We can write for the form of a solution in such a time window

$$\begin{aligned} x(t) = &-\frac{A}{\omega\sqrt{1+(k/\omega)^2}}\cos(\omega t + \arctan(k/\omega)) \\ &+ Ce^{-k(t-(2n+1)\pi/\omega - t_0)} \end{aligned} \tag{3.3.5}$$

Here and henceforth, we have set the parameters $\gamma = 1, x_0 = 1$. In order for the solution in Eq. (3.3.5) to properly match the solution for $|x(t)| > x_0$ at the limits of the window, we require

$$
\begin{aligned}
x_0 = &-\frac{A}{\omega\sqrt{1+(k/\omega)^2}}\cos((2n+1)\pi+\omega t_0 \\
&+\arctan(k/\omega))+C \qquad (3.3.6)\\
x_0 = &-\frac{A}{\omega\sqrt{1+(k/\omega)^2}}\cos((2n+3)\pi-\omega t_0 \\
&+\arctan(k/\omega))+Ce^{-2\pi k/\omega+2kt_0} \qquad (3.3.7)
\end{aligned}
$$

We can eliminate the constant C between these two equations, and we are left with the equation for t_0

$$
\begin{aligned}
&\frac{A}{\omega\sqrt{1+(k/\omega)^2}}\Big[\cos(-\omega t_0+\arctan(k/\omega)) \\
&\quad - e^{-2\pi k/\omega+2kt_0}\cos(\omega t_0+\arctan(k/\omega))\Big] \\
&\quad + x_0\left(e^{-2\pi k/\omega+2kt_0}-1\right)=0 \qquad (3.3.8)
\end{aligned}
$$

The left hand side of Eq. (3.3.8) as function of t_0 is displayed in Fig. 3.8, with the variables x_0, k and ω set so as to correspond to their values in the phase diagram in Fig. 3.3. As shown in Fig. 3.8, smaller amplitudes correspond to lower curves. the left hand side of the equation through zero for Note that there is always a solution $\omega t_0 = \pi$, which says that the window in

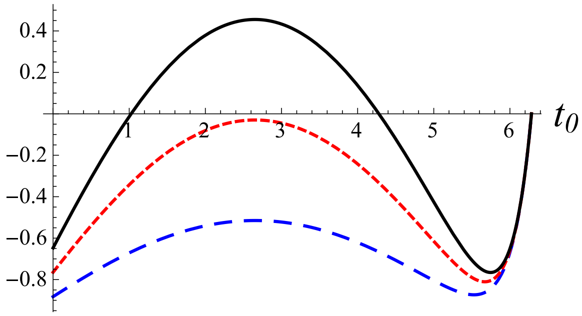

Figure 3.8: Example of left hand side of Eq. (3.3.8)

The left hand side of Eq. (3.3.8) as a function of t_0, with $x_0 = 1$, $k = 2$ and $\omega = 0.5$. The three curves correspond to the following three values of the drive amplitude: $A = 1$ (blue long-dashed curve), $A = 2$ (red dashed curve), $A = 3$ (black solid curve).

Eq. (3.3.4) has shrunk to zero. This is reasonable since it is always possible, by setting initial conditions appropriately, to construct a solution in which $x(t)$ lies completely in the regime of vanishing restoring force. When $t_0 = \pi/\omega$ is the *only* solution to Eq. (3.3.8), then solutions to the equations of motion Eq. (3.2.1) with $F(x)$ given by Eq. (3.3.1) either lie completely in the regime $|x| < x_0$ (where, in this example, $x_0 = 1$) or entirely outside of it. At a threshold value of the amplitude, two more apparent solutions arise, as for the solid curve in Fig. 3.8.

The next step is to determine whether the new intersections correspond to solutions of the equation of motion, and, if so, whether those solutions are dynamically stable. As it turns out, one of the two new solutions of Eq. (3.3.8)—the solution corresponding to the larger value of t_0—does indeed correspond to a legitimate response. Furthermore, the response is dynamically stable. Appendix 3.C describes the analysis.

Another interesting aspect of the dynamical behavior is the existence of an exceedingly small range of amplitudes, A, in which a dynamically stable, skewed solution coexists with a symmetric solution lying entirely inside the Hooke's law region. As an example of coexistence Fig. 3.9 shows the left hand side of Eq. (3.3.8) when the parameters are adjusted so that there is a solution to the equation of motion that just fits in the region $-x_0 < x < x_0$. Even though there is such a trajectory, an additional skewed and dynamically stable solution to the equation of motion Eq. (3.2.1) with $F(x)$ given by Eq. (3.3.1) also exists (actually a pair, see below), corresponding to the solution to Eq. (3.3.8) in which $t_0 \approx 2.654$. The region of coexistence is spanned as the drive amplitude A changes by about one part in 10^6. Figure 3.10 shows the three stable solutions. Not shown in the figure are the two unstable skewed solutions to the equation of motion that lie between the symmetric solution and the stable skewed solutions.

Given a solution, $x(t)$ of the equation of motion Eq. (3.2.1) with the kind of restoring force considered here, i.e. a restoring force with the property $F(-x) = -F(x)$, it is straightforward to show that the equation of motion is also satisfied by $-x(t + \pi/\omega)$. From this we can infer from one skewed solution another one, skewed in the opposite direction. This feature was used to construct the pair of skewed solutions in Fig. 3.10. Thus, we have confirmed the

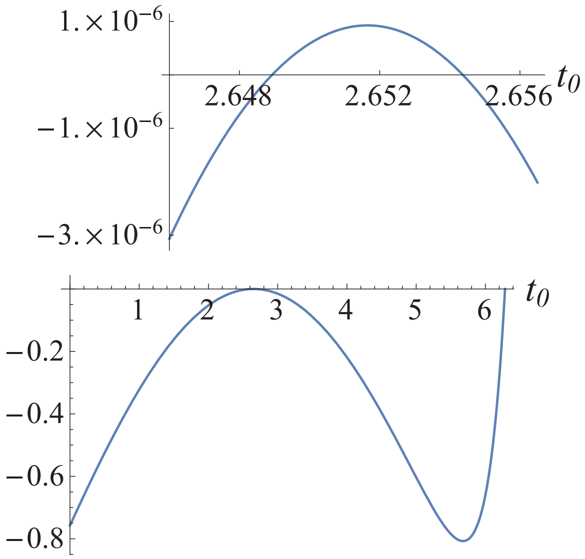

Figure 3.9: Magnified example of left hand side of Eq. (3.3.8)

The left hand side of Eq. (3.3.8) when $k = 2$, $\omega = 0.5$, $\gamma = 1$, $x_0 = 1$ and the drive amplitude A is equal to $\sqrt{k^2 + \omega^2}$. The lower portion of the figure shows the expression for the entire range of t_0, from 0 to π/ω. The upper portion magnifies the portion of the graph in which the left hand side of Eq. (3.3.8) passes through zero.

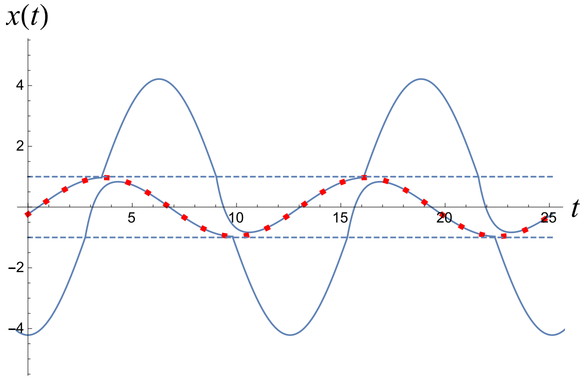

Figure 3.10: Plot of three stable solutions to Eq. (3.2.1)

The three stable solutions to the equation of motion Eq. (3.2.1) with restoring force given by (3.3.1). The parameters are the same as in Fig. 3.9. The two skewed solutions are shown as solid curves and the dots indicate the symmetric solution, which just fits in the Hooke's Law region for the restoring force. The boundaries of that region are shown as dashed lines.

existence of two distinct stable, skewed solutions to the equation of motion for sufficiently high values of the driving amplitude. See Appendix 3.B.

3.4 Loss and storage compliances

To further quantify the transition, we introduce a generalization of the way in which the response of a linear viscoelastic system is characterized in terms of dissipative, or loss, compliances and storage, or elastic, compliances. Given the notation we utilize here, the stress exerted on the system is $A\sin(\omega t)$. The response of the system, if linear, would be of the form

$$\begin{aligned} x(t) &= x_{\text{diss}}(t) + x_{\text{el}}(t) \\ &= -X_d\cos(\omega t) + X_e\sin(\omega t) \\ &= -j_2A\cos(\omega t) + j_1A\sin(\omega t)\,, \end{aligned} \tag{3.4.1}$$

where j_1 is the *storage compliance* and j_2 is the *loss compliance* [145], and the subscripts on the first line of Eq. (3.4.1) stand for "dissipative" and "elastic."

In the case of nonlinear response, it is possible to generalize the above decomposition by extracting the contribution to the response that gives rise to dissipation. We do this by taking the integral of the steady state solution over a period,

$$Y_d = \frac{\omega}{\pi}\int_0^{2\pi/\omega} x(t)\cos(\omega t)dt\,, \tag{3.4.2}$$

in which case we can write

$$\begin{aligned} x(t) &= Y_d\cos(\omega t) + (x(t) - Y_d\cos(\omega t)) \\ &\equiv x_{\text{diss}}(t) + x_{\text{el}}(t) \end{aligned} \tag{3.4.3}$$

The entirety of the dissipative response is contained in $x_{\text{diss}}(t)$ as defined above, in that

$$\int_0^{2\pi/\omega} \sin(\omega t)\frac{dx_{\text{el}}(t)}{dt}dt = 0 \tag{3.4.4}$$

This means that the quantity $-Y_d/\sqrt{2}A$ (see below) plays the role of the dissipative compliance, while there is not necessarily any quantity that can be unambiguously associated with the storage compliance.

We now return to our "standard model" shown schematically in Fig. 3.2. Figure 3.11 displays the two solutions for $x(t)$ shown in Fig. 3.4, divided into dissipative and elastic components. As is clear from the lower plot in the figure, which refers to the response in Region 1a, the elastic response is not simply proportional to the driving force, $A\sin(\omega t)$.

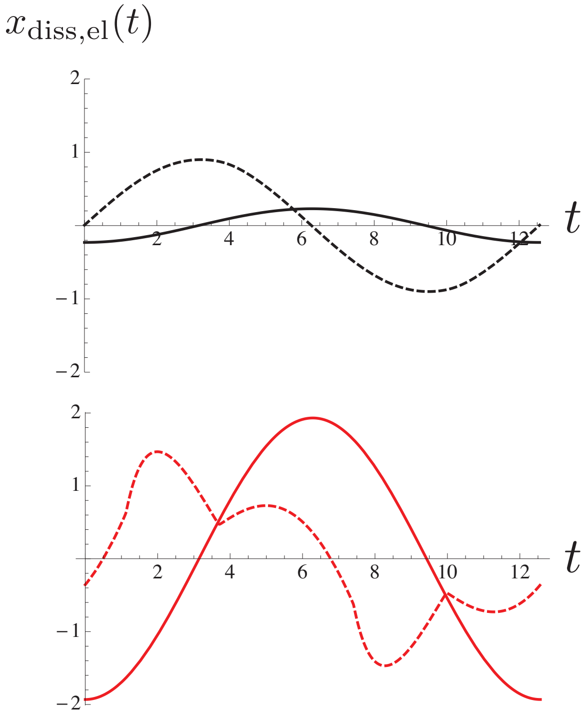

FIGURE 3.11: STORAGE AND LOST RESPONSE FOR SOLUTION IN FIG. 3.4

The two solutions for $x(t)$ shown in Fig. 3.4, broken into dissipative contributions (solid curves) and storage contributions (dashed curves); see Eq. (3.4.3). The top plot shows the solution in Region 1, in which the response is dominantly elastic and the bottom plot shows the solution in Region 1a in which the response is more dissipative. Recall that the inverse of the drive amplitude is 0.53 in the case of the top plot and 0.51 for the bottom plot, and $F_0 = 0.6$.

However, based on the developments above, we can reduce the elastic and dissipative components of the response to two numbers. If

$$I_t^2 = \frac{\omega}{2\pi}\int_0^{2\pi/\omega} x(t)^2 dt\,, \tag{3.4.5}$$

then

$$\begin{aligned}\frac{\omega}{2\pi}\int_0^{2\pi/\omega} x_{\mathrm{diss}}(t)^2 dt &= \frac{Y_d^2}{2} \\ &\equiv I_d^2 \end{aligned} \tag{3.4.6}$$

$$\begin{aligned}\frac{\omega}{2\pi}\int_0^{2\pi/\omega} x_{\mathrm{el}}(t)^2 dt &= I_t^2 - I_d^2 \\ &\equiv I_s^2\,, \end{aligned} \tag{3.4.7}$$

which means we can define an overall compliance as I_t/A, with a storage compliance, $j_1 = I_s/A$, and a loss compliance, $j_2 = I_d/A$.

As a final technicality, we need to address the case in which there are dynamically stable skewed solutions to the equation of motion. The measurements that motivated this study are made on a collection of driven oscillators; furthermore, thermal noise is substantial. As we will see such a system will equilibriate into an ensemble in which the two skewed responses, when they exist, are equally represented. This means that under such conditions, we should replace $x(t)$ in the equations defining the compliance by

$$\langle x(t)\rangle = (x(t) - x(t+\pi/\omega))/2 \tag{3.4.8}$$

Figure 3.12 displays an example of the case in which the response curve is skewed and the average in Eq. (3.4.8) has been performed The full response is shown as well as the two components that comprise it.

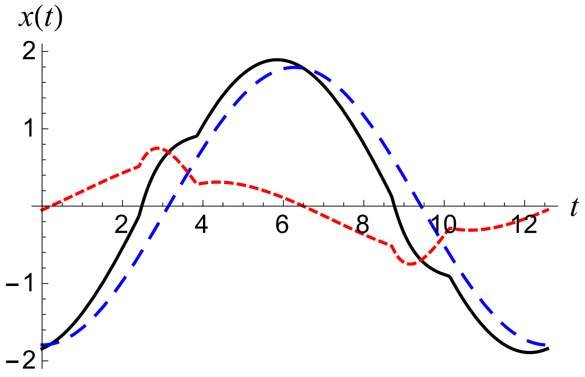

Figure 3.12: The average of the two stable skewed response curves

The solid black curve is the full response. The long dashed blue curve is the dissipative contribution, going as $\cos(\omega t)$, which we term $x_{\mathrm{diss}}(t)$. The dashed red curve is what remains when the dissipative component is subtracted from the full response. We term that response $x_{\mathrm{el}}(t)$ See Eq. (3.4.3). Here, $k = 2$, $\omega = 0.5$, $F_0 = 0$, $\alpha = 0.01$ and A, the drive amplitude, is equal to 1.9.

3.5 On the nature of the dynamical phase transition

Our focus has been the steady state behavior of the dynamical system described by Eq. (3.2.1) When the crossover from a restoring force described by Hooke's Law to a constant restoring force F_0 is not abrupt, the methods of Sec. 3.3 cannot be applied. An alternate approach that proves powerful, useful and universal, utilizes a standard map or recursion relation. This relation follows from the fact that the solution of a first-order differential equation like Eq. (3.2.1) is determined entirely by a single initial condition. That is, if we know $x(0)$, then we can use the equation to forward integrate and determine $x(t)$ at all subsequent times. In particular, we can create a map that takes us from $x(0)$ to $x(2\pi/\omega)$, the value of the dynamical variable one period later. A steady state solution to the equation of motion will have the property $x(2\pi/\omega) = x(0)$—if we can discount the possibility of solutions with a period at a subharmonic of the driving force. Figure 3.13 displays such a recursion graph, calculated from Eq. (3.2.1) with a particular choice of parameter values. Also shown in that figure is the 45° line corresponding to $x(2\pi/\omega) = x(0)$. The small open circles indicate intersection of that line with the recursion curve, corresponding to steady state solutions of

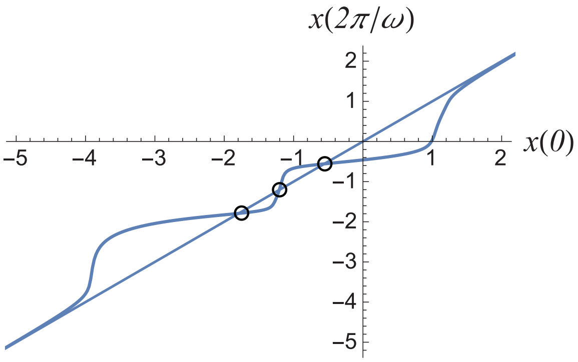

FIGURE 3.13: EXAMPLE OF THE MAP CONNECTING $x(0)$ WITH $x(2\pi/\omega)$

Plot of the quantity $x(t)$ in the equations of motion (3.2.1). Also shown is the line $x(2\pi/\omega) = x(0)$ (straight line). In this case, the drive amplitude, A is 2.75, the frequency, ω, of the drive is 2, k is 2, the parameter α is 0.15 and the asymptotic force, F_0, is equal to zero. As always, $x_0 = 1$ and $\gamma = 1$. The small open circles denote the intersections between the map and the 45° line corresponding to steady state solutions of the equation of motion.

the equation.

We can assess the dynamical stability of the steady state solutions in the standard fashion by iterating the recursion relation [150, 151]. The graphical version of this process is displayed in Fig. 3.14, in which we focus our attention on the section of the curve containing the intersections. The stepwise curves between the map and the 45° line are graphical renditions

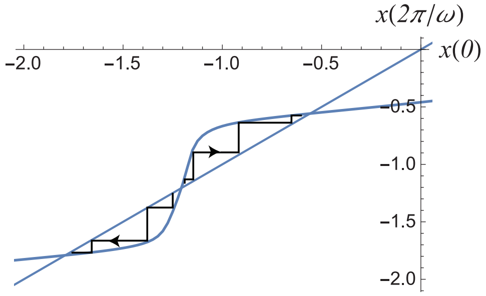

FIGURE 3.14: EXAMPLE OF THE MAP CONNECTING $x(0)$ WITH $x(2\pi/\omega)$ W/EMBED RECURSION RELATION

The result of graphical iterations of the recursion relation embodied in the curve displayed in Fig. 3.13. The broken curves impinge on the recursion curve vertically and on the 45° line horizontally.

of the result of iteration of the recursion relation. As indicated by the arrowheads on those curves, repeated calculations of the quantity $x(t)$ at succeeding intervals of one period tend away from the central intersection and towards one of the flanking ones. We are led to the conclusion that the central solution for a steady state is dynamically unstable, while the two solutions that flank it are, by contrast, dynamically stable. Such a recursion relation yields the solutions one finds in Region 2 of the dynamical phase diagram as shown in Fig. 3.3.

Given a steady state solution for a particular $x(0)$, we can then compute $x(t)$ for the entire interval between $t = 0$ and $t = 2\pi/\omega$, and from this the response properties of that solution. As an example, we can explore in more detail the transitions between the various regions shown in the phase diagram in Fig. 3.3. We start by looking at the portion of the phase diagram that is exactly on the vertical axis, i.e. for which the large-x asymptote of the restoring force is $F_0 = 0$. Making use of the definitions in Sec. 3.4 for total, storage and loss compliances, we obtain results for the quantities I_t/A, I_s/A and I_d/A. Figure 3.15 shows the total compliance, I_t/A, plotted in terms of the amplitude, A, of the drive. Note the discontinuity in the compliance, which can be taken as evidence for a first-order transition. Figure 3.16 shows the two contributions to the total compliance, obtained from I_d/A, and I_s/A.

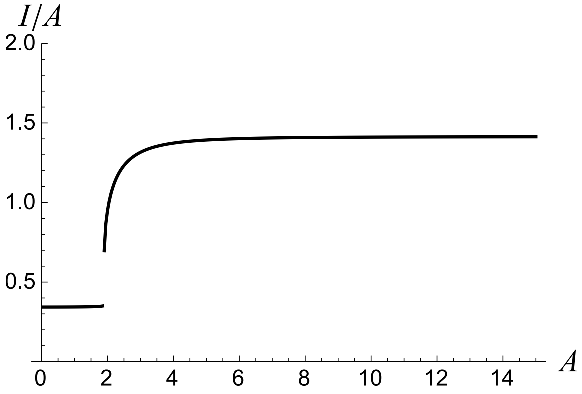

FIGURE 3.15: TOTAL COMPLIANCE IN FIRST-ORDER TRANSITION

The total compliance, I_t/A, plotted agains the drive amplitude, A. Here, F_0=0, $\omega = 0.5$, $k = 2$ and the parameter $\alpha = 0.01$. Here and in Fig. 3.16 the compliances are as defined in Sec. 3.4.

Close investigation reveals a very narrow regime around the point of discontinuity in

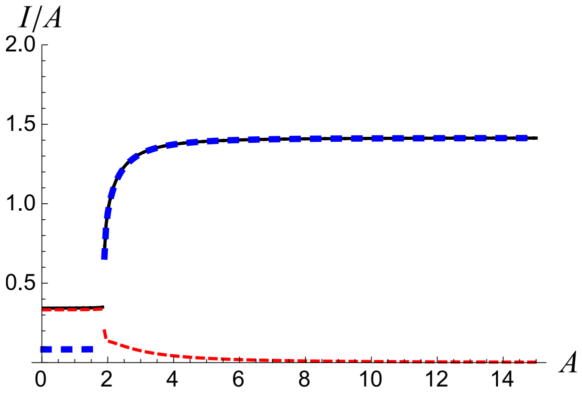

FIGURE 3.16: DISSIPATIVE AND STORAGE COMPLIANCE IN FIRST-ORDER TRANSITION
The two contributions to the total compliance graphed in Fig. 3.15: the dissipative compliance I_d/A (long dashed blue curve), the storage compliance I_s/A (dashed red curve) and the total compliance, (thin black curve).

which there is coexistence between the responses corresponding to the compliances to the right and left of the transition point in Figs. 3.15 and 3.16. The regime is sufficiently thin that it is undetectable given the resolution of the figure.

The discontinuities in the dynamic response graphed in Figs. 3.15 and 3.16 imply a dynamical transition with the characteristics of a first-order thermodynamic phase transition, in that there are discontinuities in key quantities. However, a transition with discontinuities is not inevitable. If the change in the restoring force from harmonic to a constant (in the example being discussed: $F_0 = 0$) is sufficiently gentle, then the dynamical transformation becomes *continuous* in the thermodynamic sense. That is, it remains sharp, but physical properties, such as dynamical moduli, no longer exhibit discontinuities in their dependence on the drive amplitude.

The change in the character of the transition as the properties of the restoring force are altered is illustrated in Figs. 3.17 and 3.18, which display plots highlighting the intersections of recursion curves with the 45° line. In particular, the figures show how the points of intersection change with drive amplitude. The plot in Fig. 3.17 contains four recursion curves, corresponding to four different drive amplitudes. In this case there is a first-order dynamical phase transition. The parameters are—with the exception of ω—the same as in the phase diagram in Fig. 3.3 with $F_0 = 0$. The drive frequency has been set as $\omega = 2$ in order to make certain features of the curve more visible and to expand the coexistence region between Regions 1 and 2. The longer dashed blue curve intersects the 45° line once, corresponding to a single symmetric and stable dynamical steady state. This curve is characteristic of low drive amplitude and (more nearly) elastic response. The (short-) dashed red curve corresponds to the drive amplitude at which one sees the onset of four more steady state solutions to the equation of motion, all of them skewed, two stable and two unstable. In the regime represented by the solid black curve, those additional solutions are clearly visible, and three dynamically stable steady state solutions to the equation of motion coexist – one symmetric and two skewed. The long-dashed red curve corresponds to the high amplitude regime, Region 2 in the phase diagram, in which there are two stable skewed steady state solutions and one unstable symmetric solution to the equation of motion. The restoring force is as given in Appendix 3.A, with parameter $\alpha = 0.01$, the same value as was used to generate the phase diagram in Fig. 3.3.

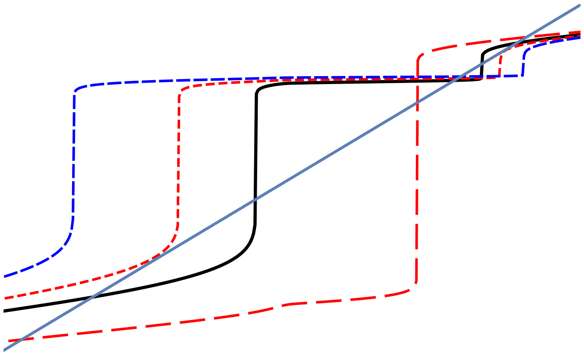

Figure 3.17: $x(0)$ –$x(2\pi/\omega)$ map near first-order transition

Illustrating a first-order transition between Region 1 and Region 2. Referring to Appendix 3.A, the parameters in the restoring force and the equation of motion are as follows: $\omega = 2$, $k = 2$, $x_0 = 1$, $\alpha = 0.01$ and $F_0 = 0$. The longer dashed blue curve and the shorter dashed red curve correspond to Region 1 in the phase diagram in Fig. 3.3. The longest dashed red curve corresponds to Region 2, and the solid black curve to a coexistence region between Regions 1 and 2. Such a region exists but is exceedingly narrow for the set of variables used to generate Fig. 3.3.

Figure 3.18 displays the effect of smoothing out the transition region in $F(x)$. Here, the parameter α has been set equal to 0.15. In this case, the transition from a single, stable and symmetric, steady state solution to three steady state solutions—two skewed and stable and one symmetric and unstable—occurs continuously with no coexistence region and no discontinuities in dynamical response. The drive frequency, ω, has again been set equal to 2, while the spring constant k in the Hooke's Law region is maintained at 2. The short-dashed blue curve corresponds to Region 1, the long-dashed red curve is characteristic of Region 2, and the solid black curve illustrates the onset of the transition between one symmetric, stable solution to the equation of motion and three solutions, two skewed and stable, one symmetric and unstable. No region of coexistence separates the two.

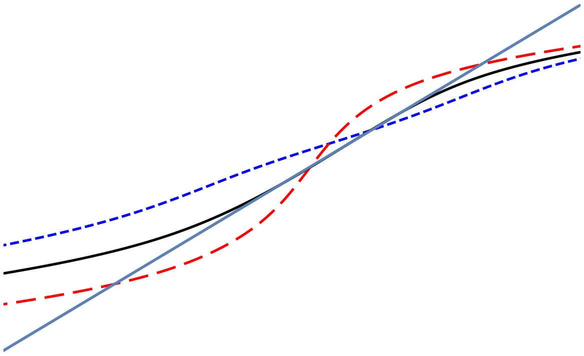

Figure 3.18: $x(0)$ $-x(2\pi/\omega)$ MAP NEAR CONTINUOUS TRANSITION

Illustrating a continuous transition between Regions 1 and 2 in Fig. 3.3 when α is increased from 0.01 to 0.15 so as to stretch out the transition region between a Hooke's Law restoring force and a vanishing restoring force, i.e. $F_0 = 0$. Otherwise the parameters utilized are the same as in Fig. 3.18. See Appendix 3.A A. The dashed blue curve corresponds to Region 1 and the long dashed red curve to Region 2. The solid black curve corresponds to the onset of the transition between the two regions.

Figure 3.19 illustrates the compliances associated with Fig 3.18, quantified in terms of those defined in Sec. 3.4. Because of the particular relative values of ω and k, the compliance in Region 1 of the phase diagram divides equally into viscous and elastic, while in Region 2 viscous response increasingly dominates.

The compliance curves are continuous and without evident features marking the transition

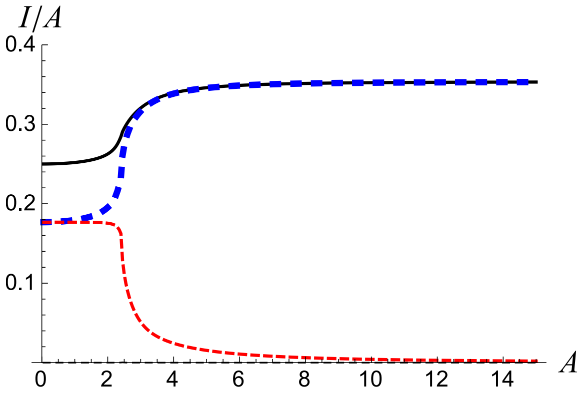

FIGURE 3.19: COMPLIANCE IN CONTINUOUS TRANSITION

In the case of parameter values leading to the plot in Fig. 3.18, the total compliance, I_t/A, (solid black curve) and the three contributions to that compliance: the dissipative compliance I_d/A (long dashed blue curve) and the storage compliance I_s/A (dashed red curve). Here, the transition is continuous. Also shown on the graph is the value of the amplitude, A at which the transition between Section 1 and Section 2 in the phase diagram occurs. For definitions of the compliances see Sec. 3.4.

from Region 1 to Region 2. Very close inspection reveals singularities in the form of mild slope discontinuities in I_t/A, I_s/A and I_d/A, which are unlikely to be detectable in any experimental realization of this system. Figure 3.20 shows the total compliance, I_t/A, in the immediate vicinity of the transition.

The recursion curves bear a close relationship to the free energy extremum curves that arise in a simple order parameter-based model of a tricritical system. To be specific, the intersection of the recursion curves with the 45° line correspond with the intersection of the curves for $d\mathcal{F}(\psi)/d\psi$ with the abscissa, as shown in Figs. 3.32 and 3.34 in Appendix 3.D, which reviews the classical order parameter based model of a tricritical point.

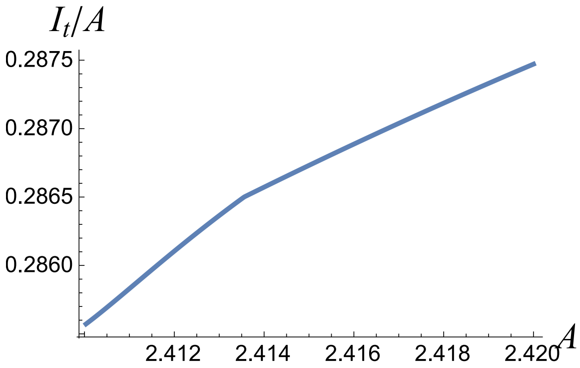

FIGURE 3.20: COMPLIANCE IN CONTINUOUS TRANSITION (ZOOMED IN NEAR TRANSITION)
The total compliance, I_t/A, in the immediate vicinity of the continuous transition from Region 1 to Region 3 in the dynamical phase diagram.

3.6 On the effects of inertia

3.6.1 Existence of dynamical fixed point when including inertial

So far we have ignored any effects of inertia on the response of the system. In light of the unexpected nature of the over-damped response and the typically significant effects of inertia, including resonant behavior, it is worthwhile to ask whether the dynamical transitions observed in the absence of inertia survive its introduction into the equations of motion. To this end, we have performed preliminary studies of an extension of Eq. (3.2.1) that incorporates an inertial term. The new equation of motion is

$$m\frac{d^2x(t)}{dt^2} + \gamma\frac{dx(t)}{dt} = F(x(t)) + A\sin(\omega t)\,, \tag{3.6.1}$$

which can be rewritten as

$$\frac{dx(t)}{dt} = \frac{p(t)}{m} \tag{3.6.2}$$

$$\frac{dp(t)}{dt} = -\gamma x(t) + F(x(t)) + A\sin(\omega t) \tag{3.6.3}$$

The search for steady state solutions to the above equation of motion can be formulated in terms of a pair of recursion relations. That is, on the basis of Eqs. (3.6.2) and (3.6.3) we can construct a map from $x_0 = x(0)$ and $p_0 = p(0)$ to $x_1 = x(2\pi/\omega)$ and $p_1 = p(2\pi/\omega)$. The map takes the form

$$x_1 = X(x_0, p_0) \tag{3.6.4}$$

$$p_1 = P(x_0, p_0) \tag{3.6.5}$$

Steady state solutions to the equation of motion are x_f and p_f, where

$$x_f = X(x_f, p_f) \tag{3.6.6}$$

$$p_f = P(x_f, p_f) \tag{3.6.7}$$

Taken separately each of the relations above generates a curve in the (x_f, p_f) plane. Figure 3.21 displays two such curves. The point at which the two curves intersect corresponds to a simultaneous solution of Eqs. (3.6.6) and (3.6.7) and thus a steady state solution of Eqs. (3.6.2) and (3.6.3). The solution $x(t)$ arising from that intersection, which corresponds

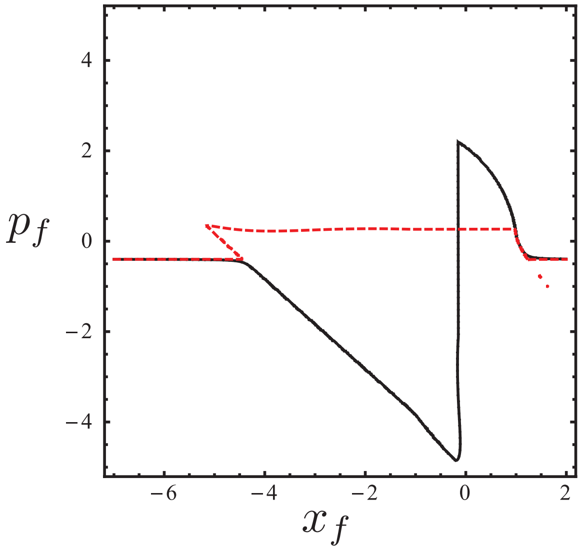

Figure 3.21: Contour plot of constant positions and momentum (single intersection)
A curve corresponding to Eq. (3.6.6) (solid curve) and Eq. (3.6.7) (dashed curve). In this case, we have taken $k = 2$, $\gamma = 1$, $\alpha = 0.01$ in the expression for the restoring force (see Appendix 3.A) and the force outside the Hookean region, $F_0 = 0$. The effective mass is $m = 1$, and the drive amplitude, $A = 1.82$.

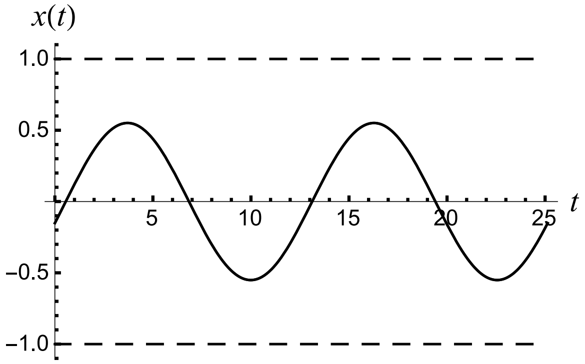

FIGURE 3.22: SOLUTION OF INTERSECTION IN FIG. 3.21

The solutions, $x(t)$, corresponding to the point of intersection in Fig. 3.21. The response is entirely inside the regime in which the restoring force is Hookean.

to a relatively weak driving force, is displayed in Fig. 3.22. Also shown in that figure are the nominal limits of the harmonic restoring force, at $x = \pm 1$.

By contrast, when the amplitude of the drive increases, more than one solution to the fixed point equations Eqs. (3.6.6) and (3.6.7)) appear, as shown in Fig. 3.23.

The curves for $x(t)$ corresponding to the three intersections are shown in Fig. 3.24. The relationship between the two skewed solutions is the same as the relationship between "mirror image" solutions established for solutions to Eq. (3.2.1) in Appendix 3.B. In fact, the argument in Appendix 3.B is easily extended to incorporate the inertial term in the equation of motion Eq. (3.6.1).

The question of the stability of the solutions of Eqs. (3.6.6) and (3.6.7) can be addressed in a straightforward manner. Imagine that x_F and p_F are such simultaneous solutions. Then, if $x_0 = x_F + \Delta x$ and $p_0 = p_F + \Delta p$,

$$\begin{aligned} x_1 &= x_F + \Delta x' \\ &= X(x_F + \Delta x, p_F + \Delta p) \\ &= x_F + X_x \Delta x + X_p \Delta p \end{aligned} \tag{3.6.8}$$

$$\begin{aligned} p_1 &= p_F + \Delta p' \\ &= p_F + P_x \Delta x + P_p \Delta p \end{aligned} \tag{3.6.9}$$

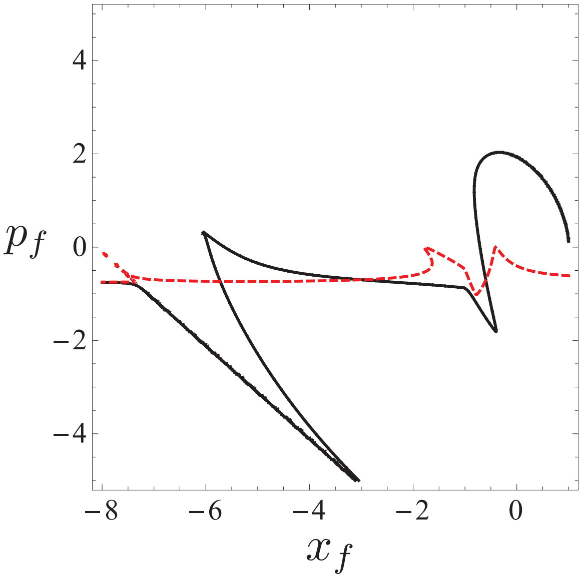

Figure 3.23: CONTOUR PLOT OF CONSTANT POSITIONS AND MOMENTUM (THREE INTERSECTIONS)
Another pair of curves corresponding to Eq. (3.6.6) (solid curve) and Eq. (3.6.7) (dashed curve). In this case the parameters in the equation of motion (Eq. (3.6.1)) are the same as in Fig. 3.21, except for the drive amplitude, A, which is now 1.87. Note the presence of three intersections of the two curves.

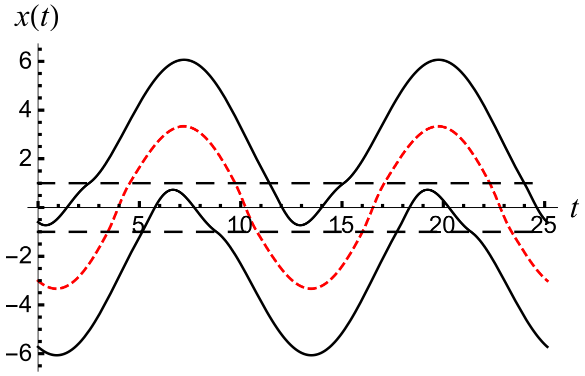

.

Figure 3.24: SOLUTION OF INTERSECTION IN FIG. 3.23
The three solutions corresponding to the intersections in Fig. 3.23. The two solid curves are the two stable, skewed solutions to the equation of motion (Eq. (3.6.1)), while the dashed curve is a symmetric and unstable solution to that equation. The horizontal lines indicate the limit of the region in which the restoring force is Hookean.

or

$$\begin{pmatrix} \Delta x' \\ \Delta p' \end{pmatrix} = \begin{pmatrix} X_x & X_p \\ P_x & P_p \end{pmatrix} \begin{pmatrix} \Delta x \\ \Delta p \end{pmatrix} \tag{3.6.10}$$

from which we infer that the stability of the solutions is controlled by the eigenvalues of the matrix on the right hand side of Eq. (3.6.10). If both have absolute value less than 1, the fixed point at x_F, y_F is stable; otherwise it is unstable. It is possible to determine the elements of the matrix numerically by exploring the recursion relations in the vicinity of the fixed point. Using this analysis, we find that the single intersection shown in Fig. 3.21 is stable and that the intersections on the far right and far left of Fig. 3.23 also represent dynamically stable solutions to the simultaneous equations Eqs. (3.6.6) and (3.6.7) – while the central intersection, which gives rise to the steady state solution shown dashed in Fig. 3.24, corresponds to a dynamically unstable solution to the equation of motion (Eq. (3.6.1)).

An alternate approach to the stability analysis of the steady state solutions to Eq. (3.6.1) is described in Appendix 3.E.

3.6.2 Limits cycles and subharmonic response

The above results strongly indicate the the types of dynamical transitions that we find when inertia is neglected are also to be expected in a system that manifests inertia. A more comprehensive exploration of the nature of viscoelastic behavior in such systems, including the range of dynamical transitions that one may encounter, remains to be undertaken.

3.7 Noise

3.7.1 Langevin equation approach

As noted in the introduction our original motivation was a series of experiments on the mechanical properties of a driven natively folded protein in solution at room temperature. Clearly this is a noisy environment, and it behooves us to examine which features we have uncovered survive the introduction of fluctuations, thermal and otherwise. In this section we briefly and qualitatively consider some of the modifications that arise when noise is introduced into the over-damped equation of motion, Eq. (3.2.1). For a specific example, we take the nonlinear restoring force to be the one defined in Appendix 3.A, with $F_0 = 0, \alpha = 0.01$. The restoring force is linear in displacement for $|x|$ less then about unity, decaying to zero restoring force outside that interval, as sketched in Fig. 3.2 with $F_0 = 0$.

With noise the dynamical equation is

$$\frac{dx(t)}{dt} = \frac{1}{\gamma}[-V'(x(t)) + A\sin(\omega t)] + \eta(t) \tag{3.7.1}$$

where $\eta(t)$ is a Gaussian random variable, corresponding to white noise, with correlator

$$\langle \eta(t)\eta(t')\rangle = \Gamma\delta(t-t') \tag{3.7.2}$$

We do not assume a fluctuation-dissipation relation and take γ and Γ as independent parameters.

A simple Euler forward integration leads to

$$x(t+\delta t) = x(t) + \frac{\delta t}{\gamma}[-V'(x(t)) + A\sin(\omega t)] + \sqrt{\Gamma\delta t}\, y_i \tag{3.7.3}$$

where y_i is a Gaussian random variable with zero mean and unit standard deviation. As an example, we choose parameters for which the noise-free system has a first-order transition from a “phase" at sufficiently low driving amplitude A in which there is a single, stable steady state, which is symmetric, to a phase (probably not physically reachable, occupying a tiny region of parameter space) at higher driving amplitude with three stable solutions, one symmetric and a pair of skewed solutions and, finally, at even higher amplitude drive to a phase in which only the skewed solutions are stable. For reference, for the parameters we choose, the noise-free dynamical transition occurs with amplitude about $A \simeq 1.89$. A realization of the three-solution situation with added noise is shown for $A = 1.89$ in Fig. 3.25.

The noise level $\Gamma = 10^{-4}$ has been chosen so that the noise-driven switching between the stable solutions is apparent. The nature of the switching will be considered in future work.

FIGURE 3.25: SAMPLE REALIZATION FOR STOCHASTIC MOTION

One realization of the solution to the stochastic equation Eq. (3.7.1) when the noise- free system is in the vicinity of a first-order dynamical phase transition from a phase with a single symmetric solution to a phase with three stable (noise free) steady state solutions, one symmetric about $x = 0$ and a pair of skewed solutions. The restoring force is provided in Appendix 3.A with $\alpha = 0.01, k = 2, F_0 = 0$. Other parameters: drive amplitude, $A = 1.89$, frequency, $\omega = 0.5$, noise correlator, $\Gamma = 0.0001$.

With this level of noise, the single symmetric solution below the transition is unremarkable and not shown.

For modest levels of noise, such as those considered above, qualitatively one expects the sharp noise-free transitions to be rounded, but to retain hints of the underlying noise-free transitions. This is, in fact realized. However, the calculation turns out to be more straightforwardly carried out in the context of the Fokker-Planck equation, to which we turn now.

3.7.2 Master equation

The dynamical equation with noise, Eq. (3.7.1) is Markovian, of the form $\dot{x} = h(x,t) + \eta(t)$, where, as above, $\eta(t)$ is delta-correlated with *constant* Γ, and $h(x,t)$ contains the “systematic" restoring force and the time- dependent driving force. As shown, e.g., in [152], one can reformulate the analysis of this equation into a probability distribution, $P(x,t)$, of an ensemble of solutions to the noisy equation of motion. This distribution is governed by the Fokker-

Planck equation,

$$\frac{\partial}{\partial t}P(x,t) = -\frac{\partial}{\partial x}D^{(1)}(x,t)P(x,t) + \left(\frac{\partial}{\partial x}\right)^2 D^{(2)}(x,t)P(x,t) \tag{3.7.4}$$

$$D^{(1)}(x,t) = h(x,t) \tag{3.7.5}$$

$$D^{(2)}(x,t) = \Gamma/2 \tag{3.7.6}$$

In our case, the quantity $h(x,t)$ is the driving force $F(x(t)) + A\sin(\omega t)$. As an example of the utilization of this equation, we apply it to the case of a discontinuous transition described in Sec. 3.5. Initially, we take $\Gamma = 0.2$, with the amplitude, A equal to 2.7.

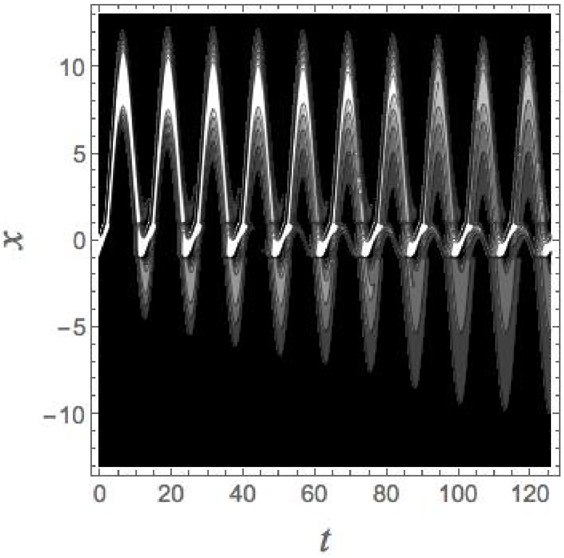

FIGURE 3.26: EVOLUTION OF $P(x,t)$ (10 PERIODS)

The probability distribution, $P(x,t)$ as given by the solution of the Fokker-Planck equation (Eqs. (3.7.4)–(3.7.6)), with $A = 2.7$, $\omega = 0.5$, $k = 2$, $F_0 = 0$ and $\Gamma = 0.2$. Ten periods of the driving force are shown. Lighter colors correspond to higher values of $P(x,t)$. The distribution at $t = 0$ was chosen to center on one of the dynamically stable skewed solutions to the deterministic equation of motion.

At this amplitude there are two stable skewed solutions and one unstable symmetric solution. The initial distribution was chosen to center on one of the skewed solutions. As illustrated in Fig. 3.26 the distribution evolves toward one that is symmetric. That is, both skewed solutions are equally represented in the steady state distribution. In fact, one can readily demonstrate that if $P(x,t)$ is a solution to Eqs. (3.7.4)–(3.7.6), then so is $P(-x, t+\pi/\omega)$. In Fig. 3.27, we show the steady state distribution for one period, along with the two stable skewed solutions and the unstable symmetric solution for zero noise.

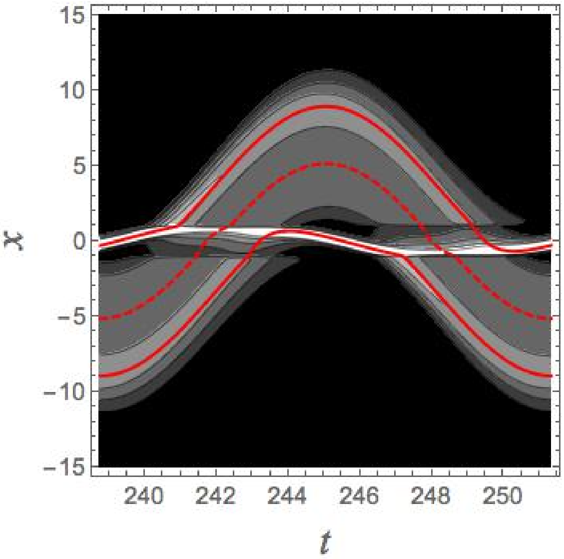

FIGURE 3.27: EVOLUTION OF $P(x,t)$ (SINGLE PERIODS)

One period (the twentieth) of the probability distribution, $P(x,t)$ as given by the solution of the Fokker-Planck equation (Eqs. (3.7.4)–(3.7.6)), with $A = 2.7$, $\omega = 0.5$, $k = 2$, $F_0 = 0$ and $\Gamma = 0.2$. Also shown are the two stable skewed solutions (solid red curves) and the unstable symmetric solution (dashed red curve). Lighter colors correspond to higher values of $P(x,t)$.

3.7.3 Compliances in the presence of noise

Making use of the steady state probability distribution, one can calculate the effect of noise on compliances. Figure 3.28, displays the results for the compliances in the case in which the parameters in the noise-free equation of motion are such that Eq. (3.2.1)) predicts a first-order transition from a dynamically stable symmetric solution to stable skewed solutions. In this calculation, Γ is taken to be 0.014—significantly higher values of this quantity lead to a washing out of evidence of a dynamical transition. Here the compliances are defined as in Sec. 3.4, with $x(t)$ replaced by $\langle x(t)\rangle$, the average being taken with respect to the distribution function $P(x,t)$, i.e. $\langle x(t)\rangle = \int_{-\infty}^{\infty} x' P(x',t)dx'$. The plot in Fig. 3.28 is to be compared

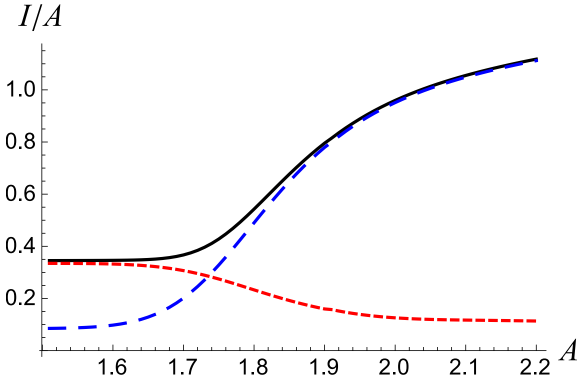

Figure 3.28: Total compliance with noise

The total compliance I_t/A (solid black curve), the dissipative compliance, I_d/A (long-dashed blue curve) and the storage compliance, I_s/A (dashed red curve). Here $k = 2$, $\omega = 0.5$, $F_0 = 0$ and $\Gamma = 0.014$.

with Fig. 3.16, the plot of compliances in the absence of noise. In the presence of noise the transition from an elastic to a viscous response regime no longer displays a first-order discontinuity.

3.8 Concluding remarks

The investigations of Zocchi *et al.* [137–139, 153] of the response of a folded protein to a sinusoidal driving force point to a description in terms of a single collective coordinate. Moreover, the response appears to be quantifiable in terms of a viscoelastic formalism, with the additional feature of a sharp transition from dominantly elastic response at low amplitude drive to mainly viscous response at high drive amplitude. We find that a simple model exhibits behavior consistent with those observations. From such analysis we conclude that the combination of experimental findings and characterization in terms of a simple model by Zocchi et al. forms a promising basis for a comprehensive description of the gross mechanical and dynamical properties of a class of folded proteins. Furthermore, we strongly believe that it ought to be useful in further investigations, both experimental and theoretical of those properties.

Extensions of the present study should aid in the development of insights into the structural properties of proteins, both in isolation and as components of larger systems. For example, it would be interesting to expand the characterization of a protein configuration beyond a single collective variable, to take into account internal adjustments to external influences. Given the size and complexity of those molecules the number of mechanical degrees of freedom will be considerable. However, judicious analysis should allow the investigator to expand the set of dynamical variables to a manageable size. Additionally, the effects of inertia, while small, are almost certainly non-negligible, and the effects of noise deserve fuller attention.

The existence of a dynamical phase transition in the simple model studied here deserves note in and of itself, and the genesis of this transition merits further study. It would be of great interest to identify the essential characteristics of a nonlinear system that lead to this phenomenon. As regards symmetry breaking, a crucial aspect of the model is the existence of a symmetry in the underlying equation of motion, in particular the fact that the restoring force, $F(x)$ satisfies $F(-x) = -F(x)$; a similar symmetry is present in the Suzuki-Kubo model [143, 144]. However, the protein conformation is almost certainly not consistent with such a force, given that the collective co-ordinate x will have one sign—say positive—when the protein is stretched and the opposite sign when it is compressed. It is entirely reasonable to expect that the "cracking" process, in which a linear restoring force is replaced by another relationship between that force and the relative displacements in the protein, will differ in those two regimes, which means that there is no symmetry to break. Nevertheless, as shown in Appendix 3.F, even in the absence of such intrinsic asymmetry, the equation of motion can nevertheless lead to the kind of dynamical transition discussed in this paper. Thus, there are good reasons to expect that the response observed by Zocchi and co-workers does indeed arise from a true dynamical phase transition.

Appendix 3.A The nonlinear restoring force

The form for the restoring force derives from the function

$$\Delta(x,\alpha) = \frac{1}{\pi}\frac{\alpha}{x^2+\alpha^2} \tag{3.A.1}$$

In the limit $\alpha = 0$, this is just the Dirac delta function. Two functions that result from integrating this function once and then twice are

$$f_1(x,\alpha) = \frac{2\tan^{-1}(x/\alpha)}{\pi} \tag{3.A.2}$$

$$f_2(x,\alpha) = \frac{2\left(x\tan^{-1}(x/\alpha) - \frac{1}{2}\alpha\ln\left(\alpha^2+x^2\right)\right)}{\pi} \tag{3.A.3}$$

Then, with coefficients

$$A = -\frac{2\alpha F_0 - \pi k(1+\alpha^2)}{4\left((1+\alpha^2)\tan^{-1}(1/\alpha) - \alpha\right)} - \frac{F_0}{2} \tag{3.A.4}$$

$$B = -\frac{2\alpha F_0 - \pi k(1+\alpha^2)}{4\left((1+\alpha^2)\tan^{-1}(1/\alpha) - \alpha\right)} \tag{3.A.5}$$

The function

$$\begin{aligned} &A\left(f_1(x+1,\alpha) + f_1(x-1,\alpha)\right) \\ &\qquad + B\left(f_2(x-1,\alpha) - f_2(x+1,\alpha)\right) \end{aligned} \tag{3.A.6}$$

has the form shown in Fig. 3.2, with slope $-k$ at the origin and asymptotes of $\pm F_0$. The parameter α determines the sharpness of the transition from a linear restoring force to a restoring force that is constant. This cumbersome expression for the restoring force enables independent variation of the features controlled by α and F_0. Figure 3.29 displays three instances of the kind of restoring force that we explore.

In the body of the paper we have taken the transition from Hookean behavior to occur around $|x| = 1$.

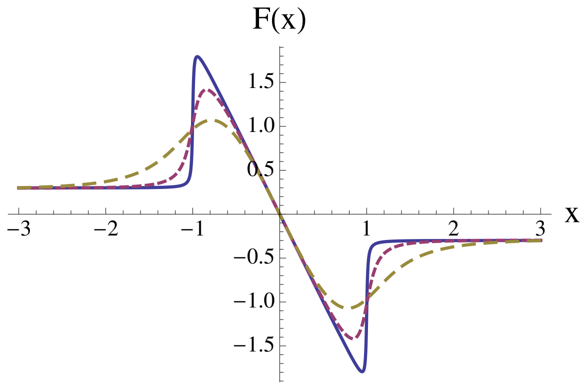

Figure 3.29: Example of the restoring force

Three instances of restoring forces arising from Eq. (3.A.6). In all cases, the absolute value of the slope of the curve at $x = 0$ is $k = 2$, and the absolute value of the asymptote is $F_0 = 0.3$. The parameter α controlling the transition between the central and outer region is 0.01 for the solid curve, 0.1 for the short-dashed curve and 0.5 for the long-dashed curve. The restoring force changes from Hookean to constant near $x = \pm 1$.

Appendix 3.B Pairs of skewed solutions

The form of the equation of motion, (Eq. (3.2.1)) and the symmetry of the restoring force,

$$F(x) = -F(-x) \tag{3.B.1}$$

allow one to generate, from a solution $x(t)$, a "mirror image" solution equal to $-x(t + \pi/\omega)$. To see this, replace t by $t + \pi/\omega$ in Eq. (3.2.1), which leads to

$$\begin{aligned}\frac{dx(t+\pi/\omega)}{dt} &= \frac{1}{\gamma}\left[F(x(t+\pi/\omega)) + A\sin(\omega(t+\pi/\omega))\right] \\ &= \frac{1}{\gamma}\left[-F(-x(t+\pi/\omega)) - A\sin(\omega t)\right] \end{aligned} \tag{3.B.2}$$

If we now multiply both sides of the resulting equation by -1, we end up with the result that $-x(t + \pi/\omega)$ satisfies the same equation as $x(t)$. This allows one to generate, from any skewed solution, a second one, skewed in the opposite direction. By contrast, a symmetric solution will reproduce itself under this transformation.

Appendix 3.C Stability analysis for solutions to the equation of motion in Sec. 3.3

To assess the stability of a solution of the equation of motion when the restoring force exhibits a sharp break between Hooke's Law and vanishing amplitude as in Eq. (3.3.1), we perturb that equation as follows. Assume a solution, $x_0(t)$, to Eq. (3.2.1). Then, write $x(t) = x_0(t) + \delta x(t)$. At first-order in the perturbation $\delta x(t)$, the equation becomes

$$\frac{d\delta x(t)}{dt} = \frac{1}{\gamma}\left[\delta x(t) F'(x_0(t))\right] \tag{3.C.1}$$

Dividing both sides of Eq. (3.C.1) by $\delta x(t)$ and integrating over a period of the drive, we find

$$\ln\left(\frac{\delta x(t+2\pi/\omega)}{\delta x(t)}\right) = \frac{1}{\gamma}\int_t^{t+2\pi/\omega} F'(x_0(t))dt \tag{3.C.2}$$

or

$$\frac{\delta x(t+2\pi/\omega)}{\delta x(t)} = \exp\left[\frac{1}{\gamma}\int_t^{t+2\pi/\omega} F'(x_0(t))dt\right] \tag{3.C.3}$$

Figure 3.30 shows a restoring force that changes abruptly from Hookean to vanishing, along with its derivative.

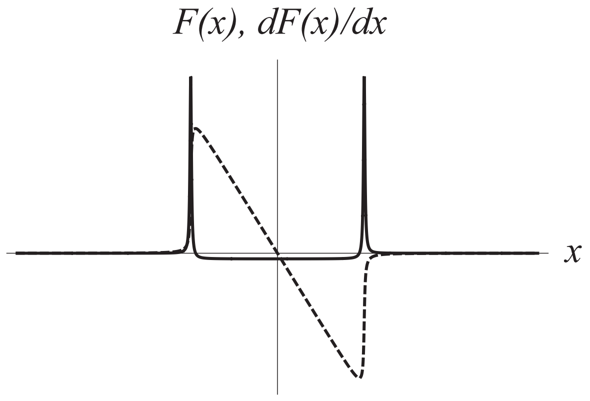

Figure 3.30: Restoring force and its derivative

Restoring force with a rapid transition between Hooke's law in a region about the origin (dashed curve) along with its derivative (solid curve). When the transition is perfectly abrupt the peaks in the force derivative become Dirac delta functions.

In the limit of a discontinuous transition, the peaks in the derivative become Dirac delta functions. If we are interested in the skewed solutions described in Sec. 3.3, then the integral on the right hand side of Eqs. (3.C.2) and (3.C.3) yields three contributions. The first is from the interior region and will be equal to $-k$ multiplied by the amount of time that $x(t) < x_0$, which, according to Eq. (3.3.4), is $2\pi/\omega - 2t_0$. Then there is the result of integrating through the very narrow peaks in the derivative. Here, we write

$$\begin{aligned} \int F'(x_0(t))dt &= \int \frac{F'(x_0(t))}{dx_0(t)/dt} dx_0(t) \\ &= \int \frac{F'(x)}{F(x) \pm A\sin(\omega t_0)} dx \\ &\to \pm \ln \left[\frac{A\sin(\omega t_0)}{A\sin(\omega t_0) \mp kx_0} \right] \end{aligned} \tag{3.C.4}$$

The upper sign on the right hand side of Eq. (3.C.4) applies in the case that the trajectory through the peak in the derivative is out of the inner region and the lower sign applies when the trajectory is into the inner region. The time, t has been set equal to t_0, as passage through the peaks occurs in effectively a single instant of time. Assembling the two contributions we fnd for the right hand side of Eq. (3.C.3)

$$\exp\left[-\frac{k}{\gamma}\left(\frac{2\pi}{\omega} - 2t_0 \right) + \frac{1}{\gamma} \ln \left(\frac{(A\sin(\omega t_0))^2}{(A\sin(\omega t_0))^2 - (kx_0)^2} \right) \right] \tag{3.C.5}$$

If the expression in square brackets is real and negative then perturbations to the trajectory $x_0(t)$ die off, and the periodic solution to the equation of motion is stable. If it is positive, then those perturbations grow exponentially, and the solution is unstable. If the expression is imaginary, then the assumption of a solution is incorrect, in that the velocity at one of the transitions between Hooke's law force and no restoring force has the wrong sign. We find that in the case of graphical solutions to Eq. (3.3.8) that are not equal to π/ω, the one with a smaller value of t_0 does not correspond to an actual trajectory, and the one with the larger value of t_0 corresponds to a dynamically stable solution to the equation of motion.

Appendix 3.D Review of the statistical mechanics of tricriticality

According to the canonical model of tricritical points based on an order parameter, the thermodynamic behavior of a system near a symmetry breaking phase transition is governed by a free energy of the form

$$\mathcal{F}(\psi) = \mathcal{F}_0 + Ct\psi^2 + u\psi^4 + v\psi^6 \tag{3.D.1}$$

Here, ψ is the order parameter and t is a reduced temperature, proportional to the difference between the actual temperature of the system and a critical temperature. The coefficients $C > 0$, u and v are assumed to be insensitive to the temperature as long as t is sufficiently small. Thermodynamic stability requires $v > 0$; otherwise, the free energy takes on unbounded negative values as $|\psi|$ increases. The system described by this free energy settles into the state of lowest free energy, determined by minimizing $\mathcal{F}(\psi)$. The results of this minimizing procedure depend qualitatively on the sign of the coefficient u. When u is positive, the ψ-dependence of $\mathcal{F}$ is as shown in Fig. 3.31. As shown in the figure, when $t > 0$, the unique minimum of the free energy is at $\psi = 0$. On the other hand, when $t < 0$, there are two minima, spaced equidistant from $\psi = 0$. The minimum at $\psi = 0$ has become a free energy maximum.

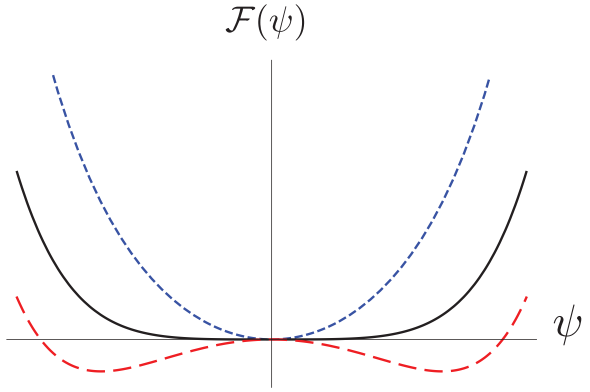

FIGURE 3.31: FREE ENERGY OF TRICRITICAL SYSTEM NEAR CONTINUOUS TRANSITION

Behavior of the free energy $\mathcal{F}(\psi)$ in Eq. (3.D.1) when the coefficients u and v are positive. The blue, dashed curve is the free energy when $t > 0$. The red, long- dashed, curve is the free energy when $t < 0$. The solid black curve is $\mathcal{F}(\psi)$ at the transition point, when $t = 0$.

In mechanics, that maximum would correspond to a point of unstable equilibrium, in contrast to the minima, which represent points of stable equilibrium. However, a thermodynamic system will inevitably fluctuate away from such a state. Because the free energy is even in ψ, in that $\mathcal{F}(-\psi) = \mathcal{F}(\psi)$, each of the minima for $t < 0$, which lies to one side or the other of the origin, represents a violation of the symmetry of the physics underlying the system's thermodynamics, and the transition that occurs as t passes through zero is called a *symmetry breaking* phase transition. The determination of the minima follows from the solution of the equation

$$\frac{d\mathcal{F}(\psi)}{d\psi} = 0 \tag{3.D.2}$$

On the other hand, when $u < 0$, the behavior of $\mathcal{F}(\psi)$ is shown in Fig. 3.32.

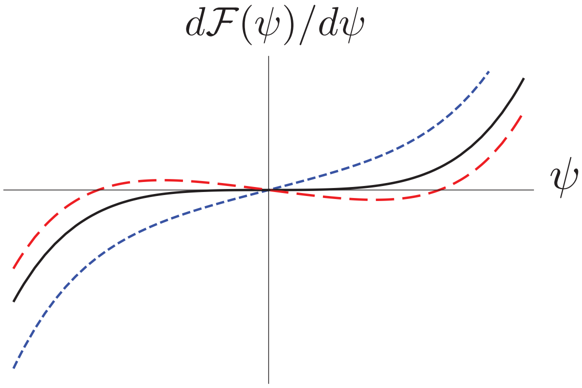

Figure 3.32: Derivative of free energy in tricritical system near continuous transition The graphical representation of $d\mathcal{F}(\psi)/d\psi$. The curves follow the format of Fig. 3.31.

In this case, the minima at non-zero values of ψ develop while there is still a free energy minimum at $\psi = 0$. As that occurs two free energy maxima appear between the new minima and the free energy minimum at $\psi = 0$. Eventually, at low enough temperatures, the only minima are at finite ψ, with one free energy maximum at $\psi = 0$. Free energies and the related curves for the free energy derivative are displayed in Figs. 3.33 and 3.34. Focusing on the curves in Fig. 3.34, we see that at high enough temperatures, there is only one value of ψ at which $d\mathcal{F}(\psi)/d\psi$ passes through zero: $\psi = 0$. As the temperature is lowered additional zeros appear, first four, two on each side of the origin, corresponding to a maximum and then a

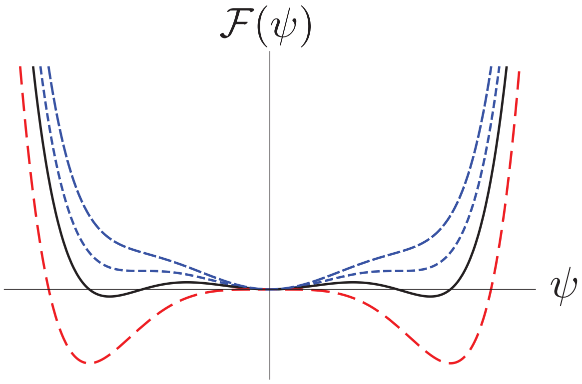

FIGURE 3.33: FREE ENERGY OF TRICRITICAL SYSTEM NEAR FIRST-ORDER TRANSITION

Curves for $\mathcal{F}(\psi)$ when the fourth order coefficient u is negative. At high enough temperatures (blue long dashed curve) there is one free energy minimum, at $\psi = 0$. As the temperature is lowered, two other minima emerge (blue dashed curve and solid black curve). In addition, two maxima that separate the minimum at $\psi = 0$ and the flanking minima appear. At low enough temperatures the two minima at non-zero ψ remain, the central extremum in the free energy having become a maximum (red long-dashed curve).

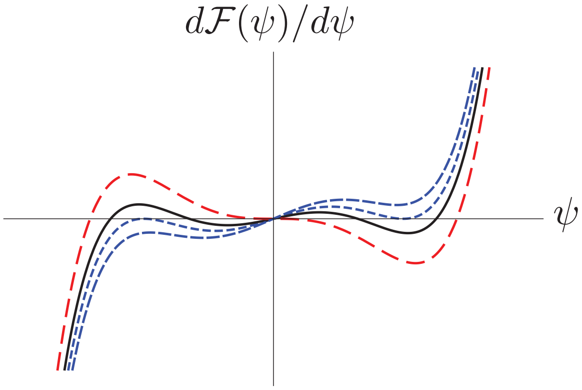

FIGURE 3.34: DERIVATIVE OF FREE ENERGY IN TRICRITICAL SYSTEM NEAR FIRST-ORDER TRANSITION

Curves for $d\mathcal{F}(\psi)/d\psi$ corresponding to the curves shown in Fig. 3.31. These curves pass through zero at extrema—maxima and minima—of $\mathcal{F}(\psi)$. They are formatted in the same way as the free energy curves in Fig. 3.33.

minimum in $\mathcal{F}(\psi)$. At even lower temperatures, only three zeros remain, corresponding to minima at non- zero values of ψ, while the zero at $\psi = 0$ refers to a free energy maximum at that point.

Appendix 3.E Alternate stability analysis of steady state solutions to (3.6.1)

As an alternate approach to the stability analysis of steady state solutions to Eq. (3.6.1), obtained by determining simultaneous solutions to Eq. (3.6.6) and Eq. (3.6.7), we return to the original equation Eq. (3.6.1) and expand about periodic solution, $x_0(t)$. That is, write $x(t) = x_0(t) + \delta x(t)$. The equation satisfied by $\delta x(t)$ is

$$\frac{d^2\delta x(t)}{dt^2} + \gamma \frac{d\delta x(t)}{dt} = F'(x_0(t))\delta x(t) \tag{3.E.1}$$

Then, we write $\delta x(t) = \psi(t)e^{-\gamma t/2}$. The equation for $\psi(t)$ is

$$\frac{d^2\psi(t)}{dt^2} - \left(\frac{\gamma}{2}\right)^2 \psi(t) = F'(x_0(t))\psi(t) \tag{3.E.2}$$

Because of the periodicity of $x_0(t)$, this is just like the Schrödinger equation of a particle in a periodic potential. The periodicity is that of the driving force. We can now treat this as a problem in one dimensional band theory [154]. We start with a solution of the above equation, $\psi_1(t)$ that has the initial conditions

$$\psi_1(0) = 1 \tag{3.E.3}$$

$$\psi_1'(0) = 0 \tag{3.E.4}$$

and a function $\psi_2(t)$ satisfying

$$\psi_2(0) = 0 \tag{3.E.5}$$

$$\psi_2'(0) = 1 \tag{3.E.6}$$

A general solution will be a linear combination of $\psi_1(t)$ and $\psi_2(t)$, where the coefficients are determined, for example, by the value of the solution and the value of its derivative at $t = 0$.

If we write

$$\psi(t) = A\psi_1(t) + B\psi_2(t) \tag{3.E.7}$$

Then,

$$A = \psi(0) \tag{3.E.8}$$

$$B = \psi'(0) \tag{3.E.9}$$

After one full period, the magnitude and derivative of the solution is given by

$$A' = A\psi_1(2\pi/\omega) + B\psi_2(2\pi/\omega) \tag{3.E.10}$$

$$B' = A\psi_1'(2\pi/\omega) + B\psi_1'(2\pi/\omega) \tag{3.E.11}$$

This gives rise to the map

$$\begin{pmatrix} A' \\ B' \end{pmatrix} = \begin{pmatrix} \psi_1(2\pi/\omega) & \psi_1(2\pi/\omega) \\ \psi_1'(2\pi/\omega) & \psi_2'(2\pi/\omega) \end{pmatrix} \begin{pmatrix} A \\ B \end{pmatrix} \tag{3.E.12}$$

We know from the invariance of the Wronskian and from its value at $t = 0$ that

$$\psi_1(t)\psi_1'(t) - \psi_1'(t)\psi_2(t) = 1 \tag{3.E.13}$$

for all t. This means that the determinant of the matrix in Eq. (3.E.12) is equal to one.

Given that the relationship Eq. (3.E.12) holds for the values of A and B for each succeeding period, the ultimate behavior of the solution is going to be determined by the eigenvalues of the matrix on the right hand side of that equation. In light of the relationship between $\delta x(t)$ and $\psi(t)$, we see that the stability of the solution is going to be determined by the exponential $e^{-\gamma\pi/\omega}$ and the eigenvalues. Specifically, by the product

$$\begin{aligned} &e^{-\gamma\pi/\omega}\frac{1}{2}\Big[\psi_1(2\pi/\omega) + \psi_2'(2\pi/\omega) \\ &\qquad \pm \sqrt{(\psi_1(2\pi/\omega) + \psi_2'(2\pi/\omega))^2 - 4}\Big] \end{aligned} \tag{3.E.14}$$

If the absolute value of Eq. (3.E.14) is less than one, for both signs in the expression, then the solution is stable, and if that is not the case the solution is unstable. The result in

Eq. (3.E.14) follows in part from the fact that the determinant of the matrix in Eq. (3.E.12) is equal to one.

Making use of the above method, we arrive at the same conclusions regarding the steady state solutions to the equation of motion (Eq. (3.6.1)) shown in Sec. 3.6.

Appendix 3.F Dynamical transition when the force is inherently asymmetric

We have been considering a system in which the force, $F(x)$ that restores it to stable equilibrium in the absence of an external drive is symmetric in the dynamical variable that characterizes its distortion from that state in that $F(-x) = -F(x)$. It is natural to ask whether this symmetry in the equation of motion is essential to the existence of the dynamical transitions discussed here. As it turns out those transitions can also arise when the underlying symmetry is absent. Consider the restoring force shown in Fig. 3.35. As shown in that figure, the force is of the form $F = -kx$, with spring constant $k = 2$ for $x < 1$. Outside of that region the restoring force is equal to zero.

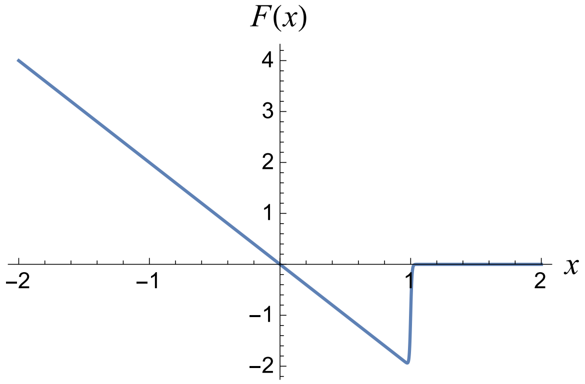

FIGURE 3.35: ASYMMETRIC RESTORING FORCE

A restoring force, $F(x)$ that is Hookean for all positive values of x but that reverts to zero at $x = -1$. The spring constant in the Hookean regime is $k = 2$.

In Fig. 3.36 we see the map from $x(0)$ to $x(2\pi/\omega)$, along with the 45° line for drive amplitude $A = 2.762$, frequency $\omega = 2$ and $\gamma = 1$ in the equation of motion (Eq. (3.2.1)).

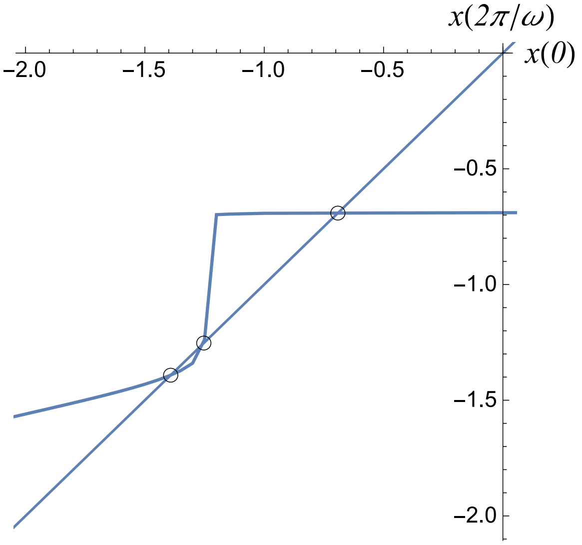

Figure 3.36: Example $x(0)$ $-x(2\pi/\omega)$ map in asymmetric case

The map from $x(0)$ to $x(2\pi/\omega)$ generated by the equation of motion (Eq. (3.2.1)) with the restoring force shown in Fig. 3.35 and $\omega = 2$, $\gamma = 1$ and $A = 2.762$. The points of intersection between the map and the 45° line, also shown, are indicated by small circles. The two outer intersections correspond to dynamically stable steady state solutions to the equation of motion, while the inner intersection corresponds to a dynamically unstable steady state solution.

This kind of map is consistent with the existence of two stable fixed points solutions and one unstable solutions; Fig. 3.37 shows those three solutions. This coexistence points to a dynamical transition identical to sharp transitions described in the body of this paper, the only difference being the absence of symmetry breaking, in that there is no underlying symmetry to violate.

As further evidence for the dynamical transition, Fig. 3.38 contains the maps for four different drive amplitudes in the same region plotted in Fig. 3.37. This plot is to be compared with the maps shown in Fig. 3.17. The parameters are as described in Fig. 3.36, except for the drive amplitudes, which range from $A = 2.755$ to $A = 2.78$. The discussion of the scenario corresponding to this figure parallels the corresponding commentary just above Fig. 3.17.

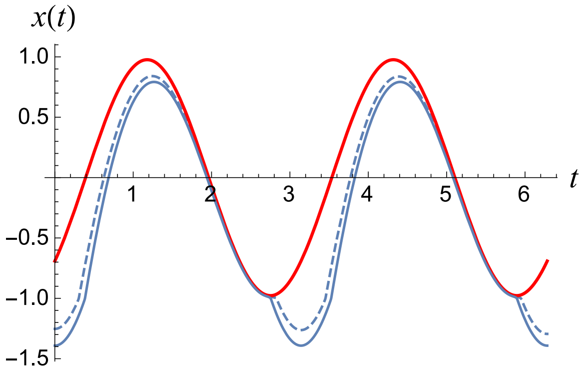

FIGURE 3.37: EXAMPLE TRAJECTORIES IN ASYMMETRIC CASE

The three steady state solutions to the equation of motion corresponding to the points of intersection in Fig. 3.36, plotted over two periods of the drive, $A\sin(\omega t)$. The thick red curve corresponds to a trajectory that lies entirely in the region in which the restoring force is linear. The thin blue curve is the stable solution that extends outside that region ($x < -1$), and the dashed curve is the dynamically unstable solution that separates the two stable solutions for $x(t)$.

The noteworthy results here are, first, that at the highest drive amplitude there is only one skewed steady state solution to the equation of motion instead of two and, second, that when there is more than one solution the two dynamically stable ones correspond to a symmetric solution and a single skewed solution, separated by an unstable steady state solution, as plotted in Fig. 3.37.

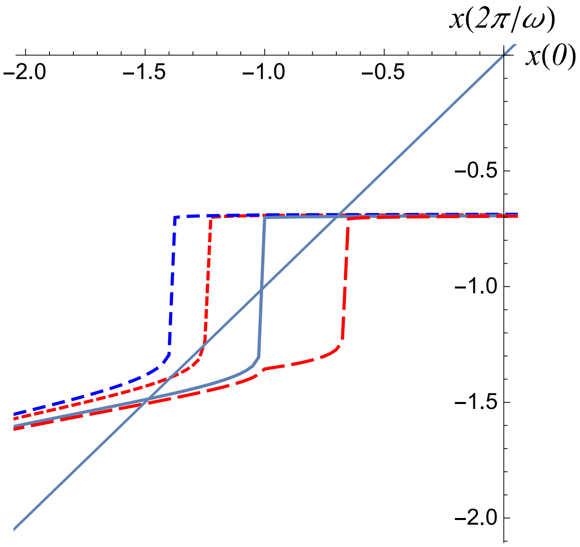

Figure 3.38: Example $x(0)$ $-x(2\pi/\omega)$ map throughout transition in asymmetric case Illustrating a first-order transition in the case in which the restoring force is as shown in Fig. 3.35. The parameters are as described in the caption to Fig. 3.36, except for the values of the drive amplitudes. Those amplitudes are 2.755 (intermediate dashed blue curve), 2.762 (short dashed red curve), 2.775 (solid black curve) and 2.78 (long dashed red curve). Note that there are no more than three steady state solutions to the equation of motion and that at the extremes there is only one steady state solution to the equation of motion (Eq. (3.2.1)), in contrast to the case of the symmetry breaking dynamical phase transition.

BIBLIOGRAPHY

[1] T. Zeng and L. Chen. “Tracing dynamic biological processes during phase transition.” In: *BMC Systems Biology* 6.Suppl 1 (2012), S23 (pages ii, 3).

[2] P. C. Davies, L. Demetrius, and J. a. Tuszynski. “Cancer as a dynamical phase transition.” In: *Theoretical Biology and Medical Modelling* 8.1 (2011), p. 30 (pages ii, 3).

[3] C. A. Fogle et al. “Shape transitions in soft spheres regulated by elasticity.” In: *Physical Review E - Statistical, Nonlinear, and Soft Matter Physics* 88.5 (July 2013). arXiv: `1306.5864` (page xi).

[4] C. A. Fogle, J. Rudnick, and D. Jasnow. “Protein viscoelastic dynamics: a model system.” Version 1. In: (Feb. 2015), pp. 1–19. arXiv: `cond-mat.soft/1502.00343v1 [cond-mat.soft]` (page xi).

[5] W. Helfrich. “Elastic properties of lipid bilayers: theory and possible experiments.” In: *Zeitschrift für Naturforschung. Teil C: Biochemie, Biophysik, Biologie, Virologie* 28.11 (1973), pp. 693–703 (pages 1, 17).

[6] P. G. De Gennes and C. Taupin. “Microemulsions and the flexibility of oil/water interfaces.” In: *The Journal of Physical Chemistry* 86.13 (1982), pp. 2294–2304 (page 1).

[7] D. R. Nelson and L. Peliti. “Fluctuations in Membranes with Crystalline and Hexatic Order.” In: *Journal de Physique* 48.7 (1987), pp. 1085–1092 (pages 1, 11).

[8] L. Peliti and S. Leibler. “Effects of thermal fluctuations on systems with small surface tension.” In: *Physical Review Letters* 54.15 (1985), pp. 1690–1693 (page 1).

[9] S. A. Safran. “Fluctuations of spherical microemulsions.” In: *The Journal of Chemical Physics* 78.4 (1983), pp. 2073–77 (page 1).

[10] M. B. Schneider, J. T. Jenkins, and W. W. Webb. “Thermal fluctuations of large quasi-spherical bimolecular phospholipid vesicles.” In: *Journal de Physique* 45.9 (1984), pp. 1457–1472 (page 1).

[11] M. B. Schneider, J. T. Jenkins, and W. W. Webb. “Thermal Fluctuations of Large Cylindrical Phospholipid Vesicles.” In: *Biophysical Journal* 45.5 (May 1984), pp. 891–899 (page 1).

[12] S. T. Milner and S. Safran. “Dynamical Fluctuations of Droplet Microemulsions and Vesicles.” In: *Physical Review A* 36.9 (Nov. 1987), pp. 4371–4379 (pages 1, 18, 19).

[13] S. Ljunggren and J. C. Eriksson. “Shape fluctuations of spherical micelles.” In: *Journal of the Chemical Society, Faraday Transactions 2* 80.4 (1984), p. 489 (page 1).

[14] P. J. Flory and J. Rehner. “Statistical Mechanics of Cross-Linked Polymer Networks II. Swelling.” In: *The Journal of Chemical Physics* 11.11 (1943), p. 521 (page 1).

[15] M. Hamedi et al. “Nanocellulose aerogels functionalized by rapid layer-by-layer assembly for high charge storage and beyond.” In: *Angewandte Chemie - International Edition* 52.46 (2013), pp. 12038–12042 (page 1).

[16] C. Primo-Martín et al. “The role of the gluten network in the crispness of bread crust.” In: *Journal of Cereal Science* 43.3 (2006), pp. 342–352 (page 1).

[17] A. S. Sivam et al. “Properties of bread dough with added fiber polysaccharides and phenolic antioxidants: A review.” In: *Journal of Food Science* 75.8 (2010) (page 1).

[18] J. A. Dunne. “The Network Structure of Food Webs.” In: *Structure* (2005), pp. 27–86 (page 1).

[19] K. S. Mikkonen et al. *Prospects of polysaccharide aerogels as modern advanced food materials.* 2013 (page 1).

[20] P. J. Flory and J. Rehner. “Statistical Mechanics of Cross-Linked Polymer Networks I. Rubberlike Elasticity.” In: *The Journal of Chemical Physics* 11.11 (1943), p. 512 (page 1).

[21] P. G. de Gennes. Scaling Concepts in Polymer Physics. Cornell University Press, 1979, p. 319 (page 1).

[22] P.-G. de Gennes. “Reptation of a Polymer Chain in the Presence of Fixed Obstacles.” In: *Journal of Chemical Physics* 55.2 (1971), pp. 572–579 (page 1).

[23] M. Rubinstein and S. Panyukov. “Elasticity of Polymer Networks.” In: *Macromolecules* 35.17 (Aug. 2002), pp. 6670–6686 (page 1).

[24] W. W. Graessley and L. J. Fetters. “Thermoelasticity of polymer networks.” In: *Macromolecules* 34.20 (2001), pp. 7147–7151 (page 1).

[25] G. Gurtner and M. Durand. “Structural Properties of Stiff Elastic Networks.” In: *Europhysics Letters* 87.2 (2008), pp. 1–5. arXiv: `0805.4712` (page 1).

[26] J. Wilhelm and E. Frey. “Elasticity of stiff polymer networks.” In: *Physical Review Letters* 91.10 (Sept. 2003), p. 108103. arXiv: `0303592 [cond-mat]` (page 1).

[27] A. Arabzade, H. Moharami, and A. Ayazi. *Local elastic buckling coefficients of steel plates in composite steel plate shear walls.* 2011 (page 1).

[28] S. H. Kang and Y. T. Im. “Three-dimensional thermo-elastic-plastic finite element modeling of quenching process of plain-carbon steel in couple with phase transformation.” In: *International Journal of Mechanical Sciences* 49.4 (2007), pp. 423–439 (page 1).

[29] M. Tane et al. “Elastic property of aged duplex stainless steel.” In: *Scripta Materialia* 48.3 (2003), pp. 229–234 (page 1).

[30] G. De Schutter. “Applicability of degree of hydration concept and maturity method for thermo-visco-elastic behaviour of early age concrete.” In: *Cement and Concrete Composites* 26.5 (2004), pp. 437–443 (page 1).

[31] F. Lydon and R. Balendran. *Some observations on elastic properties of plain concrete.* 1986 (page 1).

[32] S. Wen and D. D. L. Chung. “Uniaxial tension in carbon fiber reinforced cement, sensed by electrical resistivity measurement in longitudinal and transverse directions.” In: *Cement and Concrete Research* 30.8 (2000), pp. 1289–1294 (page 1).

[33] E. Totry et al. “Effect of fiber, matrix and interface properties on the in-plane shear deformation of carbon-fiber reinforced composites.” In: *Composites Science and Technology* 70.6 (2010), pp. 970–980 (page 1).

[34] C. O. Horgan and G. Saccomandi. “A new constitutive theory for fiber-reinforced incompressible nonlinearly elastic solids.” In: *Journal of the Mechanics and Physics of Solids* 53.9 (2005), pp. 1985–2015 (page 1).

[35] J.-P. Salvetat et al. *Elastic and Shear Moduli of Single-Walled Carbon Nanotube Ropes.* 1999 (page 1).

[36] J. P. Lu. “Elastic properties of carbon nanotubes and nanoropes.” In: *Physical Review Letters* 79.7 (1997), pp. 1297–1300 (page 1).

[37] I. Arias and M. Arroyo. “Size-dependent nonlinear elastic scaling of multiwalled carbon nanotubes.” In: *Physical Review Letters* 100.8 (2008) (page 1).

[38] G. Bao and S. Suresh. “Cell and molecular mechanics of biological materials.” In: *Nature materials* 2.11 (2003), pp. 715–725 (page 2).

[39] C. Guillot and T. Lecuit. “Mechanics of epithelial tissue homeostasis and morphogenesis.” In: *Science* 340.6137 (2013), pp. 1185–9 (page 2).

[40] D. E. Discher, P. Janmey, and Y.-L. Wang. “Tissue cells feel and respond to the stiffness of their substrate.” In: *Science* 310.5751 (2005), pp. 1139–1143 (page 2).

[41] S. Y. Tee et al. “Cell shape and substrate rigidity both regulate cell stiffness.” In: *Biophysical Journal* 100.5 (2011) (page 2).

[42] W. Xu et al. “Cell Stiffness Is a Biomarker of the Metastatic Potential of Ovarian Cancer Cells.” In: *PLoS ONE* 7.10 (2012) (page 2).

[43] J. Calbo et al. “A functional role for tumor cell heterogeneity in a mouse model of small cell lung cancer.” In: *Cancer Cell* 19.2 (Feb. 2011), pp. 244–56 (page 2).

[44] D. Irimia and M. Toner. “Spontaneous migration of cancer cells under conditions of mechanical confinement.” In: *Integrative Biology* 1.8-9 (), pp. 506–12 (page 2).

[45] S. E. Cross et al. “Nanomechanical analysis of cells from cancer patients.” In: *Nature Nanotechnology* 2.12 (Dec. 2007), pp. 780–3 (page 2).

[46] V. Swaminathan et al. “Mechanical Stiffness Grades Metastatic Potential in Patient Tumor Cells and in Cancer Cell Lines.” In: *Cancer Research* (June 2011), pp. 5075–5080 (page 2).

[47] W. A. Eaton and J. Hofrichter. “Sickle cell hemoglobin polymerization.” In: *Advances in Protein Chemistry* 40 (1990), pp. 63–279 (page 2).

[48] M. H. Steinberg and C. Brugnara. “Pathophysiological-based approaches to treatment of sickle cell disease.” In: *Annual Review of Medicine* 54 (2003), pp. 89–112 (page 2).

[49] S. K. Ballas and N. Mohandas. “Sickle red cell microrheology and sickle blood rheology.” In: *Microcirculation* 11.2 (2004), pp. 209–225 (page 2).

[50] P. G. Vekilov. “Sickle-cell haemoglobin polymerization: Is it the primary pathogenic event of sickle-cell anaemia?” In: *British Journal of Haematology* 139.2 (2007), pp. 173–184 (page 2).

[51] V. L. R. M. Verstraeten et al. “Increased mechanosensitivity and nuclear stiffness in Hutchinson-Gilford progeria cells: Effects of farnesyltransferase inhibitors.” In: *Aging Cell* 7.3 (2008), pp. 383–393 (page 2).

[52] S. Choi et al. “Computational image analysis of nuclear morphology associated with various nuclear-specific aging disorders.” In: *Nucleus* 2.6 (Nov. 2011), pp. 570–9 (page 2).

[53] S. Even-Ram, V. Artym, and K. M. Yamada. “Matrix Control of Stem Cell Fate.” In: *Cell* 126.4 (2006), pp. 645–647 (page 2).

[54] A. J. Engler et al. “Matrix Elasticity Directs Stem Cell Lineage Specification.” In: *Cell* 126.4 (2006), pp. 677–689 (page 2).

[55] E. F. Koslover et al. “Local geometry and elasticity in compact chromatin structure.” In: *Biophysical Journal* 99.12 (2010), pp. 3941–3950 (page 2).

[56] B. Mergell, R. Everaers, and H. Schiessel. “Nucleosome interactions in chromatin: Fiber stiffening and hairpin formation.” In: *Physical Review E - Statistical, Nonlinear, and Soft Matter Physics* 70.1 1 (2004). arXiv: `0406036 [q-bio]` (page 2).

[57] M. L. Bennink et al. “Unfolding individual nucleosomes by stretching single chromatin fibers with optical tweezers.” In: *Nature Structural Biology* 8.7 (2001), pp. 606–610 (page 2).

[58] T. Roopa and G. V. Shivashankar. “Direct measurement of local chromatin fluidity using optical trap modulation force spectroscopy.” In: *Biophysical Journal* 91.12 (Dec. 2006), pp. 4632–7 (page 2).

[59] J. S. Kanger, V. Subramaniam, and R. Van Driel. *Intracellular manipulation of chromatin using magnetic nanoparticles.* 2008 (page 2).

[60] O. Chaudhuri, S. Parekh, and D. A. Fletcher. “Reversible stress softening of actin networks.” In: *Nature* 445 (2007), pp. 295–298 (pages 2, 11).

[61] M. L. Gardel et al. “Elastic behavior of cross-linked and bundled actin networks.” In: *Science* 304.5675 (2004), pp. 1301–1305 (page 2).

[62] K. E. Kasza et al. *The cell as a material.* 2007. arXiv: `33846280192` (page 2).

[63] P. A. Janmey and D. A. Weitz. *Dealing with mechanics: Mechanisms of force transduction in cells.* 2004 (page 2).

[64] P. A. Janmey. “The cytoskeleton and cell signaling: component localization and mechanical coupling.” In: *Physiological Reviews* 78.3 (1998), pp. 763–781 (page 2).

[65] S. Huang and D. E. Ingber. “The structural and mechanical complexity of cell-growth control.” In: *Nature Cell Biology* 1.5 (1999), E131–E138 (page 2).

[66] M. Ehrbar et al. “Elucidating the role of matrix stiffness in 3D cell migration and remodeling.” In: *Biophysical Journal* 100.2 (2011), pp. 284–293 (page 2).

[67] E. Hadjipanayi, V. Mudera, and R. A. Brown. “Guiding cell migration in 3D: A collagen matrix with graded directional stiffness.” In: *Cell Motility and the Cytoskeleton* 66.3 (2009), pp. 121–128 (page 2).

[68] P. Friedl and K. Wolf. *Plasticity of cell migration: A multiscale tuning model.* 2010 (page 2).

[69] J. R. Lange and B. Fabry. *Cell and tissue mechanics in cell migration.* 2013 (page 2).

[70] E. Kolaczkowska and P. Kubes. “Neutrophil recruitment and function in health and inflammation.” In: *Nature reviews. Immunology* 13.3 (2013), pp. 159–75 (page 3).

[71] A. L. Olins et al. “An in vitro model for Pelger-Huët anomaly: Stable knockdown of lamin B receptor in HL-60 cells.” In: *Nucleus* 1.6 (Jan. 2010), pp. 506–512 (pages 3, 4).

[72] S. Gravemann et al. “Dosage Effect of Zero to Three Functional LBR-Genes in Vivo and in Vitro.” In: *Nucleus* 1.2 (Jan. 2010), pp. 179–189 (pages 3, 4).

[73] J. Ellenberg et al. “Nuclear membrane dynamics and reassembly in living cells: targeting of an inner nuclear membrane protein in interphase and mitosis.” In: *The Journal of cell biology* 138.6 (Sept. 1997), pp. 1193–206 (page 5).

[74] A. Vaziri and M. R. K. Mofrad. “Mechanics and Deformation of the Nucleus in Micropipette Aspiration Experiment.” In: *Journal of biomechanics* 40.9 (Jan. 2007), pp. 2053–62 (page 5).

[75] W. H. De Vos et al. “Increased plasticity of the nuclear envelope and hypermobility of telomeres due to the loss of A-type lamins.” In: *Biochimica et Biophysica Acta* 1800.4 (Apr. 2010), pp. 448–58 (page 5).

[76] A. C. Rowat et al. “Nuclear envelope composition determines the ability of neutrophil-type cells to passage through micron-scale constrictions.” In: *Journal of Biological Chemistry* 288.12 (2013), pp. 8610–8618 (page 5).

[77] J. D. Pajerowski et al. “Physical plasticity of the nucleus in stem cell differentiation.” In: *Proceedings of the National Academy of Sciences* 104.40 (Oct. 2007), pp. 15619–24 (page 5).

[78] J. Swift et al. “Nuclear Lamin-A Scales with Tissue Stiffness and Enhances Matrix-Directed Differentiation.” In: *Science* 341.6149 (2013), pp. 1240104–1240104 (page 5).

[79] A. C. Rowat et al. “Nuclear envelope composition determines the ability of neutrophil-type cells to passage through micron-scale constrictions.” In: *Journal of Biological Chemistry* 288.12 (2013), pp. 8610–8618 (page 5).

[80] S. Stejskal et al. “The role of chromatin condensation during granulopoiesis in the regulation of gene cluster expression.” In: *Epigenetics : official journal of the DNA Methylation Society* 5.8 (2010), pp. 758–766 (page 5).

[81] J. A. McCammon, B. R. Gelin, and M. Karplus. “Dynamics of folded proteins.” In: *Nature* 267.5612 (1977), pp. 585–590 (page 7).

[82] M. Kjaergaard et al. “A folded excited state of ligand-free nuclear coactivator binding domain (NCBD) underlies plasticity in ligand recognition.” In: *Biochemistry* 52.10 (2013), pp. 1686–1693 (page 7).

[83] E. Z. Eisenmesser et al. “Intrinsic dynamics of an enzyme underlies catalysis.” In: *Nature* 438.7064 (2005), pp. 117–121 (page 7).

[84] A. Ansari et al. “Protein states and proteinquakes.” In: *Proceedings of the National Academy of Sciences* 82.15 (1985), pp. 5000–5004 (page 7).

[85] O. Miyashita, J. N. Onuchic, and P. G. Wolynes. “Nonlinear elasticity, protein quakes, and the energy landscapes of functional transitions in proteins.” In: *Proceedings of the National Academy of Sciences* 100.22 (2003), pp. 12570–12575 (page 7).

[86] P. C. Whitford et al. “Conformational Transitions of Adenylate Kinase: Switching by Cracking.” In: *Journal of Molecular Biology* 366.5 (2007), pp. 1661–1671 (page 7).

[87] R. Lakes. Viscoelastic Materials. Cambridge University Press, 2009, pp. 195–244 (pages 7, 8).

[88] R. S. Huismans and C. Beaumont. “Asymmetric lithospheric extension: The role of frictional plastic strain softening inferred from numerical experiments.” In: *Geology* 30.3 (2002), pp. 211–214 (page 8).

[89] L. L. Schramm. Emulsions, Foams, and Suspensions. Wiley, 2006, pp. 1–448 (page 8).

[90] M. Rao. *Rheology of Fluid and Semisolid Foods.* 2007 (page 8).

[91] J. A. Byars, G. F. Fanta, and F. C. Felker. “The effect of cooling conditions on jet-cooked normal corn starch dispersions.” In: *Carbohydrate Polymers* 54.3 (2003), pp. 321–326 (page 8).

[92] Y. Wang and G. Zocchi. “Viscoelastic transition and yield strain of the folded protein.” In: *PLoS ONE* 6.12 (2011) (pages 8, 9).

[93] P. Chaikin and T. Lubensky. Principles of condensed matter physics. Cambridge University Press, 2000, p. 717 (page 9).

[94] M. Trejo et al. “Elasticity and wrinkled morphology of Bacillus subtilis pellicles.” In: *Proceedings of the National Academy of Sciences of the United States of America* 110.6 (Feb. 2013), pp. 2011–6 (pages 10, 11).

[95] J. Dervaux and M. B. Amar. “Buckling condensation in constrained growth.” In: *Journal of the Mechanics and Physics of Solids* 59.3 (Mar. 2011), pp. 538–560 (page 10).

[96] K. Li, K. Ding, and S. Cai. “Diffusion-induced wrinkling instability in a circular poroelastic plate.” In: *Applied Physics Letters* 102.24 (June 2013), p. 241908 (page 10).

[97] L. Landau and E. Lifshitz. Theory of Elasticity. 3rd. Vol. 7. Course of Theoretical Physics. Elsevier Inc., 1986 (pages 10, 11, 18).

[98] L. Euler. Mechanica, Sive Motus Scientia Analytice. St. Petersburg, Russia: Ex Typographia Academiae Scientiarum, 1736 (page 11).

[99] L. Golubovic, D. Moldovan, and A. Peredera. “Dynamics of the Euler Buckling Instability.” In: *Physical Review Letters* 81 (1998), p. 3387 (page 11).

[100] J. D. Hartog. Strength of Materials. New York: Dover, 1977 (page 11).

[101] M. Das, A. Levine, and F. MacKintosh. “Buckling and force propagation along intracellular microtubules.” In: *Europhysics Letters* 84 (2008), p. 18003 (page 11).

[102] E. Conti and F. MacKintosh. “Cross-linked Networks of Stiff Filaments Exhibit Negative Normal Stress.” In: *Physical Review Letters* 102 (2009), p. 088102 (page 11).

[103] M. S. e Silva et al. “Active multistage coarsening of actin networks driven by myosin motors.” In: *Proceedings of the National Academy of Sciences of the United States of America* 108.23 (2011), pp. 9408–9413 (page 11).

[104] E. Cerda and L. Mahadevan. “Geometry and Physics of Wrinkling.” In: *Physical Review Letters* 90.7 (Feb. 2003), pp. 1–4 (pages 11, 34).

[105] E. Rodriguez, A. Hoger, and A. McCulloch. “Stress-dependent finite growth in soft elastic tissues.” In: *Journal of biomechanics* 27.4 (Apr. 1994), pp. 455–67 (page 11).

[106] D. Drasdo. “Buckling instabilities of One-Layered Growing Tissues.” In: *Physical Review Letters* 84.18 (2000), p. 4244 (page 11).

[107] A. Goriely and M. Ben Amar. “Differential growth and instability in elastic shells.” In: *Physical review letters* 94.19 (May 2005), 198103-1–4 (pages 11, 32).

[108] M. B. J. Dervaux. “Morphogenesis of Growing Soft Tissues.” In: *Physical Review Letters* 101 (2008), p. 068101 (page 11).

[109] A. N. M. Kücken. “A model for fingerprint formation.” In: *Europhysics Letters* 68.1 (2004), pp. 141–146 (page 11).

[110] e. a. T. Sato. “Single Lgr5 stem cells build crypt-villus structures in vitro without a mesenchymal niche.” In: *Nature* 459.7244 (2009), pp. 262–265 (page 11).

[111] J.-F. J. E. Hannezo J. Prost. “Instabilities of Monolayered Epithelia: Shape and Structure of Villi and Crypts.” In: *Physical Review Letters* 107 (2011), p. 078104 (page 11).

[112] J. Genzer and J. Groenewold. "Soft matter with hard skin: From skin wrinkles to templating and material characterization." In: *Soft Matter* 2.4 (2006), pp. 310–23 (page 11).

[113] J. Yoon, J. Kim, and R. C. Hayward. "Nucleation, growth, and hysteresis of surface creases on swelled polymer gels." In: *Soft Matter* 6.22 (2010), p. 5807 (page 11).

[114] D. Breid and A. J. Crosby. "Effect of stress state on wrinkle morphology." In: *Soft Matter* 7.9 (2011), pp. 4490–96 (page 11).

[115] R. Huang and S. Im. "Dynamics of wrinkle growth and coarsening in stressed thin films." In: *Physical Review E* 74.2 (Aug. 2006), pp. 1–12 (page 12).

[116] H. Diamant and T. A. Witten. "Compression Induced Folding of a Sheet: An Integrable System." In: *Physical Review Letters* 107.16 (Oct. 2011), pp. 1–4 (pages 12, 34).

[117] A. Viallat, J. Dalous, and M. Abkarian. "Giant lipid vesicles filled with a gel: shape instability induced by osmotic shrinkage." In: *Biophysical journal* 86.4 (Apr. 2004), pp. 2179–87 (pages 12, 14, 30, 32).

[118] B. Li et al. "Surface Wrinkling Patterns on a Core-Shell Soft Sphere." In: *Physical Review Letters* 106.23 (June 2011), pp. 2–5 (pages 12, 30, 31, 33).

[119] A. C. Rowat, J. Lammerding, and J. H. Ipsen. "Mechanics of the cell nucleus and effects of emerin deficiency." In: *Biophysical journal* 91 (2006), pp. 4649–64 (pages 12, 31).

[120] C. Brangwynne et al. "Microtubules can bear enhanced compressive loads in living cells because of lateral confinement." In: *Journal of Cell Biology* 173.5 (2006), pp. 733–741 (page 17).

[121] P. Leo et al. "Elastic fields about a perturbed spherical inclusion." In: *Acta Metallurgica* 33.6 (1985), pp. 985–989 (page 20).

[122] M. Abramowitz and I. A. Stegun. Handbook of mathematical functions: with formulas, graphs, and mathematical tables. New York: Dover, 1970 (page 26).

[123] G. B. Arfken and H. J. Weber. Mathematical Methods for Physics. 6th. Academic Press, 2005 (page 26).

[124] I. S. Gradshteyn, I. M. Ryzhik, and A. Jeffrey. Table of integrals, series, and products. 6th. San Diego: Academic Press, 2000 (page 26).

[125] J. D. Finan and F. Guilak. "The effects of osmotic stress on the structure and function of the cell nucleus." In: *Journal of Cellular Biochemistry* (2009), n/a–n/a (page 30).

[126] G. Cao et al. "Self-Assembled Triangular and Labyrinth Buckling Patterns of Thin Films on Spherical Substrates." In: *Physical Review Letters* 100.3 (2008), p. 036102 (page 30).

[127] A. C. Rowat, D. Keller, and J. H. Ipsen. "Effects of farnesol on the physical properties of DMPC membranes." In: *Biochemica et Biophysica Acta* 1713.1 (2005), pp. 29–39 (page 31).

[128] J. Yin et al. "Stress-driven buckling patterns in spheroidal core/shell structures." In: *Proceedings of the National Academy of Sciences of the United States of America* 105.49 (Dec. 2008), pp. 19132–5 (page 31).

[129] H. Shum et al. "Dewetting-induced Membrane Formation by Adhesion of Amphiphile-Laden Interface." In: *Journal of the American Chemical Society* 133 (2011), pp. 4420–4426 (page 31).

[130] B. a. Mattson, E. W. Overstrom, and D. F. Albertini. "Transitions in trophectoderm cellular shape and cytoskeletal organization in the elongating pig blastocyst." In: *Biology of reproduction* 42.1 (Jan. 1990), pp. 195–205 (page 31).

[131] M. Ben Amar and A. Goriely. "Growth and instability in elastic tissues." In: *Journal of the Mechanics and Physics of Solids* 53.10 (2005), pp. 2284–2319 (page 32).

[132] X. Chen and J. Hutchinson. "Herringbone Buckling Patterns of Compressed Thin Films on Compliant Substrates." In: *J. Appl. Mech.* 71 (2004), pp. 597–603 (page 33).

[133] S. Safran. Statistical Thermodynamics Of Surfaces, Interfaces, And Membranes. Frontiers in Physics. Westview Press, 2003 (page 34).

[134] A. Love. A Treatise on the Mathematical Theory of Elasticity. New York: Dover, 1944 (page 42).

[135] E. U. Condon and G. H. Shortley. The Theory of Atomic Spectra. Cambridge University Press, 1935 (page 52).

[136] A. Messiah. Quantum Mechanics. Dover Publications, 1999 (page 52).

[137] Y. Wang and G. Zocchi. "Viscoelastic Transition and Yield Strain of the Folded Protein." In: *Plos One* 6.12 (2011) (pages 58, 90).

[138] W. Yong and G. Zocchi. "The folded protein as a viscoelastic solid." In: *Europhysics Letters* 96.1 (2011), 18003-1–6 (pages 58, 90).

[139] Q. Hao, J. Landy, and G. Zocchi. "Cracking phase diagram for the dynamics of an enzyme." In: *Physical Review E (Statistical, Nonlinear, and Soft Matter Physics)* 86.4 (2012), pp. 041915–041915 (pages 58, 60, 90).

[140] D. Whitford. Proteins : structure and function. Hoboken, NJ: J. Wiley & Sons, 2005 (page 58).

[141] R. Phillips et al. Physical biology of the cell. Second. London New York, NY: Garland Science, 2013 (page 58).

[142] R. S. Lakes. Viscoelastic materials. Cambridge; New York: Cambridge University Press, 2009, xviii, 461 p. (Pages 59, 61).

[143] M. Suzuki and R. Kubo. "Dynamics of Ising Model near Critical Points .I." In: *Journal of the Physical Society of Japan* 24.1 (1968), p. 51 (pages 60, 91).

[144] T. Tomé and M. J. de Oliveira. "Dynamic phase transition in the kinetic Ising model under a time-dependent oscillating field." In: *Physical Review A* 41.8 (1990), pp. 4251–4254 (pages 60, 91).

[145] W. N. Findley, J. S. Lai, and K. Onaran. Creep and relaxation of nonlinear viscoelastic materials: with an introduction to linear viscoelasticity. Dover books on engineering. New York: Dover, 1989, xii, 371 p. (Pages 61, 71).

[146] M. M. Tirion. “Large amplitude elastic motions in proteins from a single-parameter, atomic analysis.” In: *Physical Review Letters* 77.9 (1996), pp. 1905–1908 (page 61).

[147] A. Ansari et al. “Protein States and Protein Quakes.” In: *Proceedings of the National Academy of Sciences of the United States of America* 82.15 (1985), pp. 5000–5004 (page 61).

[148] O. Miyashita, J. N. Onuchic, and P. G. Wolynes. “Nonlinear elasticity, proteinquakes, and the energy landscapes of functional transitions in proteins.” In: *Proceedings of the National Academy of Sciences of the United States of America* 100.22 (2003), pp. 12570–12575 (page 61).

[149] See also Anderson *et. al.*: Chapter 8 of A. Noy. Handbook of molecular force spectroscopy. New York, NY: Springer, 2008 (page 61).

[150] J. Guckenheimer and P. Holmes. Nonlinear oscillations, dynamical systems, and bifurcations of vector fields. Corr. 5th print. Applied mathematical sciences. New York: Springer, 1997 (page 75).

[151] M. J. Feigenbaum. “Quantitive Universality for a Class of Non-Linear Transformations.” In: *Journal of Statistical Physics* 19.1 (1978), pp. 25–52 (page 75).

[152] H. Risken. The Fokker-Planck Equation. 2nd. Vol. 18. Series in Synergetics. Springer, 1989, p. 454 (page 87).

[153] Y. Wang and G. Zocchi. “The folded protein as a viscoelastic solid.” In: *Europhysics Letters* 96.1 (2011) (page 90).

[154] N. W. Ashcroft and N. D. Mermin. Solid state physics. New York, Holt Rinehart and Winston, 1976, pp. xxi, 826 (page 99).

[155] C. A. Fogle, J. L. Nagle, and M. M. Desai. “Clonal interference, multiple mutations and adaptation in large asexual populations.” In: *Genetics* 180.4 (Dec. 2008), pp. 2163–73.